

2017-01-01

Investigation on a Cooling Channel Design for a High Heat Flux Oxy-Fuel Direct Power Extraction Combustor

Luisa Alejandra Cabrera Maynez

University of Texas at El Paso, broadwaykoala@gmail.com

Follow this and additional works at: https://digitalcommons.utep.edu/open_etd



Part of the [Mechanical Engineering Commons](#)

Recommended Citation

Cabrera Maynez, Luisa Alejandra, "Investigation on a Cooling Channel Design for a High Heat Flux Oxy-Fuel Direct Power Extraction Combustor" (2017). *Open Access Theses & Dissertations*. 416.

https://digitalcommons.utep.edu/open_etd/416

This is brought to you for free and open access by DigitalCommons@UTEP. It has been accepted for inclusion in Open Access Theses & Dissertations by an authorized administrator of DigitalCommons@UTEP. For more information, please contact lweber@utep.edu.

INVESTIGATION ON A COOLING CHANNEL DESIGN FOR A HIGH HEAT
FLUX OXY-FUEL DIRECT POWER EXTRACTION COMBUSTOR

LUISA ALEJANDRA CABRERA MAYNEZ

Doctoral Program in Mechanical Engineering

APPROVED:

Norman D. Love Jr., Ph.D., Chair

Ahsan Choudhuri, Ph.D.

Yirong Lin, Ph.D.

Bill Tseng, Ph.D.

Charles Ambler, Ph.D.
Dean of the Graduate School

Copyright ©

by

Luisa Alejandra Cabrera Maynez

2017

Dedication

To my mom, to whom I owe everything. To my husband, for providing unconditional support to be my best self. To my brother and grandparents, for their care and comprehension. To my teammates, for their friendship and shared lessons learned. Finally, to my advisor, Dr. Norman Love, for his guidance and mentoring throughout this time.

I would not be here without any of you.

INVESTIGATION ON A COOLING CHANNEL DESIGN FOR A HIGH HEAT
FLUX OXY-FUEL DIRECT POWER EXTRACTION COMBUSTOR

by

LUISA ALEJANDRA CABRERA MAYNEZ, BSME, MSME

DISSERTATION

Presented to the Faculty of the Graduate School of

The University of Texas at El Paso

in Partial Fulfillment

of the Requirements

for the Degree of

DOCTOR OF PHILOSOPHY

Department of Mechanical Engineering

THE UNIVERSITY OF TEXAS AT EL PASO

August 2017

Acknowledgements

This research is supported by the US Department of Energy, under award DE-FE-0024062 (Project Manager Jason Hissam). However, any opinions, findings, conclusions, or recommendations expressed herein are those of the authors and do not necessarily reflect the view of the Department of Energy. The author acknowledges the support of the National Council of Science and Technology in México (CONACYT) for the pursuit of her postgraduate studies.

Abstract

The implementation of oxy-fuel technology in fossil-fuel power generation could result in a drastic increase of system efficiencies and a reduction of emissions. While typical system temperatures are dictated by material constraints, open-cycle magnetohydrodynamic (MHD) power generators have the potential to utilize the energy of undiluted flames. This work presents design and modeling strategies to develop steady-state supersonic MHD combustors operating at temperatures exceeding 3000 K. Throughout the study, computational fluid dynamics (CFD) models were extensively used as a design and optimization tool. A proof-of-concept 60 kWth model was designed, manufactured and tested in accordance to methods relevant to rocket engine technologies. A fully-coupled numerical method was developed in ANSYS FLUENT to characterize the heat transfer in the system; this study revealed that nozzle heat transfer may be predicted through a 40% reduction of the semi-empirical Bartz correlation. Experimental results showed good agreement with the numerical evaluation, with the combustor exhibiting a favorable performance when tested during extended time periods. The results observed in the proof-of-concept system were employed to develop a 1-MW scaled prototype. Scaling methods were based on critical design criteria found in similar systems, aimed at replicating combustion flow fields and reducing possible instabilities. The scaled prototype was manufactured through selective laser melting (SLM)-based additive manufacturing to reduce lead times and increase geometrical complexity. Additional CFD models were developed to optimize coolant manifold system parameters and perform a parametric study on channel geometry. An investigation on coolant manifold geometry demonstrated improvements in channel flow distribution when enlarging manifold lengths and increasing the number of tubes feeding into the flow. A three-dimensional model based on a single channel was developed to capture the effect of variable properties and

thermal stratification. All cases in the simulation exhibited higher wall temperatures and lower convective coefficients than those determined through 1-D analytical means. This implies pressure and velocity safety factors must be implemented in system operation. Overall, the findings made in this investigation are thought to be of value to researchers and industrial practitioners when designing thermal protection devices for high temperature, high heat flux systems. In addition to this, the implementation of the developed technology at pilot and commercial scales could result in a significant improvement in the efficiencies of heritage and next-generation power cycles.

Table of Contents

Acknowledgements.....	v
Abstract.....	vi
Table of Contents.....	viii
List of Tables	xi
List of Figures.....	xii
Chapter 1: Introduction and Background.....	1
1.1 Introduction.....	1
1.2 Literature Review.....	1
1.2.1 MHD	1
1.2.2 Nozzle Cooling Systems	5
1.3 Project Objectives	8
1.4 Practical Relevance.....	8
1.5 Commercialization Potential.....	9
Chapter 2: Design Methodology.....	11
2.1 Combustor and Nozzle Design	11
2.2 Cooling System Design.....	14
2.2.1 Estimates of Temperature through the Conduction Equation.....	18
2.3 Technical Approach.....	18
2.3.1 Experimental Apparatus.....	18
2.3.1.1 Combustor.....	18
2.3.1.2 Feed System.....	21
2.3.2 Experimental Approach & Test Matrix	23
Chapter 3: Numerical Methodology (60 kW Combustor)	25
3.1 Theory	25
3.2 Geometry and Boundary Conditions	28
3.3 Characterization of Geometry into Axisymmetric Model	32
Chapter 4: Results & Discussion (60 kW Combustor)	34
4.1 Experimental Results	34
4.2 Numerical Results.....	36

4.2.1 Combustion Gas Model-Axial Properties	36
4.2.2 Coupled Heat Transfer Analysis	40
4.2.3 Comparison to Experimental Results	44
Chapter 5: Design Methodology (1 MW Combustor)	48
5.1 1MW DPE Combustor Development	48
5.2 Scaling Procedures	49
5.3 Additive manufacturing & final design	56
Chapter 6: Optimization of Cooling System	65
6.1 Manifold Optimization	65
6.1.1 Numerical Domain and Setup	66
6.1.2 Numerical Results	72
6.1.3 Mesh Independence Results	76
6.2 Parametric Fin Study	77
6.2.1 Analytical Methodology	78
6.2.2 Analytical efficiency results	80
6.3 Numerical Fin Study	83
6.3.1 Numerical Domain and Setup	84
6.3.2 Numerical Results	90
6.3.3 Mesh Independence Results	112
Chapter 7: Summary and Future Work	114
7.1 Next steps/Considerations	120

References	121
Appendix A: Nomenclature	126
Appendix B: Sample Calculations	131
Appendix C: Experimental Uncertainty Calculations.....	135
Appendix D: Estimates of Numerical Error for 60 kW Coupled Simulation	136
Appendix E: Material properties for numerical models	140
Appendix F: Blueprints for 60-kW and 1-MW Combustors	143
Vita	145

List of Tables

Table 1: Overall design parameters	17
Table 2: Operational and geometrical parameters of the combustor	20
Table 3: Experimental tests performed using the combustor.....	24
Table 4: List of boundary conditions used in 2-D numerical model	30
Table 5: Comparison between numerical and analytical methods.....	37
Table 6: Results comparison to experimental measurements	46
Table 7: Comparisons of design criteria	55
Table 8: Dimensional analysis results on 1-MW combustor built by AM methods.....	63
Table 9: Dimensional Analysis Results for Cooling Shells.....	64
Table 10: Cases Employed in Manifold Simulation	67
Table 11: Boundary Conditions employed in manifold simulation.....	70
Table 12: Manifold Model Results	76
Table 13: Cases employed in channel simulation.....	85
Table 14: Boundary conditions employed in channel simulation.....	88
Table 15: Channel model results.....	99
Table 16: Local efficiency comparison of channels	112
Table 17: Combustion parameters for 1MW model	131
Table 18: Cooling system parameters for 1-MW model	133
Table 19: Error analysis of temperature and flow sensors.....	136
Table 20: Numerical predictions of converged value	139

List of Figures

Figure 1: Schematic of an open-cycle MHD power generator	2
Figure 2: Schematic of the MHD open-cycle combustor.	11
Figure 3: Block layout of experimental apparatus.....	12
Figure 4: Adiabatic flame temperatures of CH ₄ -O ₂ for pressures of 4-8 bar	13
Figure 5: Thermal-resistance model used for the analysis of the combustor and nozzle	14
Figure 6: Exploded view of combustor system components	20
Figure 7: a) Isometric view of the 60 kW combustor b) Milled cooling channels	21
Figure 8: Experimental setup feed system layout	22
Figure 9: LabView interface	23
Figure 10: Computational domain with boundary conditions labeled.....	28
Figure 11: Gas flow rates during 5 minute test.....	34
Figure 12: Water and wall temperature variations for 5 minute test	35
Figure 13: Temperature contours for axisymmetric simulation	37
Figure 14: Comparison of nozzle velocity.....	40
Figure 15: Comparison of axial nozzle temperature.....	40
Figure 16: Comparison of heat flux calculation from numerical and analytical model	41
Figure 17: Inner combustor and (outer) channel wall temperatures in the nozzle region	42
Figure 18: Comparison of nozzle data using (top) numerical and (bottom) analytical model	43
Figure 19: Development of thermal stratification through cooling channels	44
Figure 20: Comparison of numerical and analytical model results to experimental values	47
Figure 21: Historical scope of open-cycle MHD studies.....	49
Figure 22: Exploded view of main combustor components	54
Figure 23: Principal dimensions of 1-MW design.....	54
Figure 24: Mechanical properties of Inconel 718 as reported by Trosch et al. [56].....	57
Figure 25: Comparison between CAD and AM models.....	58
Figure 26: Detailed views of the 1-MW combustor	58
Figure 27: Thermocouple port views a) side b) top c) detail	59
Figure 28: Outer shells manufactured by SLM.....	60
Figure 29: Partial assembly view of a) nozzle and b) inlet components	61
Figure 30: Schematic of measured dimensions	62
Figure 31: Schematic of measured dimensions (shells).....	62
Figure 32: Domain for manifold simulation	66
Figure 33: Manifold simulation mesh detail.....	67
Figure 34: Inner wall boundary condition, UDF	69
Figure 35: Temperature contours of base model A (periodic repeats)	72
Figure 36: Comparisons of exit velocity contours.....	73
Figure 37: Comparison of temperature zones above 450 K	75
Figure 38: Comparisons of wall temperature at channel midline	77
Figure 39: Setup for analytical fin efficiency	78
Figure 40: Aspect ratio efficiency comparison	81
Figure 41: Hydraulic diameter efficiency comparison	82
Figure 42: Channel number efficiency comparison.....	83
Figure 43: Domain for periodic channel simulation	85
Figure 44: Channel simulation mesh detail	86

Figure 45: Convective heat transfer coefficient in walls, user defined function	87
Figure 46: Boundary layer temperature in walls, user defined function.....	87
Figure 47: Temperature contours of base model A (periodic repeats)	90
Figure 48: Channel bottom temperature (Aspect ratio comparison)	91
Figure 49: Channel bottom temperature (Hydraulic diameter comparison).....	92
Figure 50: Channel bottom temperature (Channel number comparison)	92
Figure 51: Combustion-side wall temperature (Aspect ratio comparison).....	93
Figure 52: Combustion-side wall temperature (Hydraulic diameter comparison)	94
Figure 53: Combustion-side wall temperature (Channel number comparison).....	94
Figure 54: Combustion-side wall temperature (Aspect ratio comparison-radial)	95
Figure 55: Combustion-side wall temperature (Hydraulic diameter comparison-radial)	96
Figure 56: Combustion-side wall temperature (Channel number comparison- radial)	97
Figure 57: Channel stratification, aspect ratio comparison	101
Figure 58: Channel stratification, hydraulic diameter comparison.....	101
Figure 59: Water centerline temperature comparison (Hydraulic diameter)	102
Figure 60: Channel stratification at throat, channel number comparison	102
Figure 61: Water centerline temperature comparison (Channel number)	103
Figure 62: Dean Vortices in base model A.....	104
Figure 63: Radial velocity contours for base model A	105
Figure 64: Convective heat transfer coefficient comparison (Aspect ratio)	107
Figure 65: Convective heat transfer coefficient comparison (Hydraulic diameter)	107
Figure 66: Convective heat transfer coefficient comparison (Channel number).....	108
Figure 67: Detailed view of radial velocity contours.....	108
Figure 68: Case comparison between a) Pizzarelli et. al [54] and b) current configuration.....	109
Figure 69: Fin base temperature comparison (Aspect ratio).....	110
Figure 70: Fin base temperature comparison (Hydraulic diameter)	110
Figure 71: Fin base temperature comparison (Channel number).....	111
Figure 72: Fin temperature stratification, comparison at throat	111
Figure 73: Comparisons of midline channel velocity	113
Figure 74: Spatial error % in log-log space comparing temperature and flux values for localized point	138
Figure 75: Spatial error % in log-log space comparing average and localized values	138
Figure 76: Thermal conductivity of water	140
Figure 77: Heat capacity of water	140
Figure 78: Density of water	141
Figure 79: Viscosity of water.....	141
Figure 80: Thermal conductivity of Inconel 718	142
Figure 81: Dimensions for 60-kW Combustor (mm)	143
Figure 82: Dimensions for 1-MW Combustor (mm).....	144

Chapter 1: Introduction and Background

1.1 Introduction

Recent demand for alternative energy sources has spurred the development of novel technologies for power generation. As global consciousness on the effect of greenhouse gases grows, there has been a call for the reduction of high-emission devices. Fossil-fuel based power generation has been identified as a major contributor of carbon dioxide released to the environment. This type of power generation was responsible for 31% of the 6,673 million metric tons of the gas emitted in the United States in 2013 [1]. An alternative for the enhancement of existing fossil-fuel based technologies is integration of oxy-fuel combustion [2] [3]. This process replaces air for oxygen when burning hydrocarbons, simplifying the process of CO₂ sequestration due to the products of its reaction. Nevertheless, temperatures for oxy-based systems can exceed 3000 K, imposing design constraints that are limited by existing material operability limits. In many other systems CO₂ and steam based flue gases are recycled to lower the flame temperature to those used in air-based systems. However, if it is possible to harness the energy release at 3000K, according to Carnot, much higher efficiencies are possible. A technology with the potential to fully utilize the temperatures of undiluted oxy-fuel based combustion is a direct power extraction (DPE) or magnetohydrodynamic (MHD) generator.

1.2 Literature Review

1.2.1 MHD

An MHD direct power extraction unit produces electricity based on Faraday's law of induction, where current is generated through the interaction of a conductor and a magnetic field. One advantage of this type of system is that it possesses no moving parts and it is possible to directly convert the energy in hot gases to electricity. This aspect of the MHD system simplifies

some design parameters such as those faced many times by turbine-based systems, such as blade cooling. Two basic categories of MHD generators exist: closed generators employing a heated inert gas combined with an alkaline metal, and open generators involving combustion products seeded by an alkaline compound [4]. In recent times, open-cycle MHD generators have received increasing attention on their energy extraction potential from the products of oxy-fuel combustion [4] [5]. The conversion of ionized flows in MHD power extraction topping cycles may exceed the efficiencies of those seen in conventional gas turbines. Additionally, access to in-situ carbon capture is made possible by the combination of fossil-fuel combustion and MHD. The use of fossil-fuel driven ionized gases in constitutes the basis for open-cycle MHD. Experimentally, MHD generators have been demonstrated to achieve enthalpy extraction ratios in the range of 10-20% when using a shock-driven disk channel. When employed as part of a topping cycle, the enthalpy extraction ratio has been recorded to be as high as 24.5%, corresponding to the plant-size U-500 developed in the USSR [4].

Open cycle MHD generators involve several subsystems, including a combustion chamber, nozzle, and a segmented Faraday or Hall generator, which is subjected to a magnetic field [6]. Inside the MHD channel, the gas velocity is diminished through the magnetic field, generating a retarding (Lorentz) force orthogonal to fluid motion [7]. The resultant ions are collected by electrodes, creating an electric current. A block diagram depicting the subsystems of an open cycle generator is shown in Figure 1.

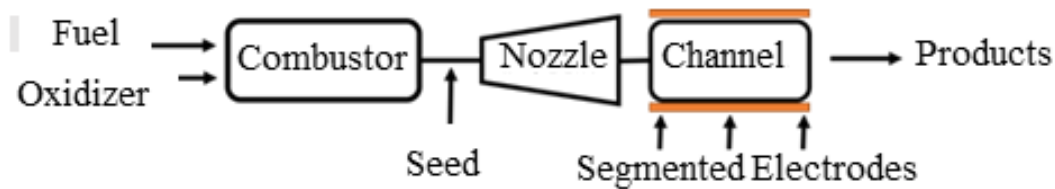


Figure 1: Schematic of an open-cycle MHD power generator

Magnetic field interaction with seeded combustion gases has been investigated since the 1960s [8], with the first MHD combustion experiment being conducted in 1961 [9]. A variety of studies concerning MHD power extraction were conducted in the 1960-1990 time span, with Russia leading the effort in MHD power plant development. The United States and Russia tested ionized gases for their use when combined with downstream-placed turbines. During this time, the United States focused upon the development of alkali-metal seeded pulverized coal-fired gases for use with MHD technology [4]. On the other hand, Russia developed this technology through the use of natural gas from the first MHD pilot plant facility in 1963 [8] until the close of the U-500 plant in the 1980s [4]. The U-500 plant was designed to perform with a 1100 MW_{th} input, an output of 582 MW_e (of which 270 MW_e came from MHD and 312 from the bottoming cycle) [8]. Unfortunately, this plant was seen to exhibit low electrical conductivities in its combustion process, as well as significant electrode oxidation [4]. The closure of the plant due to Russia's changing political scenario was seen as a serious obstacle to the advance of MHD technology.

Stricter environmental regulations implemented during the 1980s prompted the United States to look into retrofitting MHD power plants of 25-30 MWe outputs. Several cycles were suggested and investigated [8]. A 1982 proposal of a retrofit MHD power plant was theorized to increase conventional power plant efficiency by 5% with moderate costs; while it initially gained momentum, financial constraints prevented retrofitting projects from being funded to completion. The implementation of the MHD retrofit concept was quoted as necessary to the future of commercial MHD plants [8]. Investigations of MHD technology in power plant infrastructures have seen a sharp decline since 1993; during this same year, the Department of Energy's MHD POC experiments were terminated. This decline can be attributed to unresolved research questions in regards to the durability of electrodes, low electrical conductivities and a lack of materials capable of withstanding the operational conditions [4]. Additionally, the technology was not extensively commercialized [10]. Due to this, recent data of MHD is limited particularly for oxy-fuel combustion based systems.

In the present day, many studies focus upon the use of computational methods to predict the ability of gases exiting MHD combustors to conduct and produce electricity. Assumptions are often made to simplify the analysis and design of the system. Aithal and Ishikwa presented computational models capable of predicting optimum power extraction [11] [12]. In these models, the authors were able to simulate plasma flow through a magnetic field through the implementation of the Navier-Stokes equations. In another computational study, Bhadoria showed that oblique shocks form inside the MHD channel as the gas passes through the field [13]. In this study, these shocks were shown to aid in power generation. Computational models for the cooling of the MHD system have also been investigated. A 1-D heat transfer study was conducted by Wolfendale to model the fusion blanket in an MHD generator [14]. Using OPENFOAM, the authors were able to predict pressure loss and temperature profiles along the combustor walls.

Electrical conductivities in MHD power generation have been enhanced by oxygen enrichment environments [4]. The introduction of excess oxygen results in an increase of adiabatic flame temperature, reaction heat release and electrical conductivity of the working fluid. Nevertheless, there is limited data on oxy-fuel combustion for open-cycle MHD power extraction. Kayukawa performed thermodynamic cycle analyses to assess the possible use of this technology in 2004 [5]. This researcher clarified that the conductivities from ionized natural gas in comparison to coal-fired ionized gas presented relatively higher conductivities due to slag defects. An advantage of open-cycle MHD is presented in more efficient energy conversion and heat utilization. Efficiency quantification in literature is frequently cited as thermal conversion efficiencies or enthalpy extraction ratios. Thermal conversion efficiencies have been recorded to have values up to 48 percent [15]. However, combined cycle configurations that may output efficiencies beyond 60 percent [6].

In open-cycle systems, temperature of the conducting fluid significantly impacts the performance of the MHD-based generators, since the electrical conductivity of gases depends on this parameter [4]. This dependence, on the order of T^{10} , promotes operation at elevated

temperatures and is beneficial in terms of obtaining higher thermal efficiencies [4] [6]. Assuming combustion temperatures of 3500 K, the maximum theoretical enthalpy extraction ratio achievable is 35% [4]. Use of oxy-fuel combustion at the conditions presented produces flame temperatures of 3000 K; continuous operation at this elevated temperature and the elevated risk of corrosion present a challenge due to current material limitations [16] [17]. Because of this limitation, the steady-state operation of an MHD power generator employing oxy-combustion requires the inclusion of a highly effective cooling system or diluent gases to lower the flame temperatures. In either case, heat flux and temperatures are expected to be highest at the throat of the nozzle.

1.2.2 Nozzle Cooling Systems

The steady-state operation of an MHD power generator employing oxy-combustion requires the inclusion of an effective cooling mechanism. In this configuration, heat fluxes are expected to be significant due to the acceleration of gases to supersonic velocities. De Laval nozzle theory dictates that the highest fluxes will occur at the minimum cross-sectional area region, where gases reach Mach 1. The subject of nozzle cooling has largely been approached by rocket engine designers, who in the past have relied upon empirical and semi-empirical correlations for the development of cooling systems.

Due to the complex nature of the issue, an accurate solution to the issue must effectively couple combustion gas properties, high temperature material characteristics and coolant flow-fields. Past research efforts cite inherent flaws in the decoupled design strategies used in the industry, which can lead to low solution accuracy [18] [19]. Current strategies in the subject of rocketry vary from the use of 1-D semi-empirical correlations to computationally expensive three dimensional approaches [20].

Marchi et al [21] presented a one-dimensional mathematical model using three coupled subproblems in accordance to the combustion-wall-coolant configuration. This approach seems to

diverge from the majority of current researchers, as most groups have attempted to characterize nozzle heat transfer through 2-D or 3-D computational solutions.

Kim et al [22] [23] employed a combination of numerical methods with semi-empirical correlations found in literature. A study by these authors quantitatively evaluated the design of a kerosene-cooled engine and validated the results against hot firing test data. This uncoupled design accommodates cooling channel features and fin efficiency. Overall, these researchers concluded that the use of a simple thermal resistance model was effective when characterizing temperature and pressure drops in cooling channels.

Combined resolution methods abound in similar studies, such as the one presented by Zhang et al [24]. These researchers adopted a 1-D empirical model to simulate coolant flow, but opted to model combustion gas through a two-dimensional axisymmetric simulation. A common modeling approach to nozzle cooling is that of a semi-coupled iterative method [19] [25] [26]. This technique is characterized by the solution of heat transfer characteristics in an iterative manner between submodels. For instance, gaseous characteristics may be obtained and placed as thermal boundary conditions in a channel-centered simulation, such as the aforementioned study performed by Zhang et al [24]. This process is repeated until both models achieve mutual convergence for an unknown parameter.

Pizzarelli et al [18] [27] have presented various works based on this methodology. These researches have studied the effect of wall heat conduction on heat flow for high aspect ratio cooling channels. The first study by these authors [26] found that a coupled conduction-convection model effectively characterized pressure and heat flux, but overestimated wall temperatures when compared to published data from the space shuttle main engine. The second study based on a quasi 2-D model [18] concluded that the Bartz correlation for nozzle heat transfer overpredicts the convective heat transfer by as much as 40% in the throat area. In addition to this, the study concluded that the effect of stratification within the channels must be accounted for in a simulation, due to the possibility of error propagation in thrust chamber design.

A study by Wang et al [19] employed a 3-D heat conduction submodel and a 1-D channel hydraulic model to compare to data from the space shuttle main engine combustion chamber. A 1-D calculation was employed for the hot-gas-side flow boundary condition accounting for film coolant flow. Though the use of an iterative procedure, these researchers were able to effectively characterize heat flux data when compared to methods employed by Rocketdyne and Pratt & Whitney. An additional finding showed that the maximum heat flux occurred at a location slightly upstream of the throat, where the engine is most susceptible to blanching and cracks.

Constraints for an MHD cooling system design dictate that the unit must be operational for an indefinite period of time. For this reason, while the cooling solution strategy is similar, the design will deviate in some ways from the studies presented above. An example lies in the fact that the choice in cooling fluid is not limited to the fuel, as reinjection to the chamber is not needed. A system similar to an MHD-based combustor is that of a high velocity oxy-fuel (HVOF) gun. This configuration typically employs water or air as a cooling fluid. Nevertheless, a review in literature revealed that most HVOF-centered studies do not focus upon this aspect, but rather on combustion reactions and the introduction of seeding particles into the flow [28] [29] [30]. The latter studies may show to be of importance for researchers focused on the injection of the alkali metal seed in the MHD configuration. A study on the matter of cooling was performed by Katanoda et al [31], who analytically estimated the cooling rate of an HVOF gun through a relationship based on enthalpy of reaction. This equation was coupled with a quasi-one dimensional calculation that described internal flow.

Although extensive investigations have been performed on the subject of nozzle cooling methods, currently there is no consensus on the specific relationships that should be used for high temperature and high heat-flux environments. In addition to this, there is a lack of recent research on MHD open-cycle generators powered by fossil fuels burning in the presence of oxygen without diluents.

1.3 Project Objectives

The goal of this project is to introduce a design and modeling methodology for an MHD-Based Direct Power Extraction system capable of operation at stoichiometric conditions. This analysis is to be focused on the thermal management system required for steady-state operation at maximum gas ($\text{CH}_4\text{-O}_2$) temperature. Combustor exit gas parameters are to exceed 2000 m/s and 3000 K. The design, building, and testing of a 60 kW_{th} proof-of-concept model is followed by the development of a 1-MW_{th} combustor. Combustor geometries are to be based on conventional methods for the development of rocket engine geometries found in literature [32]. Experimental and analytical methods are coupled on the proof-of-concept model to develop the combustor and cooling system of the large-scale design. Numerical methods are employed to provide heat transfer characteristics in high temperature, high heat flux environments for the prediction of cooling requirements and the optimization of thermal management systems in open-cycle MHD combustors.

1.4 Practical Relevance

Improving the overall efficiency of power plants may be achievable through the integration of an open-cycle MHD system, such as the one presented. The combustion products leaving the MHD channel can be recovered when integrated with a bottoming steam turbine. Theoretical studies show that this configuration could result in efficiencies at least 20% larger than conventional power plants [33]. As the operating temperatures of the generator surpass those of any other process, the integration of an open-cycle MHD combustor would still improve the efficiency of existing cycles. A historical precedent exists in the development of combined MHD plants: in 1981 the USA established a 50 MW_{th} coal-based facility in Montana, while the Shanghai Power Plant Research Institute a pilot-scale MHD steam combined plant during the 60s [8]. The physical limitations that caused the MHD program to end in past decades may be tackled with existing and developing technology. The cooling system design presented herein allows for the system to function on steady-state near-stoichiometric conditions with no diluent gases, increasing

the efficiency of this component. As the temperature is greatly diminished when exiting the MHD channel, hot gases can be readily employed in conventional power generation configurations. The oxidizer and fuel flow rates supplied to the existing design may be adjusted to match the desired turbine inlet temperatures in the bottoming cycle. This allows for combustor integration into heritage power plants with lower temperature limits. At its maximum operating condition, the UTEP MHD combustor may be used for next-generation zero emission power plant configurations, where turbine inlet temperature may exceed 1200 °C. In addition to this, the water-based cooling system in the current combustor may be integrated with internal turbine blade cooling configurations.

1.5 Commercialization Potential

Retrofitting and novel concept power plants must be analyzed in terms of economic feasibility through a life cycle analysis. Initial costs would be a determining factor for setup location, as maintenance costs are reported to be relatively low for this type of system. Additional parameters to be accounted for are those of local fuel availability and cost, as well as unit reliability and service duration [33]. The integration of an open cycle MHD system is best suited to intermediate and base load plants [33]. Theoretical analyses performed in the 1970s and 1980s [8] [33] indicate that a combined cycle MHD plant would be able to significantly reduce costs per kW-hr through increased efficiencies. This makes the MHD system a prime candidate for commercial implementation if the overall plant reliability is high enough. In regards to the design presented here, the commercialization of the UTEP MHD combustor may be possible through a second scaling procedure or the integration of the 1-MW design in a cannular configuration. The integration of 3-D printing technologies in the combustor may be used to reduce lead times; nevertheless, a cost comparison must be performed with traditional methods due to the required manufacturing volumes. Due to its similarity with rocket engines and supersonic output, the developed 60 kW-scale MHD prototype may be integrated as high-velocity component of dynamic

remotely operated navigation equipment (DRONE) systems. Though the current device requires steady-state water cooling, the combustor may be adapted to operate for short pulses to deliver thrust as required. In addition to this, its use as a small-scale power generation device must be investigated for remote locations, where fuel transportation costs are significant. The cooling channels developed for both prototypes may be employed in the optimization of high-velocity oxy-fuel thermal spray guns. These devices operate under similar constraints as the ones presented, and typically employ air or water cooling. Likewise, the cooling system may also be implemented in next generation oxy-fuel devices intended for use in near-stoichiometric conditions. The channels could be used alongside a thermal barrier coating to increase the safety factor of a power generation device and prevent corrosion.

Chapter 2: Design Methodology

An MHD-based direct power extraction device capable of delivering gases at temperatures exceeding 2800 K and a Mach number of 2 was designed and tested for this study. Since this system is planned for use in power generation systems, a design constraint used for the current study was an assumption of steady-state operation. The experimental apparatus consists of a pressure-fed fuel and oxidizer delivery system, combustion chamber and converging-diverging De Laval nozzle, shown in Figure 2. For this purpose, a 60 kW combustor was designed. Combustion temperature is expected to remain near 2800K, this temperature is sufficient to ionize a seeded particle flow in an MHDA system. This constraint is imposed by the minimum combustion temperature for effective electrical conductivity established by Kayukawa [4]; this value corresponds to 2300 K. The upper limit of exit gas temperature is given by the flow reaction; though chamber temperatures are expected to exceed 3300 K, energy conversion in the nozzle reduces this figure.

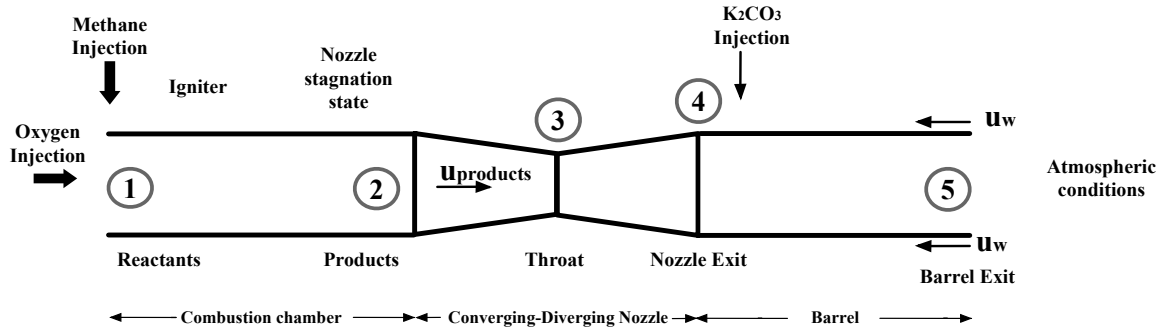


Figure 2: Schematic of the MHD open-cycle combustor.

2.1 Combustor and Nozzle Design

While the performance of the system is significantly impacted by ignition, injection and combustion efficiencies of the species, the development of the combustion chamber and nozzle geometry remains exceedingly empirical [34]. The power output of a MHD-based generator increases in a proportional manner to the square of gas velocity [35]. While power density is shown

to increase with velocity, efficiency drops at high Mach numbers. An optimum Mach number of 2.5 is quoted by a study performed at NASA Lewis research center [36]. A nozzle exit Mach number of 2 has been proposed for this study as a compromise between the proportional velocity effects and inversely proportional influence of pressure, increasing potential power extraction. Thus the selection of an expansion area ratio in the nozzle section was critical to meeting the exit gas requirements.

The design of this geometry was carried out through the assumption of constant-pressure combustion in the chamber and isentropic expansion in the nozzle. The assumption of isentropic expansion has been established in nozzle characterization efforts found in similar studies centered on semi-empirical relations [37] [38]. Injection pressures were calculated based on nozzle stagnation states to be at least 10% larger than the desired chamber pressure. Methane and oxygen were assumed to react with sufficient residence time in the combustion chamber to attain full equilibrium. A composition of oxy-methane was investigated at constant pressures of 3-8 bar and equivalence ratios from .9-1.2. From these equilibrium states, gaseous properties including adiabatic flame temperatures were investigated. Thermodynamic expansion of the gas within the nozzle was assumed to be reversible and adiabatic, and the viscous effects of the boundary layer were neglected.

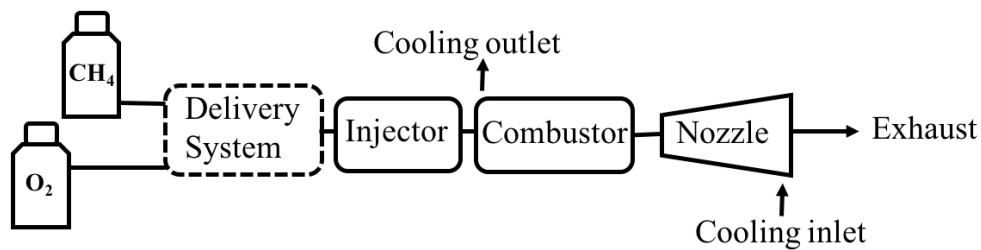


Figure 3: Block layout of experimental apparatus

Equilibrium mixture properties were determined through NASA's chemical equilibrium applications (CEA) code [39]. In the analysis, thermal transport properties were considered in frozen equilibrium at the nozzle inlet. This tool allowed for quick estimates of temperature and velocity as a function of propellant combination, chamber pressure and nozzle contraction/expansion ratios. In regards to nozzle characteristics, an expansion ratio of 1.85 was selected to achieve the required velocity parameter. A nozzle expansion ratio of 1.85 was selected to achieve the required exit velocity, providing gases at a Mach number that exceeds 1.8. A divergence half-angle of 2 degrees was selected to achieve gradual thermodynamic expansion. This geometry necessitates a minimum chamber pressure of 655 KPa (95 psia) to achieve ideal expansion in atmospheric conditions in accordance to isentropic flow relationships.

The effects of reactant stoichiometry on adiabatic flame temperatures are presented in Figure 4 for chamber pressures of 4-8 bar. From the figure, it is apparent that adiabatic flame temperatures vary by less than 10% when chamber pressure is doubled. The combustor design process required that the structure withstand the high-temperature environment characterized by the reaction. A material selection process was performed to find suitable candidates.

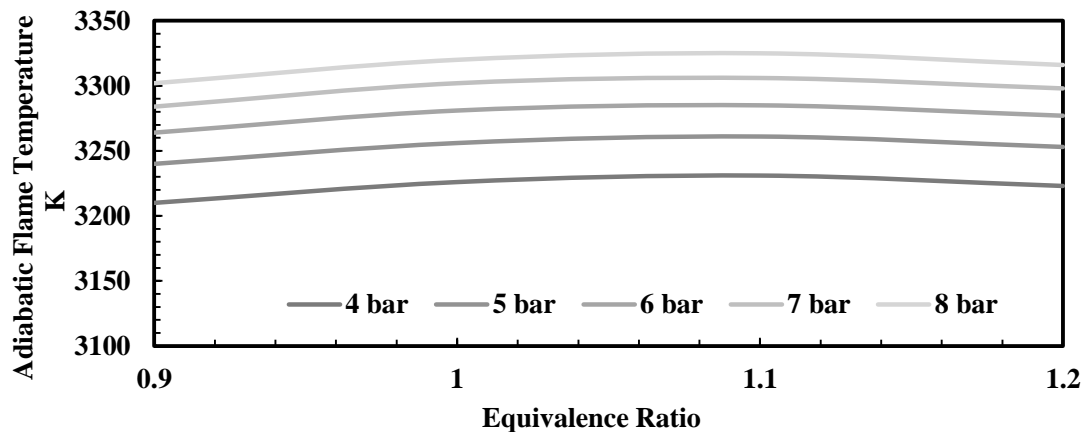


Figure 4: Adiabatic flame temperatures of CH₄-O₂ for pressures of 4-8 bar

Inconel 718, a nickel-chromium Superalloy was chosen due to its high melting point (1300 °C) and yield strength characteristics at elevated temperature environments. The selection of such material required that the critical pressure of the combustor be set at 7.6 bar, assuming a maximization of adiabatic flame temperature. A flame temperature of 3315 K was employed to estimate heat rejection to the walls, corresponding to an equivalence ratio of 1.1.

2.2 Cooling System Design

The heat transfer from the combustion gas to the wall and coolant was characterized through the use of a simplified thermal resistance model. This heat transfer model effectively accounts for the forced convective combustion gas flow, gas product boundary layer, wall conduction, coolant boundary layer and forced convection caused by coolant flow. A schematic of the thermal resistance model is shown in Figure 5. The cooling design balanced the heat transfer properties of the system and yield strength properties at the elevated wall temperature. For the system, the location of largest heat flux was used as the design point for the combustor and cooling system.

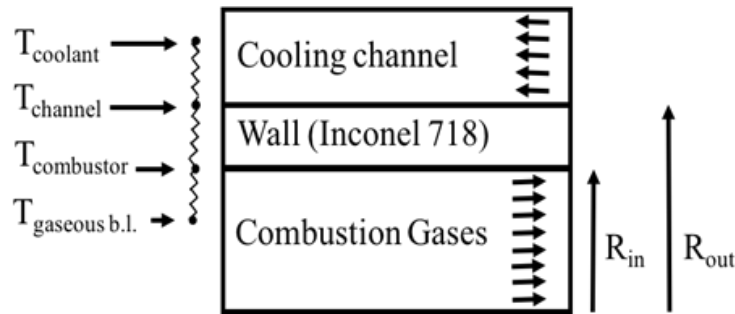


Figure 5: Thermal-resistance model used for the analysis of the combustor and nozzle

The convective characteristics of combustion gases are approximated through the use of the Bartz correlation equation for nozzle heat transfer [32], shown in Equation 1. This correlation estimates the gaseous convective heat transfer coefficient through a combination of gas stagnation

properties, boundary layer effects and nozzle throat geometry.

$$h_g = \left[\frac{0.026}{D_t^{0.2}} \left(\frac{\mu_{ns}^{0.2} c_{p_{ns}}}{Pr_{ns}^{0.6}} \right)_{ns} \left(\frac{p_{cns} g}{c^*} \right)^{0.8} \left(\frac{D_t}{R_{ct}} \right)^{0.1} \right] \left(\frac{A_t}{A} \right)^{0.9} \sigma \quad [1]$$

However, it has been shown in previous studies that Equation 1 results in the over prediction of the heat transfer characteristics at the throat by as much as 40% [18]. Therefore, a reduction in the heat transfer coefficient is assumed of 40%. Factors that are quoted as impacting the accuracy of this correlation include flow instabilities, combustion efficiency variations and the production of solid deposits in the nozzle wall [32]. Using this correction factor the heat flux is calculated using the corrected heat transfer coefficient, a wall temperature of 550 °C, and the boundary layer temperature, calculated using Equation 2. The choice of wall temperature originates from the material's behavior in extreme environments. Though Inconel 718 possesses outstanding properties at room temperature, its yield strength exponentially decreases when exposed to temperatures above 600 Celsius. This design criterion balanced thermal stresses introduced by elevated heat transfer rates to the combustor wall.

$$T_{aw} = T_{cns} \left[\frac{1+r \left(\frac{\gamma-1}{2} \right) M_x^2}{1+\left(\frac{\gamma-1}{2} \right) M_x^2} \right] \quad [2]$$

Iterative design calculations using these the material stress limitations, chamber temperatures, and chamber pressures resulted in a calculated wall thickness of 0.9-1.2 mm. This thickness results in a total stress of 610 MPa, when maintaining a hot-side wall temperature of 550 Celsius. The yield strength of Inconel 718 at this temperature corresponds to 995 MPa. These calculations were performed under the assumption of a one-dimensional, Cartesian estimate. Equation 3 was employed to relate the combination of mechanical and thermal stress to wall thickness, heat flux and material properties. This equation estimates total compressive stress in the combustion chamber.

$$S_C = \frac{(p_{co}-p_g)R}{t} + \frac{Eaqt}{2(1-\nu)k} \quad [3]$$

While the minimization of wall thickness results in a smaller thermal stress component, lowering this value outputs larger coolant-side wall temperatures. This results in an array of issues related to coolant selection, coolant flow properties, and evaluations of overall coolant effectiveness for heat removal in the system. An equilibrium between maximum temperature and wall thickness was necessary to minimize failure risk.

The choice of coolant selection was motivated by a steady-state operation constraint on the device. Due to the current design's status as a terrestrial energy system, weight limitations were nonexistent when considering the cooling structure. Deionized water is selected as the coolant fluid due to the high thermal capacity and availability of thermodynamic properties.

The coolant convection process was modeled with through Equation 4, which shows a Nusselt form empirical correlation employed in the design of regenerative cooling channels [32]. Equation 4 was rearranged to relate coolant velocity to channel hydraulic diameter, accounting for coolant properties including viscosity, density and heat capacity. A channel hydraulic diameter of 2 mm was chosen to minimize pressure drop in the passages while minimizing required pump flow capabilities. A maximum temperature of 130 Celsius in the coolant wall domain was established as a constraint to minimize the risk of cavitation in the channel environment. This value implies that the channels must be continuously pressurized above 277 KPa (40 psi). A high-head, low-flow pump configuration was preferred to satisfy the flow requirements to remove the heat rejection rate at the nozzle throat.

$$Nu = C_1 Re_{co}^{.8} Pr_{co}^{.4} \left(\frac{\mu_{co}}{\mu_{w,co}} \right)^{.14} \quad [4]$$

Structural integrity of the overall combustor-nozzle system was improved by the inclusion of channels. Considering the chamber wall thickness range of 0.9-1.2 mm, placement of ribs in the cooling structure was necessary to provide a stable support and surface to surface interface to the exterior shell in the design. The number of channels was maximized to enhance heat transfer. The

maximum number of elements is a function of throat diameter, wall thickness and desired coolant hydraulic geometry. A six channel structure was selected for the cooling of the combustion chamber and nozzle. A summary of the design parameters and the heat flux characteristics of the device is outlined in Table 1.

Table 1: Overall design parameters

<u>Parameter</u>	<u>Symbol</u>	<u>Value</u>	<u>Units</u>
Chamber Pressure	P_c	758.40	KPa
Chamber Temperature	T_c	3315	K
Gas convective heat transfer coefficient	h_g	3.04	$\frac{MW}{m^2 - K}$
Heat Flux	\dot{q}	7.65	$\frac{MW}{m^2}$
Coolant convective heat transfer coefficient	h_c	69.60	$\frac{MW}{m^2 - K}$
Coolant flow rate requirement	\dot{V}_c	16.8	LPM

The inlet, outlet cooling channel manifold and obstruction of the coolant flow locations for sensors and instrumentation was also a significant design consideration. In this design, to accommodate measurement devices and ignition, channel flow was intermittently interrupted by the placement of chamber pressure and temperature sensors, and ignition ports. The final design criteria in the development of the active thermal protection system was minimization of heat

rejection to the walls. This criterion impacts the overall open-cycle MHD combustor efficiency, as wall cooling affects the performance of the MHD energy extraction from the gases.

2.2.1 Estimates of Temperature through the Conduction Equation

The analytical calculation of temperature is determined by solving the energy equation assuming one-dimensional steady-state heat transfer in the radial direction. A heat flux boundary condition is assumed on the hot-gas side and assumed equivalent to the convective heat transfer on the coolant side of the flow. Inside of the combustor, the heat flux was computed using Bartz equation throughout the nozzle and inner boundary layer temperature. Bartz equation is calculated using the boundary layer correction factor σ , in Equation 5. Temperature-dependent properties of the wall material are assumed to use the localized average wall temperatures through an iterative process. Equation 6 is then used to calculate temperatures in the wall. These temperatures are calculated at different locations upstream, at the throat, and downstream of the throat.

$$\sigma = \frac{1}{\left[\frac{1}{2} \frac{T_{wg}}{(T_c)_{ns}} \left(1 + \frac{\gamma-1}{2} M_x^2 \right) + \frac{1}{2} \right]^{.68} \left[1 + \frac{\gamma-1}{2} M_x^2 \right]^{.12}} \quad [5]$$

$$T_r = \left(\frac{-\dot{q} r_1}{k} \right) \ln(r) + \left(\frac{h_{co} \left(\frac{\dot{q} r_1}{k} \ln(r_2) + T_{co} \right) + \dot{q}}{h_{co}} \right) \quad [6]$$

2.3 Technical Approach

2.3.1 Experimental Apparatus

2.3.1.1 Combustor

Figure 6 shows an isometric exploded view of the MHD test article, while Figure 7 displays the real model. The thrust chamber consists of three distinct parts (combustion chamber, nozzle, barrel) that have been fabricated from a single portion of superalloy Inconel 718. Cooling channels

were constructed through the electrical discharge machining method (EDM). The milled channel structure, injector attachment, and all additional connections have been laser welded with two symmetrical shells to ensure a full isolation of the coolant domain. Methane is delivered to a fuel manifold that equally distributes the fuel into four tangential ports in the injection plane. The swirl coaxial injector attachment is based on a previous design intended for use in attitude control. Manifold inlet angle has been optimized through numerical means. Gaseous oxygen is injected in the axial flow direction, orthogonal to the tangential fuel inlets. The total length of the test article, spanning from the location of oxygen injection to the end of the seed-injection barrel is 12 cm. Ignition energy is provided by a spark-activated system near the fuel injection, within the chamber. Six rectangular cooling channels deliver water at a flow rate of 16 SLPM. The channels are linked through an internal manifold fed by two 6.4 mm tubular inlets, designed to interface with compression-type fittings. In this configuration, flow enters at the nozzle exit and follows a counterflow path with gaseous flow. The cooling channels regroup in a region of low heat flux near fuel injection to later exit through conduits that mirror the entrance region. Two 4 mm obstructions in the coolant passage flow paths were implemented to introduce static pressure and temperature measurement devices in the combustion chamber. A single 8 mm obstruction in the coolant flow path provides sufficient space for the spark ignition system in the combustion chamber. At these locations, the surrounding channels are interrupted to enhance localized heat transfer and minimize stagnation regions. A summary of the combustor operating and geometrical parameters relevant to this study can be found in Table 2.

Table 2: Operational and geometrical parameters of the combustor

Parameter	Value	Units
Power Input	60	kW
Design Temperature	3315	K
Design Pressure	760	kPa
Throat Diameter	3.7	mm
Chamber Diameter	10	mm
Wall Thickness	1	mm
Nozzle Exit Area Ratio	1.85	

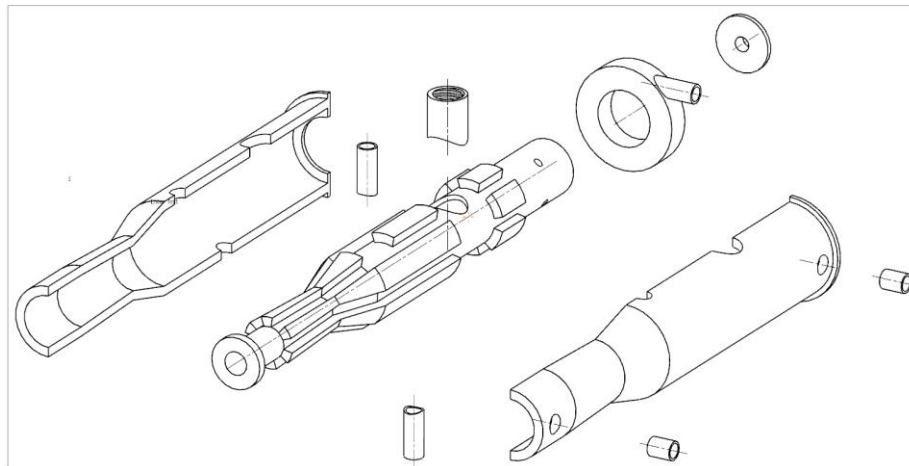


Figure 6: Exploded view of combustor system components

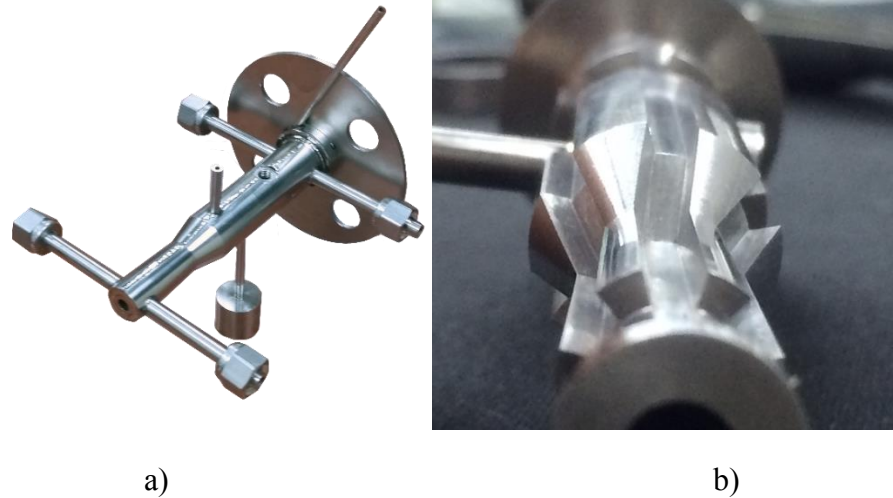


Figure 7: a) Isometric view of the 60 kW combustor b) Milled cooling channels

2.3.1.2 Feed System

The coolant and propellant feed system is outlined in Figure 8. A centrifugal pump was chosen in accordance to cooling requirements. A system of twelve 12.7 mm ball valves was used to control water flow. Three drains are integrated into the system allowing for the safe and effective clearing of all sections. Two ports were integrated for the implementation of air when clearing the line or checking for leaks. A manual proportional valve in the coolant delivery allows for flow rate calibration between test sessions, in addition to a turbine flow meter to monitor volumetric flow levels. Two static pressure transducers and J-type thermocouples were integrated at locations prior to and following the test article to monitor pressure losses and temperature gains in the combustor. A 208-liter reservoir provides sufficient fluid volume to safely operate oxy-fuel combustion in pulse or continuous modes. The gaseous delivery system facilitates precise metered flows of gaseous nitrogen, oxygen and methane. Six solenoid valves remotely control pre-set flows in all gaseous lines. Flows are calibrated with inert gases prior to hot-firing sessions.

A total of four static pressure transducers measure values in the oxidizer, fuel, inert gas and coolant lines, while a fifth provides an estimation of chamber pressure. One K-type surface

thermocouple provides estimates of chamber wall temperature. All test sessions were conducted inside the Kevlar-lined bunker system; operators remained inside an adjacent control room. LabView software is employed to remotely handle operation using custom manual and automatic programming. Figure 9 outlines the LabView interface generated for the steady-state monitoring and operation of the system.

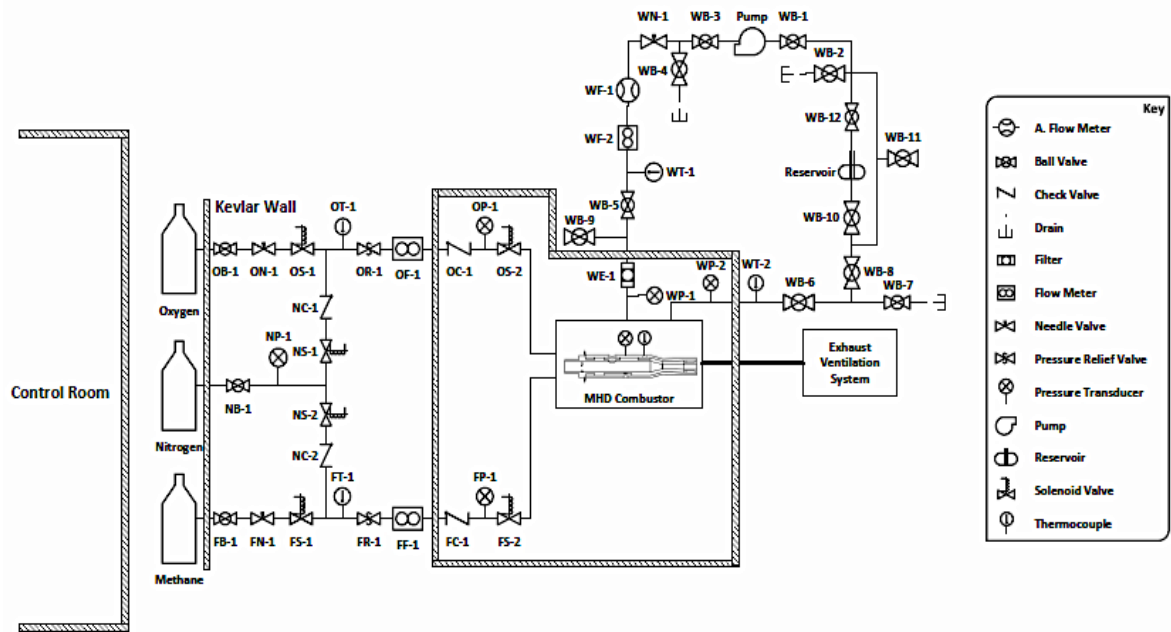


Figure 8: Experimental setup feed system layout

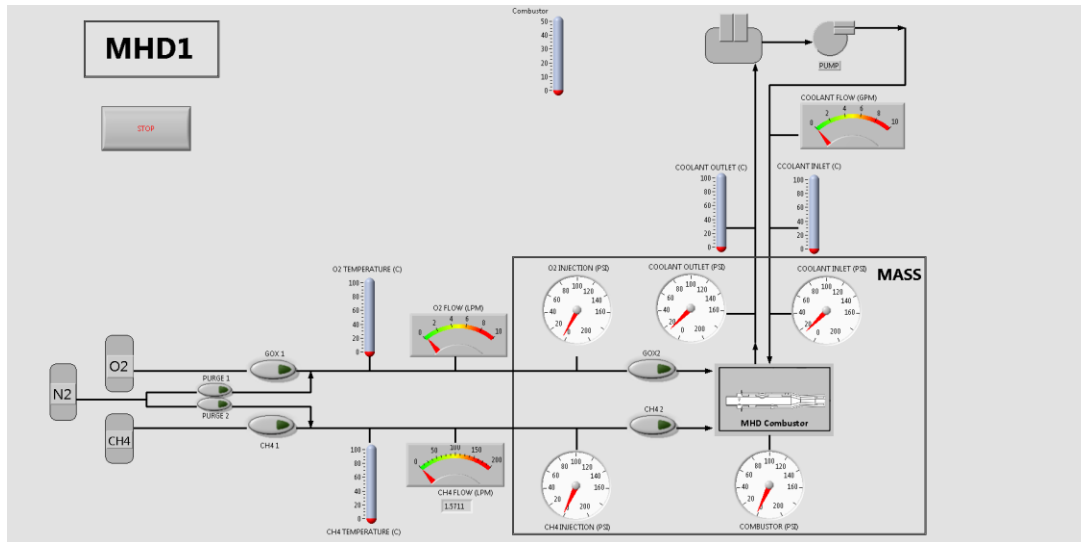


Figure 9: LabView interface

2.3.2 Experimental Approach & Test Matrix

The combustor was tested for lengths of time between two to five minutes, with preliminary runs being conducted at intervals of 2-10 seconds. The test conditions employed in the investigation are shown in Table 3. Automated operations were made possible through the use of LabView to open and close system solenoid valves. Valve delay time was neglected in the calculation of total test times. Oxidizer and fuel tank pressures were determined through cold flow tests. Following each test, purging operations were performed to clear the area of combustible mixtures prior to operators entering the bunker area. Coolant flow rate was maintained constant at 17.8 LPM throughout all tests. This value was 6% higher than the computed minimum flow of 16.8 LPM. Overall water pressure drop remained stable at 482 KPa (70 psi), not accounting for piping losses. Adjusted for the channel domain, this value drops to 262 KPa (38 psi). Minimum water pressure remained above 792 KPa (115 psia) for all cases. The maximum theoretical chamber temperature (3315 K) corresponds to Test 2 at an equivalence ratio of 1.1.

Table 3: Experimental tests performed using the combustor

Test	Fuel Flow Rate (SLPM)	Oxidizer Flow Rate (SLPM)	Equivalence Ratio	Duration (s)
1	85	155	1	120
2	95	155	1.1	120
3	85	155	1	120
4	85	155	1	300

Based on experimental measurements, the overall heat rejection rate to the cooling fluid per power input to the system is computed using Equation 7. This parameter is calculated because, unlike other systems, it is not desired to cool the combustion chamber to limits that may reduce the power generation potential of the system or quench the flame. This parameter is also used to gauge the heat removal capacity of the cooling unit.

$$Q_R = \frac{\dot{m}_{to} C_p \Delta T}{LHV * \dot{m}_f} \quad [7]$$

Where \dot{m}_{to} represents the mass flow rate of water used for cooling, C_p is the specific heat of water, ΔT is the temperature difference of the water at the inlet and exit of the combustor, LHV is the lower heating value of the methane, and \dot{m}_f represents the methane flow rate into the combustor.

Chapter 3: Numerical Methodology (60 kW Combustor)

A numerical model for the characterization of the 60 kW combustor has been developed for a thorough comparison to experimental data and the one-dimensional methods employed in the design. The development of this simulation stems from the gap found in literature concerning the accuracy of established nozzle-cooling methods. The gathered results are thought to be of value for the design of the 1-MW scale combustor and all future models based on this design.

A fully-coupled 2-D numerical axisymmetric model was developed. This incorporates the combustion, wall and cooling domains and is integrated in commercial software ANSYS FLUENT. The use of all three domains in a single simulation eliminates the necessity for iterations required in semi-coupled or decoupled methods. Estimates of combustion gas characteristics are available through the non-premixed combustion model; similarly, the method allows for an estimate of wall surface temperatures and heat flux values. Results found from this model may be incorporated into a 3-D setup to investigate specific cooling channel geometries.

3.1 Theory

The software solves the mass, momentum, species, and energy governing equations in Equations 8-17.

$$\frac{\partial \rho}{\partial t} + \frac{\partial}{\partial x}(\rho v_x) + \frac{\partial}{\partial r}(\rho v_r) + \frac{\rho v_r}{r} = 0 \quad [8]$$

$$\begin{aligned} \frac{\partial}{\partial t}(\rho v_x) + \frac{1}{r} \frac{\partial}{\partial x}(r \rho v_x v_x) + \frac{1}{r} \frac{\partial}{\partial r}(r \rho v_r v_x) = & -\frac{\partial p}{\partial x} + \frac{1}{r} \frac{\partial}{\partial x} \left[r \mu \left(2 \frac{\partial v_x}{\partial x} - \frac{2}{3} (\nabla \cdot \vec{v}) \right) \right] + \\ \frac{1}{r} \frac{\partial}{\partial r} \left[r \mu \left(\frac{\partial v_x}{\partial r} + \frac{\partial v_r}{\partial x} \right) \right] & \end{aligned} \quad [9]$$

$$\begin{aligned} \frac{\partial}{\partial t}(\rho v_r) + \frac{1}{r} \frac{\partial}{\partial x}(r \rho v_x v_r) + \frac{1}{r} \frac{\partial}{\partial r}(r \rho v_r v_r) = & -\frac{\partial p}{\partial r} + \frac{1}{r} \frac{\partial}{\partial x} \left[r \mu \left(\frac{\partial v_r}{\partial x} + \frac{\partial v_x}{\partial r} \right) \right] + \\ \frac{1}{r} \frac{\partial}{\partial r} \left[r \mu \left(2 \frac{\partial v_r}{\partial r} - \frac{2}{3} (\nabla \cdot \vec{v}) \right) \right] - 2 \mu \frac{v_r}{r^2} + \frac{2}{3} \frac{\mu_d}{r} (\nabla \cdot \vec{v}) + \rho \frac{v_z^2}{r} & \end{aligned} \quad [10]$$

Where,

$$\nabla \cdot \vec{v} = \frac{\partial v_x}{\partial x} + \frac{\partial v_r}{\partial r} + \frac{v_r}{r} \quad [11]$$

The realizable k- ϵ model was implemented to model turbulence in the flow. The model requires two additional transport equations to be included for turbulent kinetic energy and dissipation, Equations 12 and 13.

$$\frac{\partial}{\partial t}(\rho K) + \frac{\partial}{\partial x_i}(\rho K v_i) = \frac{\partial}{\partial x_j} \left[\left(\mu + \frac{\mu_{tu}}{C_{ke}} \right) \frac{\partial K}{\partial x_j} \right] + G_k + G_b - \rho \epsilon - Y_M + S_{ke} \quad [12]$$

$$\frac{\partial}{\partial t}(\rho \epsilon) + \frac{\partial}{\partial x_i}(\rho \epsilon v_i) = \frac{\partial}{\partial x_j} \left[\left(\mu + \frac{\mu_{tu}}{C_\epsilon} \right) \frac{\partial \epsilon}{\partial x_j} \right] + \rho C_2 S_\epsilon - \rho C_3 \frac{\epsilon^2}{K + \sqrt{\nu \epsilon}} + C_{2\epsilon} \frac{\epsilon}{K} C_{4\epsilon} G_b + S_\epsilon \quad [13]$$

Where G_k corresponds to the generation of turbulent kinetic energy due to mean velocity gradients, and G_b due to buoyancy effects.

A non-premixed combustion model is used to estimate gaseous reaction properties. The model simplifies thermochemistry to a single factor, mixture fraction (f). All relationships between turbulence and chemistry are computed prior to the start of the simulation through a probability density function (PDF), which quantifies the probability of finding a variable Z , corresponding to the mass fraction of species in the reactants [40]. This model was chosen since it accounts for dissociation effects in the reaction, allowing for an accurate flame temperature estimate. The energy equation utilized in the modeling of the non-adiabatic non-premixed combustion model is presented in Equation 14. At the combustor wall, this relationship takes the form of Equation 18.

$$\frac{\partial}{\partial t}(\rho H) + \nabla \cdot (\rho \vec{v} H) = \nabla \cdot \left(\frac{kq}{C_p} \nabla H \right) + S \quad [14]$$

Where,

$$H = \sum_j Z_j H_j \quad [15]$$

and S represents the viscous dissipation term and is defined in Equations 16 and 17, while Z_j represents the mass fraction of species j .

$$S = \nabla(\overline{\tau_{\text{eff}}} \cdot \mathbf{v}) - \mathbf{v} \cdot (\nabla \overline{\tau_{\text{eff}}}) \quad [16]$$

$$\tau_{\text{eff}} = \mu_{\text{eff}} \left(\left(\frac{\partial v_j}{\partial x_i} + \frac{\partial v_i}{\partial x_j} \right) - \frac{2}{3} \frac{\partial v_k}{\partial x_k} \delta_{ij} \right) \quad [17]$$

$$\frac{\partial}{\partial t}(\rho\eta) + \nabla \cdot (\rho \vec{v}\eta) = \nabla \cdot (k \nabla T) \quad [18]$$

Equation 19 represents the calculation used for mixture fraction, where Z_i denotes the mass fraction of local element i . The equation of state employed in the non-premixed model is the ideal gas law, represented in Equation 20.

$$f = \frac{Z_i - Z_{i,\text{ox}}}{Z_{i,f} - Z_{i,\text{ox}}} \quad [19]$$

$$p = \rho PV = mRT \quad [20]$$

The use of the non-adiabatic model implies that the instantaneous species of density, temperature and mass fraction take the form of Equation 21, which relates instantaneous mixture fraction f and instantaneous enthalpy H^* .

$$\phi_i = \phi_i(f, H^*) \quad [21]$$

$$H^* = \sum_j Z_j H_j = \sum_j Z_j \left[\int_{T_{\text{ref},i}}^T C_{p,i} dT + \eta_j^0(T_{\text{ref},j}) \right] \quad [22]$$

Turbulent fluctuations must be accounted for through means of a joint PDF. A simplification of this PDF, assuming enthalpy fluctuations are independent of heat losses, allows

for its sole dependence on mixture fraction [40]. Equation 23 is derived the assumption from Equation 21. Thus, the determination of time-averaged species is found from Equation 24, corresponding to the modeled transport equation for time-averaged enthalpy $\overline{H^*}$.

$$\overline{\phi_i} = \phi_i(f, \overline{H^*}) \text{PDF}(f) df \quad [23]$$

$$\frac{\partial}{\partial t} (\rho \overline{H^*}) + \nabla \cdot (\rho \vec{v} \overline{H^*}) = \nabla \cdot \left(\frac{k_t}{c_p} \nabla \overline{H^*} \right) + S \quad [24]$$

3.2 Geometry and Boundary Conditions

Figure 10 shows a schematic diagram of boundary conditions within the domain. Input values and boundary conditions are summarized in Table 4. The mesh is composed of 95,000 quadrilateral elements and integrates horizontal and vertical biases towards the chamber walls and the nozzle throat. Quadrilateral mapping was used in segmented face regions to minimize overall element skewness. Average element quality for the mesh is 0.75. To ensure the validity of the method, a mesh independence study has been conducted, with its results summarized in Chapter 4.

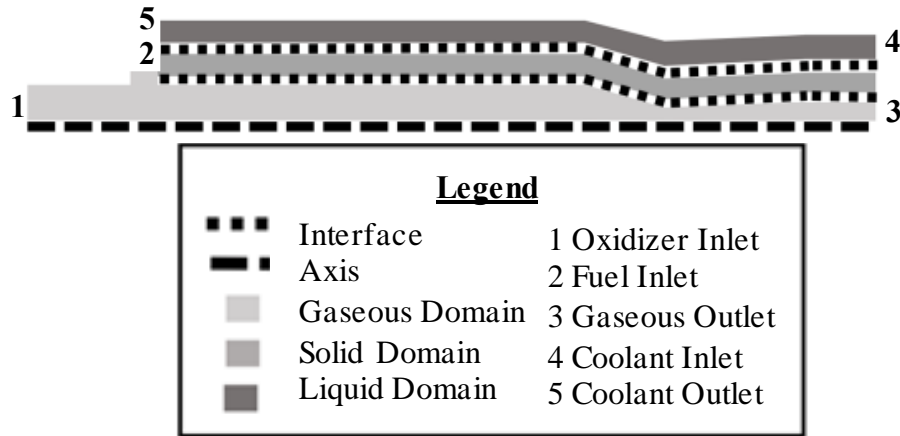


Figure 10: Computational domain with boundary conditions labeled

The inlet mass flow boundary conditions mirror the values described in Chapter 2, corresponding to Test case 2. Temperature-dependent properties of Inconel 718 have been adapted as a customized material in the solid domain for determination of surface and inner wall temperatures. A scalable wall function has been integrated into the turbulence model. This function limits the minimum value of y^+ , ensuring the solver acts at the intersection of the linear and log law profiles [41] [42]. The COUPLED algorithm and pseudo-transient solvers are employed in the present model. A second order solution was finalized through the resolution of a first order approximation. The model was judged as converged once all residuals remained unchanged for 1000 iterations. All residual parameters fell below an established threshold of 10^{-6} to 10^{-4} .

Table 4: List of boundary conditions used in 2-D numerical model

	Input
Models	<p>Energy-ON</p> <p>Viscous-Realizable k-epsilon, Scalable Wall Function</p> <p>Species-Non-premixed combustion</p> <ul style="list-style-type: none"> • Inlet diffusion-ON • Compressibility effects-ON • Fuel stream rich flammability limit-0.27 • Non-adiabatic • Equilibrium pressure 760 kPa (110 psi) • Mass fraction of CH₄-1 • Mass fraction of O₂-1
Materials	<p>PDF Mixture</p> <ul style="list-style-type: none"> • C_p-Mixing law • Thermal conductivity .0454 W/m-K • Viscosity 1.72 E-5 kg/m-s <p>Inconel 718</p> <ul style="list-style-type: none"> • Density 8290 kg/m³ • C_p-433 J/K • Thermal conductivity – user function <p>Water- Liquid</p> <ul style="list-style-type: none"> • Density 998 kg/m³ • C_p-4182 J/K • Thermal conductivity .6 W/m-K

	<ul style="list-style-type: none"> • Viscosity 0.001003 kg/m-s
Boundary Conditions	<p>Fuel Inlet:</p> <ul style="list-style-type: none"> • Mass flow rate- 0.001 kg/s • Hydraulic diameter- 1.8 mm • Mean mixture fraction -1 • Turbulent Intensity- 3.5% <p>Oxidizer inlet:</p> <ul style="list-style-type: none"> • Mass flow rate-0.0036 kg/s • Hydraulic diameter- 10 mm • Turbulent Intensity- 3.4% <p>Gas outlet:</p> <ul style="list-style-type: none"> • Atmospheric pressure (initial) • Turbulent Intensity- 7% <p>Water inlet:</p> <ul style="list-style-type: none"> • Velocity-11 m/s • Turbulent Intensity- 4.54% <p>Water outlet:</p> <ul style="list-style-type: none"> • Atmospheric pressure (initial) • Turbulent Intensity- 4.5%
Solution Initialization	Standard-Oxidizer Inlet

3.3 Characterization of Geometry into Axisymmetric Model

While the combustor's gaseous domain could be categorized as fully symmetric, fuel injection parameters required manipulation to characterize the swirl coaxial configuration. Four fuel injection ports were converted into a ring with constant inlet velocity through the conservation of mass equation. The channel geometry was modeled through the assumption of constant convective properties. Though the physical model included support structures that helped maintain a constant hydraulic diameter, characterizing a steady gap in 2D will yield variable velocities. However, if the resulting channel area is maintained, the hydraulic diameter will not be constant due to the same reason. A manipulation of a Nusselt-type correlation and the conservation of mass equation was performed to characterize the 2-D channel geometry in the profile. Equation 25 describes the rearranged Sieder-Tate correlation, where C is a constant that contains steady coolant properties and the required convective heat transfer coefficient. Hydraulic diameter is characterized as the difference between outer and inner diameters of an annulus. As such, cross-sectional channel area is described by Equation 26 at any location of the channel. The conservation of mass equation is described by Equation 27. Density for this case is assumed to be steady due to the coolant being incompressible.

$$V = \left(\frac{D_{out} - D_{in}}{C} \right)^{.25} \quad [25]$$

$$A = \frac{\pi}{4} (D_{OUT}^2 - D_{IN}^2) \quad [26]$$

$$\rho_1 A_1 V_1 = \rho_2 A_2 V_2 \quad [27]$$

An initial geometrical condition is described as a starting point, state 1. A 2-mm gap in the combustion chamber domain is assumed for this case. Employing the modified Sieder-Tate Equation 25, the channel velocity requirement is found to be 11 m/s. A system constant C2 is characterized at state 1 through Equation 28.

$$C_2 = \frac{\dot{m}}{\rho} = A * V \quad [28]$$

Rearranging conservation of mass, Equation 27, and substituting the modified Sieder-Tate Equation 25 for velocity and system constant C₂, Equation 29 is obtained. In this equation, D_{in} is characterized as the domain's local shell diameter. Outer channel diameters are obtained through the solution of this equation for all points in the nozzle and combustor. The obtained profile will maintain convective heat characteristics and it is expected that this may also help to replicate, albeit in a simplified manner, a three dimensional geometry.

$$\frac{C_2}{A} = \frac{C_2}{\frac{\pi}{4}(D_{out}^2 - D_{in}^2)} = \left(\frac{(D_{out} - D_{in})}{C} \right)^{1/4} \quad [29]$$

Chapter 4: Results & Discussion (60 kW Combustor)

4.1 Experimental Results

The volumetric flow rate of methane and oxygen were calculated to correspond to theoretical O/F and chamber pressure. The values of the flow were calculated with NASA CEA and verified through experimental cold flow tests. The maximum obtained chamber pressure was 560 kPa (81 psia), 27% lower than the predicted one as 110 psia. Differences in this reading may be due to the pressure transducer's axial location, as well as the accumulated errors of the flow. It was also observed that the combustion pressure fell below a negative value when the valve shutdown operation was performed. The minimum required pressure for an ideal expansion with the nozzle geometry is 95 psia. This implies that the flow conditions correspond to a slightly overexpanded state. Values of pressure and volumetric flow rates were observed to stabilize within the first 50 seconds of the test; fluctuations of these values were less than 5% after this timeframe. A plot of the methane and oxygen flow rates is shown in Figure 11. An equivalence ratio of 1.05 was calculated according to the stabilized values; the design equivalence ratio was 1.1.

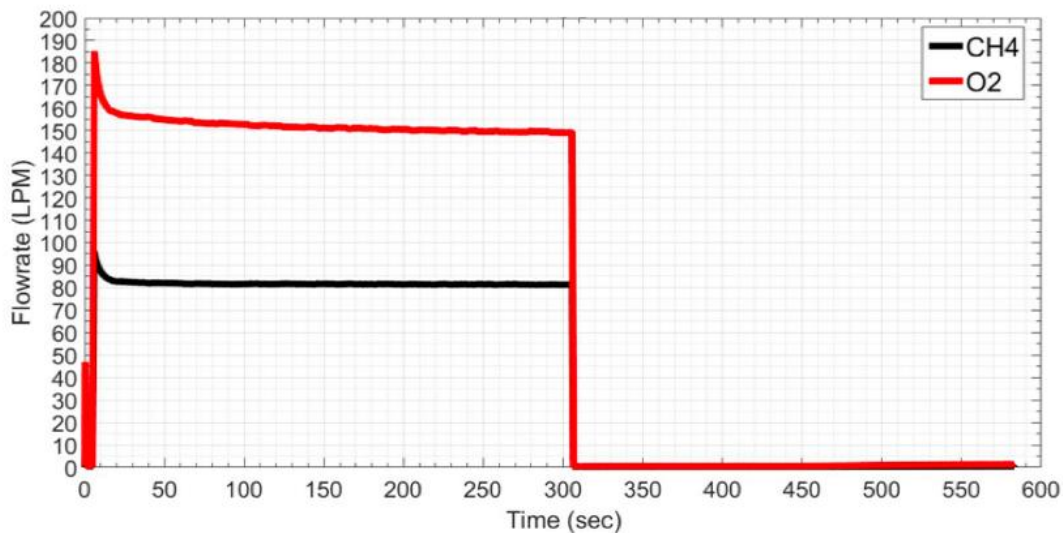


Figure 11: Gas flow rates during 5 minute test

Figure 12 shows a transient plot of the temperature variations during the 5-minute burn test. Chamber wall temperature was seen to increase to about 65 °C within the first 120 seconds,

with a slight increment until the end of the test at 300 seconds. This temperature increment may be attributed to the variation in the water inlet temperature conditions. The use of a closed system in the cooling configuration as seen in Figure 8 allows for water to be recirculated to the combustor. Though the water reservoir capacity exceeded 50 gallons, the coolant's heat absorption was greater than its dissipation to the atmosphere, causing the inlet temperature to increase steadily. The water inlet temperature increased by 2.8 °C over a time of 300 seconds. This change of initial conditions created a limitation in the operation, since the experiment could eventually result in cavitation within the cooling channels and possible failure at the combustor wall. The cooling period of the combustor wall temperature can also be appreciated in Figure 12. It is shown that the combustor requires at least 150 seconds to reach a temperature resembling the initial condition. This period is critical to estimating the time needed to run subsequent tests in the future. The temperature difference between the water inlet and outlet was measured to be 3 °C; this value was used to estimate the heat rejected to the coolant system and its corresponding fraction to the total input.

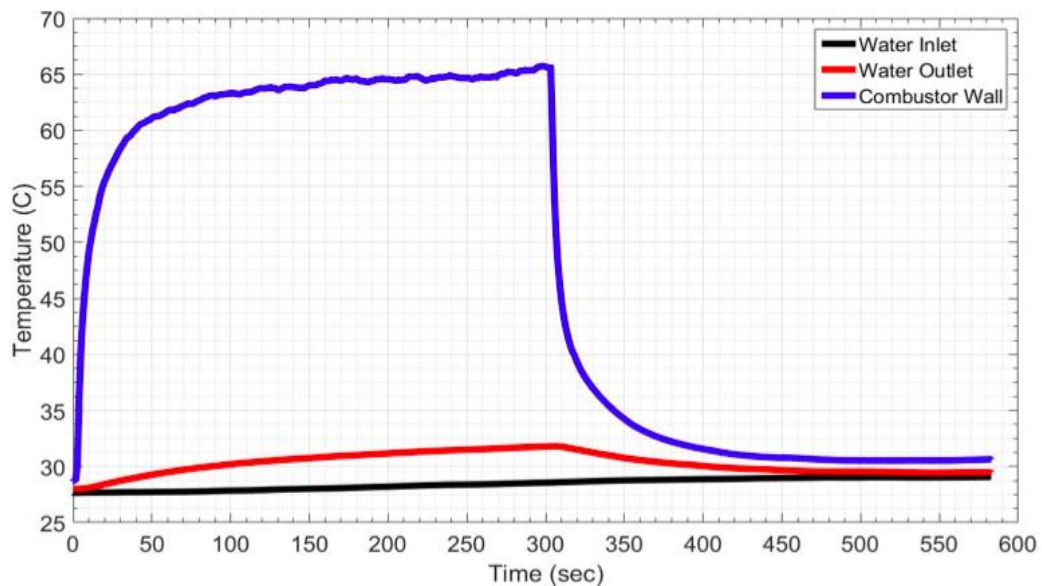


Figure 12: Water and wall temperature variations for 5 minute test

4.2 Numerical Results

4.2.1 Combustion Gas Model-Axial Properties

Figure 13 shows the static temperature contours for the 2-D coupled simulation. Uniform mixing is achieved in the model prior to entering the nozzle, suggesting characteristic chamber length is sufficient to achieve complete combustion. The values of temperature and velocity in the nozzle are compared to equilibrium mixture properties of the combustion product gases obtained through NASA Chemical Equilibrium with Applications (CEA) code [39]. This same methodology has been established in other nozzle characterization efforts found in similar studies [37] [38]. Pressure, temperature and velocity results are presented in Table 5 and compared with results from CEA. Overall, the computational model varies less than 5% compared to CEA. The comparison reveals that the largest difference is in the exit velocity. This is due to the difference in the prediction of product composition between the two models. Downstream of the throat a straight barrel section can be seen in the geometry, implemented for the addition of seeding materials needed to ionize the flow, although the inclusion of seeding particles is not modeled here. In this section temperatures reach 2819 K with a corresponding velocity of 1980 m/s. These values are sufficient for ionizing seeded flow. The lower ionization limit has been shown to be 2300 K [4] [43].

Table 5: Comparison between numerical and analytical methods

Parameter	Symbol	Numerical Model	NASA CEA	Units
Chamber Temperature	T_c	3178	3315	K
Chamber Pressure	P_c	754.9	758	kPa
Exit Temperature	T_e	2759	2873	K
Exit Velocity	V_e	2018	2119	m/s

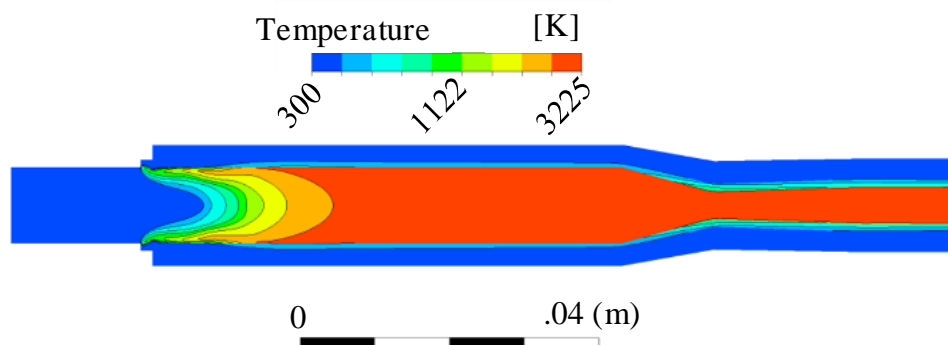


Figure 13: Temperature contours for axisymmetric simulation

Axial properties were estimated through ideal gas flow relationships for pressure, temperature and velocity in the nozzle region. The nozzle area ratios of the MHD device served as the starting points through which local pressures were approximated throughout the converging-diverging region. Pressure estimates were computed using the equations shown below. Equation

30 describes those points in the converging region, while Equation 31 characterizes those of the diverging section.

$$\frac{A_x}{A_t} = \frac{\left[\frac{2}{\gamma+1} \left(\frac{(P_c)_{ns}}{P_x} \right)^{\frac{\gamma-1}{\gamma}} \right]^{\frac{\gamma+1}{2(\gamma-1)}}}{\sqrt{\frac{2}{\gamma-1} \left[\left(\frac{(P_c)_{ns}}{P_x} \right)^{\frac{\gamma-1}{\gamma}} - 1 \right]}} \quad [30]$$

$$\frac{A_x}{A_t} = \frac{\left(\frac{2}{\gamma+1} \right)^{\frac{1}{\gamma-1}} \left(\frac{(P_c)_{ns}}{P_x} \right)^{\frac{1}{\gamma}}}{\sqrt{\frac{\gamma+1}{\gamma-1} \left[1 - \left(\frac{P_x}{(P_c)_{ns}} \right)^{\frac{\gamma-1}{\gamma}} \right]}} \quad [31]$$

Temperature and velocities were estimated through equations 32 and 33. While both relationships are dependent upon localized pressure ratios, velocity is also a function of estimated combustion temperature. These values have been plotted and compared to the computational solution. A comparison of axial velocities to nozzle distance is shown in Figure 14. This distance is measured from the onset of the injector face. The figure shows the computational model results are smaller

when compared to the one-dimensional analysis. A velocity variation of 115 m/s was found at the exit of the nozzle.

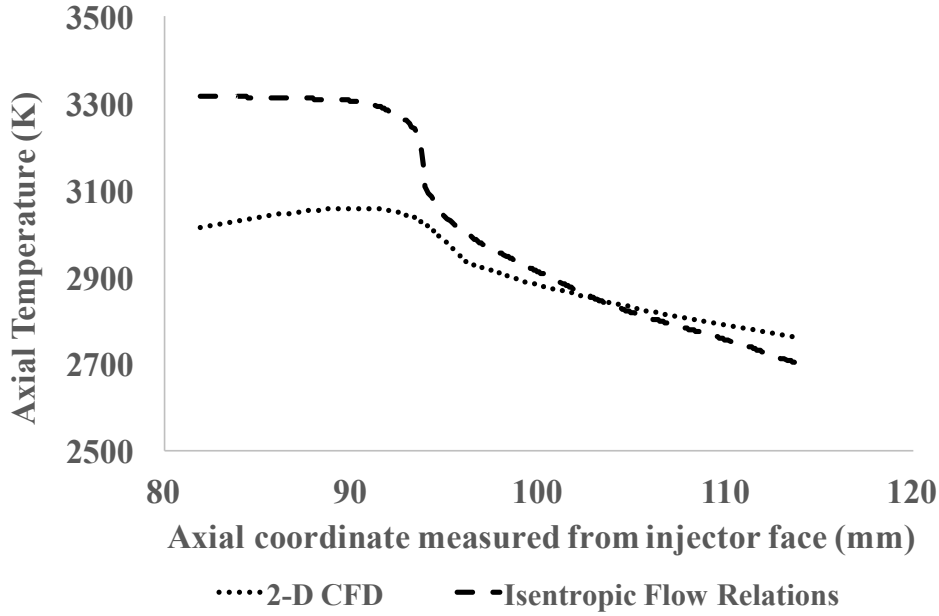


Figure 15 exhibits a comparison of temperatures in the same scale as those of velocity. Like in Figure 14, the computational model results are seen to be smaller than the isentropic values, except at the exit of the nozzle. Though temperatures corresponding to the converging section show significant differences to those of the analytical estimates, a stabilization is seen in the supersonic region.

$$T_x = (T_c)_{ns} \left[\frac{P_x}{(P_c)_{ns}} \right]^{\frac{\gamma-1}{\gamma}} \quad [32]$$

$$v_x = \sqrt{\frac{2g\gamma}{\gamma-1} R(T_c)_{ns} \left[1 - \left(\frac{P_x}{(P_c)_{ns}} \right)^{\frac{\gamma-1}{\gamma}} \right]} \quad [33]$$

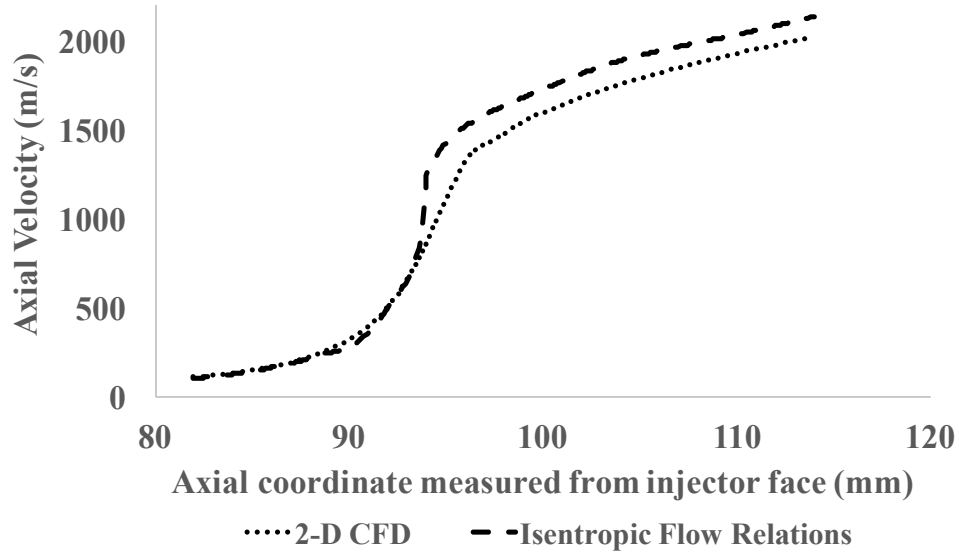


Figure 14: Comparison of nozzle velocity

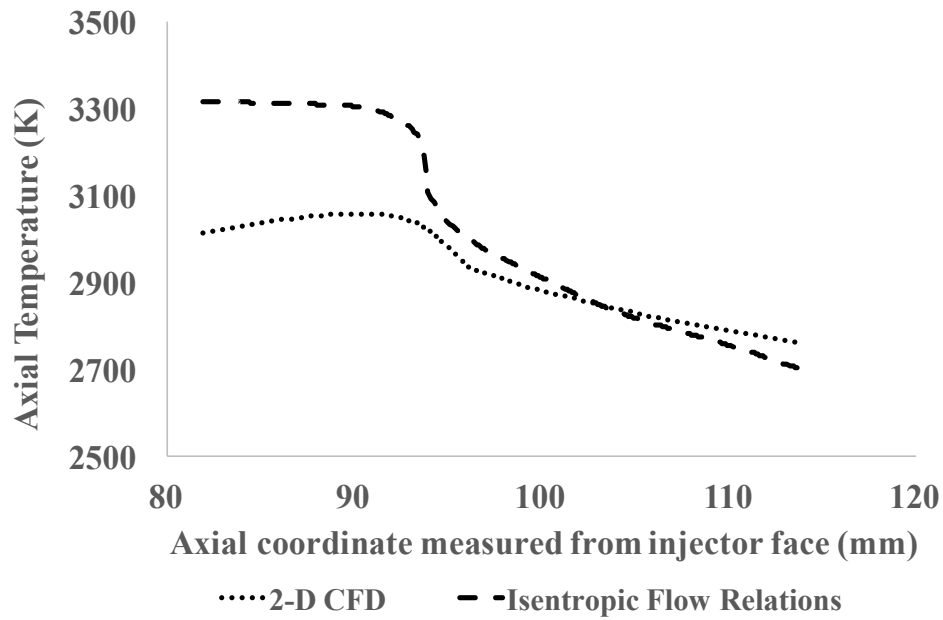


Figure 15: Comparison of axial nozzle temperature

4.2.2 Coupled Heat Transfer Analysis

The analytical heat flux calculated from the Bartz equation is compared to the numerical model in Figure 16. At its maximum point, the numerical model presents a heat flux value 40%

lower than the analytical calculation. This finding agrees with the data presented in a previous study that investigated a methane-cooled rocket that operates at a pressure that nearly doubles that of the current experiment, 1.4 MPa [26].

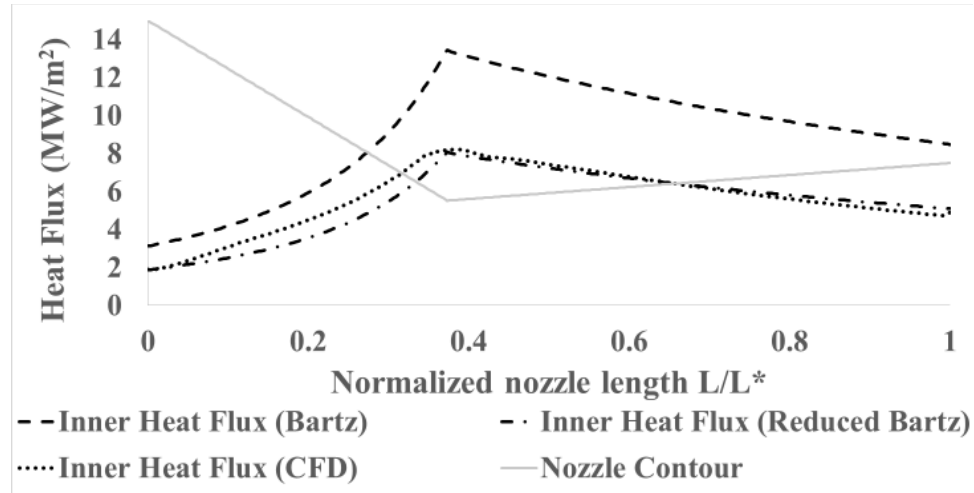


Figure 16: Comparison of heat flux calculation from numerical and analytical model

In a previous study, it has been shown that the inlet conditions of the flow impact the accuracy of Bartz correlation [44]. In particular, findings show that the semi-empirical constant in Eq. [1], 0.026, is highly dependent on boundary layer thickness. This number is suggested as a first approximation when assuming turbulent pipe flow [45]. However, the value of the constant is reported by Bartz to be 0.0225 for a so-called thick boundary layer condition. When comparing the accuracy of the correlation to Back et al. [46] and Kolozsi [47], the maximum experimental values correspond to a 70% and 65% deviation, respectively. Both of these studies employed air at temperatures that varied from 550 to 1100 K and pressures spanning from 207 to 1723 kPa. Back et al. [46] discovered that an increase of boundary layer thickness from 5 to 25% of the inlet radius corresponded to a 10% reduction in the heat transfer coefficient. Similarly, Smith [48] experimentally measured heat flux in a solid propellant motor and found that Bartz correlation over predicted results by approximately 40%.

Additional parameters that have been reported to impact the accuracy of Bartz correlation include the convergent half-angle, contraction area ratio, and chamber pressure. Larger convergent angles have been found to increase the gap between the semi-empirical prediction and test data [49]. In a comparable manner, increasing the contraction area ratio also causes the convective heat transfer to decrease. Welsh and Witte [45] discovered that for a 690 kPa chamber with an 8 to 1 contraction ratio, the maximum heat flux is 60% less than the estimation provided by Bartz correlation. While using a 4 to 1 contraction ratio at the same pressure yields a deviation of 67%. Nevertheless, these investigators also found that at conditions exceeding 1.7 MPa, the same chamber yielded values deviating from Bartz correlation by 99 to 130%. It is evident from these studies that a reduction of the Bartz correlation is required to calculate the heat flux. These studies also reveal that the magnitude of the reduction is highly dependent on chamber pressure. However, for pressures below 1.4MPa most studies show that a 40% reduction of the value calculated with Bartz correlation is applicable independent of propellant or cooling fluid.

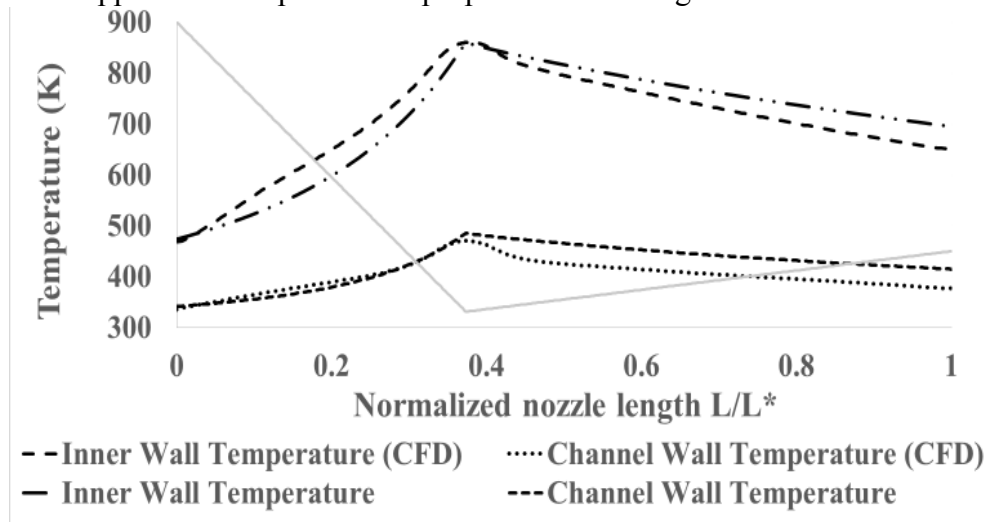


Figure 17: Inner combustor and (outer) channel wall temperatures in the nozzle region

Figure 17 shows the inner and outer combustor wall temperatures in the nozzle region for the present study. Figure 18 exhibits an overall comparison between analytical and numerical results. It can be seen that the analytical heat transfer approximation matches within 4% of the maximum value at both inner and outer walls of the combustor. When comparing

temperature trends in both models, it is apparent that the numerical model predicts a trend of overall higher values in the converging section of the nozzle. Temperature predictions reverse, the numerical method is less than the analytical prediction in the diverging section of the nozzle. At the nozzle entrance, the disparity between numerical and analytical calculations is only 2%, while variations of 7 and 10% are reached at the nozzle exit for the inner and outer combustor walls, respectively.

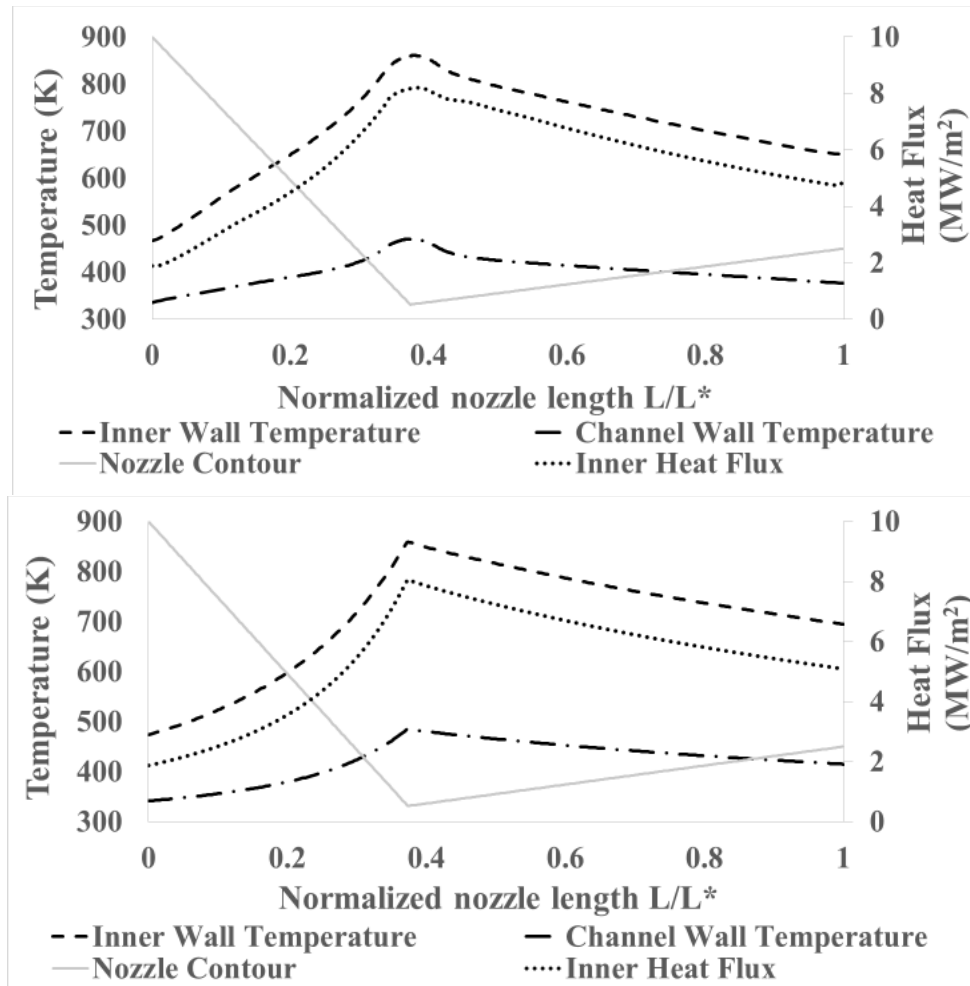


Figure 18: Comparison of nozzle data using (top) numerical and (bottom) analytical model

This behavior may be attributed to thermal stratification effects within the channels due to the counter flow configuration. Although the 1-D analytical model assumes constant thermophysical properties in the coolant fluid, variations in coolant ability to remove heat may

occur if stratification changes the coolant heat transfer coefficient. This value is itself a function of coolant properties, Eq. [4]. Stratification effects within the channels have been shown to be most apparent in the maximum heat flux region in the throat. Stratification is also observed in the chamber region of the cooling channels; this can be appreciated in Figure 19, where the contours of temperature are partially displayed for the cooling channels.

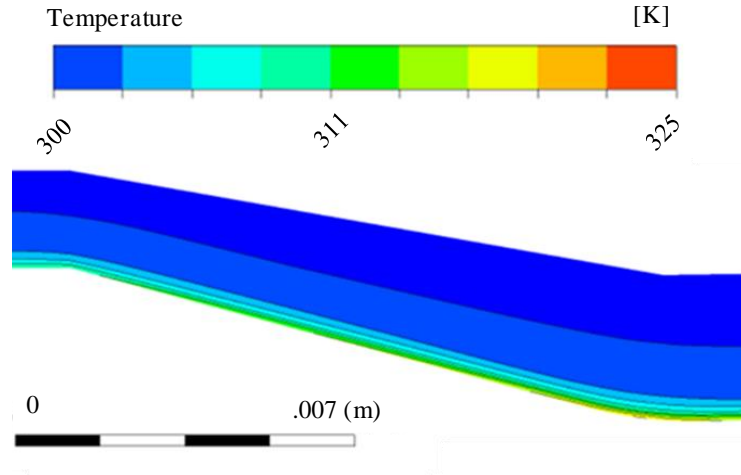


Figure 19: Development of thermal stratification through cooling channels

While previous studies [37] [50] [51] have shown the necessity to account for significant stratification in rocket engines, these investigations reached this conclusion under the assumption of highly compressible gaseous flows and high aspect ratio (HAARC) channels. Since the current system does not use gaseous coolants the effects of stratification are greatly reduced. Thus, the 40% reduction in the Bartz equation and its application as a boundary condition has yielded temperatures that exhibit variations equal to or less than 10% when compared to the computational model.

4.2.3 Comparison to Experimental Results

The computational and analytical models are compared with experimental results in this section. Thermocouples in the coolant line measured temperature during experiments for different run times. In the computational model, temperature and heat flux values have been evaluated and

averaged in a region spanning from 5 mm before and after the location of the thermocouple in the experiment. Computational temperature changes are determined using a mass-weighted average at the water inlet and outlet domains. For the analytical calculation, data are gathered based on the computed inlet nozzle values. An analytical approximation of the total heat removed by the cooling system is done by approximating the product of localized heat flux (Figure 16) and surface area. Experimental measurements of water temperature are used with the energy balance formula $\dot{Q} = \dot{m}c_p\Delta T$ to determine the heat extracted from the combustion chamber. The results and comparison of this analysis are presented in Figure 20.

Figure 20 shows that the 2-D combustor temperature of 346 K is higher than the temperature at the nozzle inlet location, 336 K. Temperature initially drops before steadily increasing in the nozzle region. This change in temperature in this region may suggest the presence of a Dean vortex. Dean vortices appear when centrifugal instabilities are present. The existence of a bend in the flow path results in a change of motion in the fluid direction [52] causing vortices that transform heat transfer behavior [53] and redistribute coolant mass flux [54]. Dean vortices generally enhance coolant heat transfer in both convex and concave bends [54]. The amount of heat transfer enhancement depends on the intensity of stratification in a particular bend [53]. In the case of the bend corresponding to a converging section, the perturbation temporarily enhances heat transfer prior to decreasing in a straight section downstream. In the combustor in this paper, the thermocouple was placed in a straight section located after the converging portion of the combustor. Near the throat, 92 to 96 mm downstream of the injector, a sudden increase in the temperature is observed. The temperature profiles in Figure 17 suggest that the effect of the Dean vortex is overcome by the stratification in the region.

A comparison between analytical and numerical results are presented in Table 6. Both methods predict the combustor chamber heat flux and channel surface temperature within acceptable ranges. The analytical temperature is able to predict surface temperature to within 3 K of the experiments while the computational model predicted a difference of less than 1 kW/m² in the surface heat flux. Analytical calculations overestimate heat transfer coolant temperature by

2.7%. This can be attributed to the assumptions made in the calculation of total heat absorption. For the analytical calculations, it is assumed that heat flux remains constant throughout the chamber to the nozzle inlet, which is an over prediction of heat flux throughout the combustor. In the case of the numerical model, the maximum chamber heat flux is not reached at the 30 mm downstream of the injector location, as seen in Figure 20.

Table 6: Results comparison to experimental measurements

	Numerical Model	Analytical Calculation	Experiment	Units
Coolant Water Temperature Increase	2.02	4.48	3.2	K
Coolant Heat Loss (Q_R)	4.5	9.9	7.1	%
Chamber temperature at x=57 mm	346	341	338	K
Chamber heat flux at x=57 mm	1.65	1.57	1.65	MW/m ²

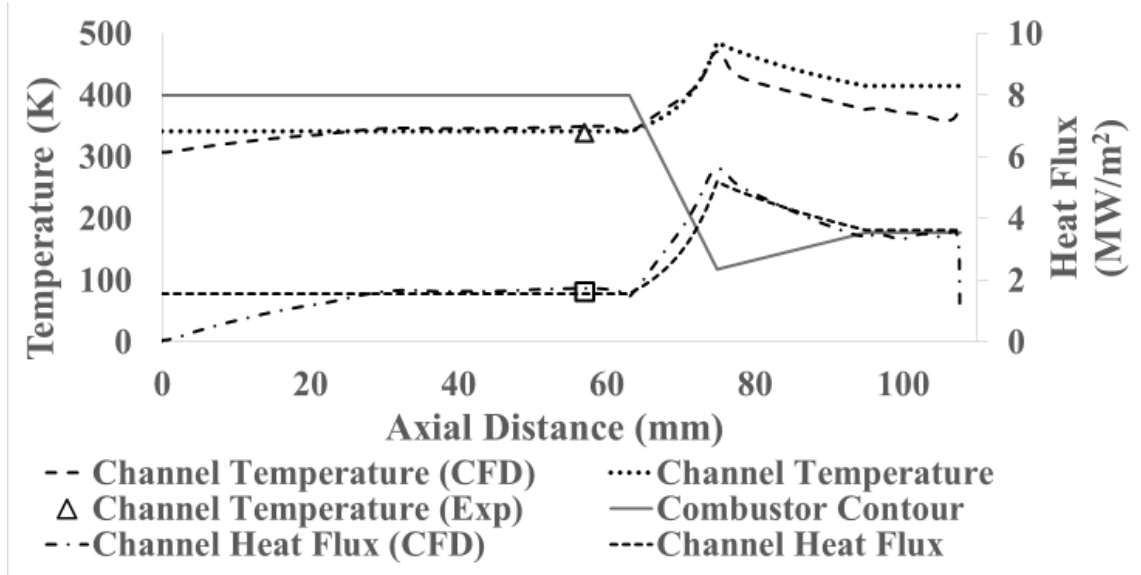


Figure 20: Comparison of numerical and analytical model results to experimental values

A compilation of the analytical, experimental and numerical results presented in the study has yielded similarities between all three methods when the Bartz correlation is reduced by a set value. While the coupled resolution of the pressure and momentum equations enhances accuracy, use of a 1D analytical model coupled with a 40% reduction in the Bartz calculation effectively provides an estimate of maximum throat heat flux. Thus, use of the analytical model for approximation of wall temperatures provide successful estimates of coolant temperature in the chamber and throat regions for chamber pressures below 1.4MPa.

Chapter 5: Design Methodology (1 MW Combustor)

5.1 1MW DPE Combustor Development

An adequate scaling procedure for DPE devices is essential when developing this technology from proof-of-concept to full commercial implementation. In particular, the scale characterization of thermal protection systems is necessary to quantify differences in performance and understand potential risks. While many rocket engine designers focus only upon baseline test parameters, literature suggests that subscale testing may be inadequate when modeling conditions that would exist in a full-scale engine [50]. Reports on MHD literature suggest that there is a research gap in the implementation of open-cycle combustors [4] [55]. A 1978 report from the US Department of Energy suggested that additional research is required to understand larger thermal inputs in MHD systems [55]. Figure 21 shows a layout of historical MHD power generation systems in terms of thermal firing input and total run time. It is seen in the figure that a research gap exists on small-scale designs and large operating times for proof-of-concept models. While the Department of Energy's POC program developed and demonstrated the feasibility of coal-based prototypes with 28 MWth and 50MWth MHD power generators [4], integrated results were not conclusive enough to justify the move to a commercial-prototype retrofit plant in the 300-MWth scale. Coal slag was quoted to pose technological and economical risks, due to its corrosive impact at high temperatures. Additionally, low thermal conductivities were reported due to a poor mixing of the seed and combustion products. Kayukawa [4] reported that higher gas conductivities may be achieved through larger temperatures by oxygen enrichment, but this would entail enhanced stress and an increased oxidation risk. The UTEP MHD prototypes employ near-stoichiometric oxygen and methane; as this mixture condition has not been used in the past, a rational scaling procedure must be performed. The characterization of prototypes at multiple power ratings could lead to the development of non-dimensional scaling parameters suited to similar systems. When combined with rapid prototyping methods, the development of such parameters may lead to reduced production costs and project timelines in the advancement of DPE systems.

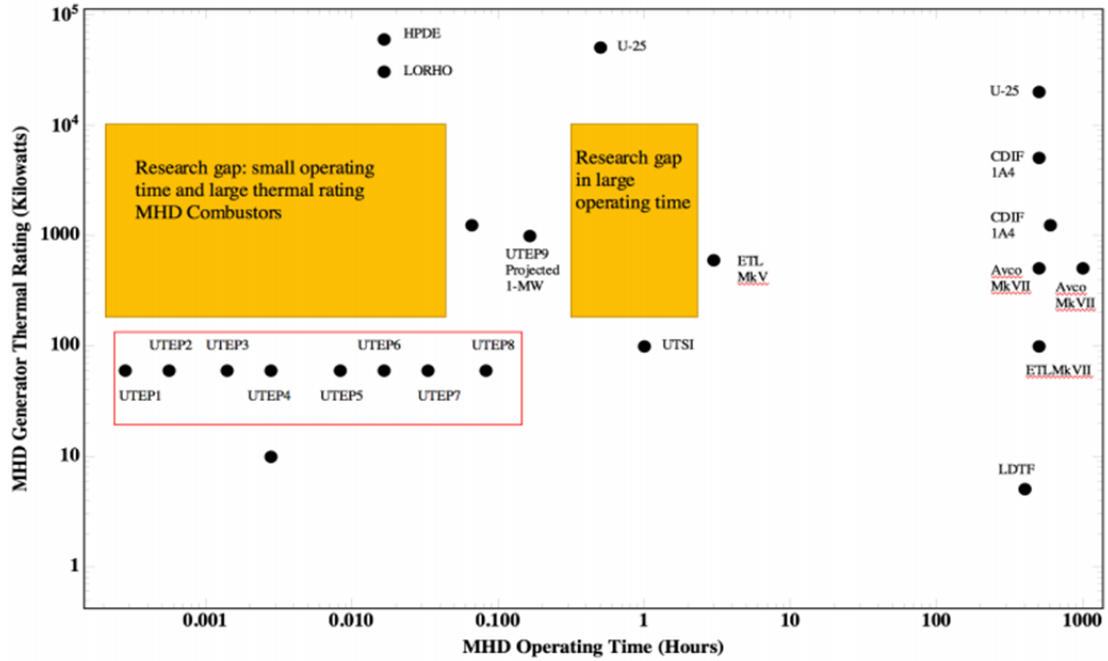


Figure 21: Historical scope of open-cycle MHD studies

5.2 Scaling Procedures

Combustor scaling criteria has been based upon previous studies [15]. A 1979 plan developed by the DoE stated that three phases were required for the full integration of MHD technology in a retrofit plant. The first phase stated that a pilot-scale facility would require a 50 MWth input, with a second phase integrating 250 MWth, and a final, commercial-scale phase demonstrating feasibility at 1000 MWth. These phases imply a scaling factor of 5 and 4, respectively. As the small-scale combustor was tested with power inputs up to 100 kW in rich conditions, a scaling parameter of 10 was employed to determine the power input of the scaled device. At its baseline (60 MWth) operating condition, this scaling parameter corresponds to 16.7. In accordance to the DoE projection, to reach a pilot-scale facility, this combustor would have to face two further scaling iterations. Due to its reliable operation, parameters involved in the design of the 60-kW combustor have been set as a reference point for the development of the 1-MWth

prototype. A gas exit temperature of 2800 K and exit velocity of 2000 m/s were set as baseline minimum nozzle parameters.

Combustion similarity of different-size chambers is a demanding requirement [56]. The scaling criteria of a combustor is said to be acceptable if similarities between injector and chamber geometries are maintained, along with propellant configuration and injection velocities [56]. A complete scaling of a combustion chamber would imply all combustion processes occur in a similar manner [56]. Though a set of similarity parameters for internal aerothermochemistry in Liquid Propellant Rocket Engines was developed by Penner [56] in the 1950s, the proposed criteria have been found to have opposable parameters. In addition to this, the number of processes occurring in rocket engine combustors is very large, making complete flow similarity unfeasible [56]. An extended evaluation of the interaction of individual processes in scaling criteria would carry elevated costs [56]. As such, only certain parameters can be prioritized when developing scaled combustor models. A number of parameters employed in the initial design are thought to be viable in the development of the scaled combustor. Scaling parameters have been determined from critical design criteria found in rocket literature [32]. These parameters include the characteristic chamber length L^* , nozzle convergence ratio, nozzle divergence ratio and injector momentum flux ratio (MFR). The combustion reaction is kept constant by maintaining the oxidizer and fuel combination at the same theoretical chamber pressure and equivalence ratio. The minimum mass flow rate was determined through Eq. 34, which relates the higher heating value of methane to the required power input.

$$\dot{m} * HHV = PW \quad [34]$$

Required mass flow rate was found to be 18 times greater than the proof-of concept model according to this relationship. A determination of the throat area A_t was performed through Eq. 35, corresponding to the methods employed by Huzel and Huang [32].

$$\dot{m} = A_t(p_c)_{ns} \sqrt{\frac{g\gamma \left[\frac{2}{\gamma+1}\right]^{\frac{\gamma+1}{\gamma-1}}}{R(T_c)_{ns}}} \quad [35]$$

The 60-kW combustor utilized a swirl coaxial injector configurations, with 4 tangential ports to achieve the desired mixing characteristics. When operating at a chamber pressure of 670 kPa (110 psi), the equilibrium conditions resulted in a momentum flux ratio (MFR) of 16. While injection parameters have a significant impact upon combustion scaling of liquid-fueled rocket engines [57], gas-gas combustion is a simplified process that involves only the mixing and reaction of the components. In this design, injector geometry scaling has followed the photo-scaled method, implying injector dimensions are varied in proportion to chamber length scales. Using this method, the Reynolds number must change between scales to maintain a constant chamber pressure. The use of the photo-scaling method is suggested by previous empirical data on combustion stability [56]. Combustor stability may be further improved by an increase in injector pressure drop. Increasing pressure drop dampens potential oscillations in the flow and helps to stabilize upstream pressure and velocity conditions. The injector design in this model is based on the required pressure drop range stated by Huzel and Huang [32]. A 20% pressure drop in the system was assumed for the calculations. The number of tangential ports and swirl-coaxial configuration have been maintained in the scaled combustor. A non-dimensional number (MFR) has been selected as a constant parameter to ensure similarity between injectors. This parameter is outlined in Eq. 36.

$$MFR = \frac{\rho_f v_f^2}{\rho_{ox} v_{ox}^2} \quad [36]$$

Injector cross-sectional areas were adjusted to maintain the pressure drop requirements in the system. This resulted in increased overall injection velocities. The calculated oxidizer orifice diameter resulted in a value ~50% smaller than that of the combustion chamber. A transition region employing a 5th order polynomial [59] was implemented to expand this area, turning the flow to develop a uniform velocity profile. Heat transfer characteristics of the model were evaluated in accordance to the methods described in Section 2.2. A maximum heat flux of 7.14 MW/m² was found at the nozzle throat, with the assumption of a reduced Bartz correlation and a desired wall temperature of 575 °C. The heat flux value was employed to evaluate proposed combustor wall thicknesses in accordance to Eq. 3. The final design's wall thickness equaled that of the small-scale configuration. A finite element analysis model of the combustor revealed that the 1-mm configuration results in an overall safety factor of 1.7, assuming the material's high-temperature yield strength to be 960 MPa [60].

According to Xiao et al [57], hot-testing data from a low-pressure gas-gas configuration may be extended to a high-pressure full scale chamber. As such, proof-of-design concepts are said to provide invaluable data when scaling, decreasing overall costs and identifying potential dangers. As the wall thickness and overall heat flux parameters mimic those of the small-scale model, cooling velocity requirements were found to be comparable in the 1-MW combustor. The small-scale cooling system employed six 2-mm channels throughout its geometry. To maintain fin base thickness, the 1-MW combustor was designed to use 20 channels with the same cross-sectional geometry. A comparison of channel configurations through analytical methods (Section 6.3) revealed that the standard 2mm x 2 mm channel geometry will result in minimized temperatures and lower temperature gradients. Coolant manifold configurations have been optimized according to the methods described in Section 6.1. A 4-water inlet, 25-mm manifold configuration was

deemed as distributing coolant flow most evenly among the cases compared. These geometrical parameters can be appreciated in Figure 22, displaying an exploded view of the elements employed in combustor development.

Figure 23 displays the principal dimensions of the finalized 1-MW combustor model, while Table 7 shows a summary and comparison of both combustor's final design parameters. The scaled model's combustion chamber configuration centers around parameters determined to focus upon geometrical similarities. Chamber contraction ratio was not varied significantly, as it affects the mixing level in developing combustion and determines the Mach number in the chamber. The expansion ratio and divergence angle were kept constant to conserve a high momentum efficiency and achieve the required exit gas velocity [60]. The length of the chamber is said to affect the overall mixing efficiency of the propellants [56], with relatively large injection elements showing a mixing improvement with increased L^* . A higher number of smaller elements, such as those found in showerhead patterns, have been shown to have little improvement through this process. The characteristic length of the combustion chamber was increased with the inclusion of the transition region. A numerical simulation of the combustion flow-fields revealed that the inclusion of this region yielded an even mixing throughout the combustion chamber [60].

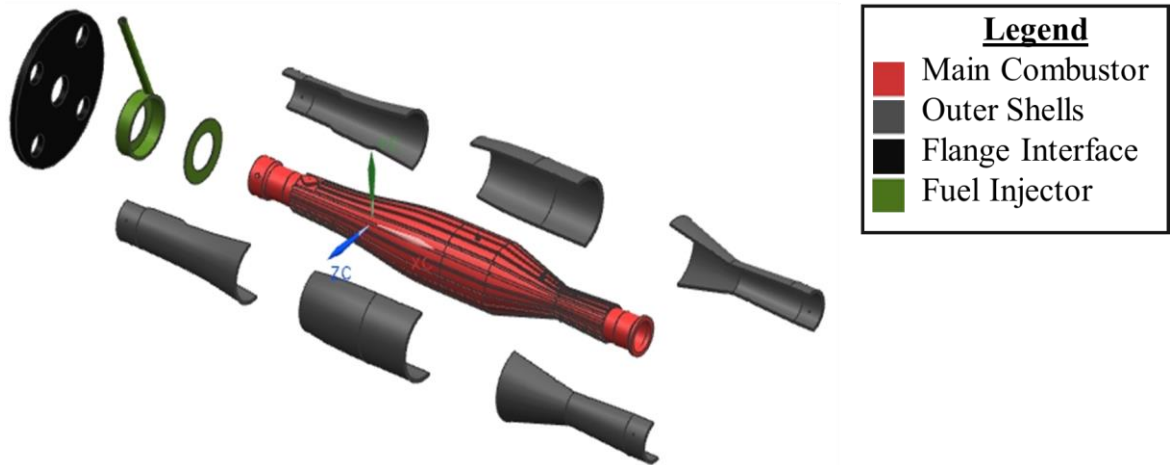


Figure 22: Exploded view of main combustor components

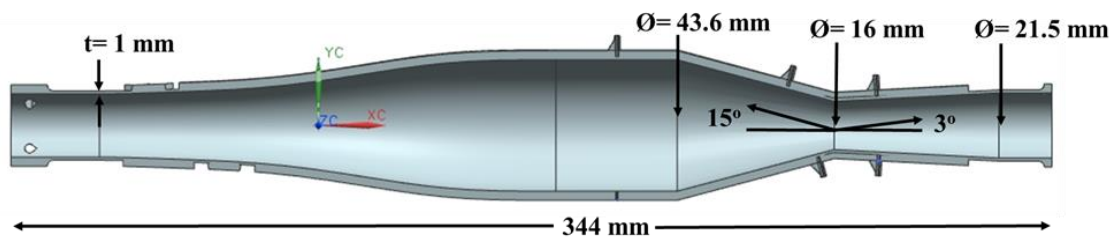


Figure 23: Principal dimensions of 1-MW design

Table 7: Comparisons of design criteria

	Units	Proof-of-concept	Scaled Prototype
Design Criteria			
Baseline Power Rating	kW	60	1000
Combustor Material	--	Inconel 718	
O2 Mass Flow	g/s	3.6	64.8
CH4 Mass Flow	g/s	1	18
Equivalence Ratio	--	1.1	
Exit Gas Velocity	m/s	2000	
Exit Gas Temperature	K	2800	
Combustion Chamber			
Characteristic Length (L*)	m	0.62	1.44
Chamber wall thickness	m	0.001	
Chamber Pressure	KPa (psi)	760 (110)	
Nozzle			
Throat Diameter	m	0.0036	0.016
Contraction Ratio	--	7.4	
Expansion Ratio	--	1.8	
Converging Angle	--	15°	
Diverging Angle	--	2°	
Injector			
Number of injector ports	--	4	
Momentum flux ratio	--	16	
Fuel pressure drop	Kpa (psi)	138 (20)	
Orifice Size	m	0.0016	0.0028

5.3 Additive manufacturing & final design

The 1-MW MHD combustor prototype was manufactured through the use of a Selective Laser Melting (SLM) technique. The inclusion of additive manufacturing technology allowed for a greater design freedom, reduced lead time, and reduced cost. The SLM method has been quoted as suitable for producing metal parts including complex geometries, such as those that include integrated cooling conduits [56] [57]. SLM generates dense metal parts through the fusion and consolidation of a powder bed in a layer-by-layer manner through a high-energy laser source [56]. The rapid heating and cooling involved in this method offers the potential for the development of fine-grained structures with superior metallurgical properties. The use of additive manufacturing methods in the aerospace industry has gained popularity in recent years. In 2012, SpaceX successfully tested a full-scale rocket engine (SuperDraco). This regenerative cooled engine was manufactured through the use of direct metal laser sintering (DMLS) [56]. NASA is currently researching additive methods to create complex components. Marshall Space Flight center has fabricated both injector (NASA) and nozzle [56] Inconel configurations through the SLM method. High-temperature tests have successfully been performed on the Inconel 625 nozzle with temperatures reaching 3315 °C [56], similar to those seen in the UTEP MHD configuration. The lab-scale nozzle prototype employs water as a cooling system. This nozzle has been tested for a total burn time of 130 seconds, was reported to perform as expected with no evident visual degradation [56]. While additive manufacturing (AM) methods are gaining acceptance in the field, an obstacle for their full integration relates to the fact that non-destructive testing techniques are still emerging. The cost and time to develop these methods has been quoted to be of concern, as AM technologies are rapidly changing [56]. Inconel 718 has been called an ideal candidate for SLM due to its low content of aluminum and titanium [56]. This material is also difficult to manufacture conventionally due to its hardness and wear on tools [56]. A 2016 study by Trosch et al. [57] revealed that Inconel 718 parts manufactured by SLM present slightly higher ultimate tensile strength and lower elongations (NTP) in comparison to forged samples. In general, build direction was shown to have a large impact, as horizontal-built SLM specimens were found to

have a higher UTS than vertical-built samples. An evaluation of high-temperature properties revealed that while SLM—parts are initially similar to their forged counterparts, their properties begin to decay after 450 °C, falling within the range of forged samples [56]; these properties could be further improved by continuous optimization of the microstructure [56]. The results of this study are summarized in Figure 24. Combined stress considerations of future MHD designs must account for these property variations in the form of a safety factor. Though temperature regions exceeding 450 °C are relatively small when compared to the overall combustor dimensions, SLM-manufactured parts have been shown to lose ductility at higher rates [56]. This may result in an elevated deformation risk at the nozzle throat. As geometrical nozzle properties are a significant consideration, further studies must be performed on the high-stress regions of MHD combustor designs.

UTS ^a (MPa) R _{p0.2} ^b (MPa) e _f ^c (%)	Horizontal	Vertical	45°	SLM (average)	Forged	Cast
Room temperature	1440 1186 18.5	1400 1180 20.4	1450 1190 16.9	1430 1185 18.6	1380 1192 19.1	950 940 23.1
450 °C	1216 1033 12.4	1160 1026 15.9	1255 1080 12.8	1210 1046 13.7	1177 1055 17.0	766 750 10.9
650 °C	1011 870 3.6	992 860 14.2	1074 855 5.8	1026 862 7.9	1061 955 13.9	576 517 13.7

Note: Each value was determined from an average of 4 measurements.

^a Ultimate tensile strength.

^b 0.2% yield strength.

^c Elongation to failure.

Figure 24: Mechanical properties of Inconel 718 as reported by Trosch et al. [56]

Figure 25 shows a contrast between the CAD model and the combustor manufactured through SLM. This figure shows a comparison of the size and location of features critical to the design. Two 1/4” spark plugs (D) were integrated into the 1-MW geometry. As mixing length parameters between both gases were not characterized, a decision was made to include the ignition sources at locations 40 and 65 mm away from the point of fuel injection. A static pressure sensor

(E) and thermocouple conduits (F) have been included in the chamber design to assess combustor characteristics and ensure safe operating conditions. Thermocouple conduits were designed to measure temperature within the fins at a wall thickness of 1 mm, matching that of the cooling channels. The pressure conduit (E) has been modeled to operate in the same manner as the one employed in the small-scale geometry. As quenching distance in a $\text{CH}_4\text{-O}_2$ mixture has not been extensively investigated in literature, an inner diameter of 0.5 mm was implemented to prevent failure in the conduit.

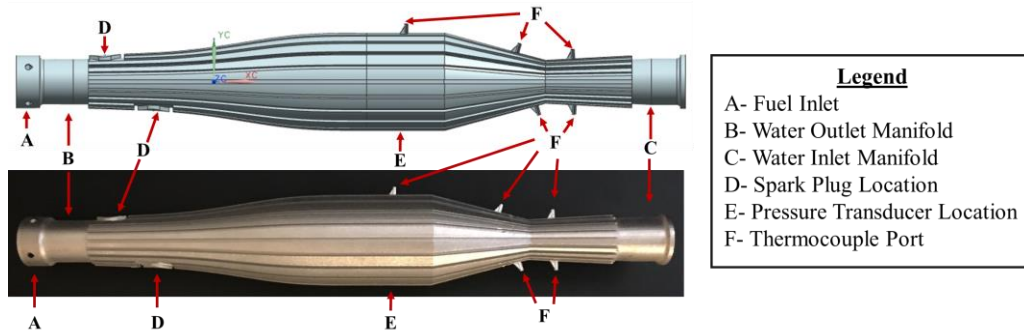


Figure 25: Comparison between CAD and AM models

Figure 26 provides detailed view of the combustor's geometrical features. Though the combustor has been cleaned and post-processed, the part retains a relatively rough surface. A high surface roughness may provide a beneficial effect if a portion of the combustor walls reaches the nucleate boiling regime, with heat flux increasing by up to a factor of 10 [68]. Nevertheless, this beneficial effect dissipates if the surface approaches film boiling.



Figure 26: Detailed views of the 1-MW combustor

Figure 27 displays detailed views of the combustor's thermocouple ports in the nozzle region. These features have been carefully assessed, as surface temperature readings are considered an integral part of the combustor design. Both thermocouple and injector inlet ports were designed with a 'teardrop' shape to account for build orientation. Circular features are notorious for experiencing dimensional inaccuracies (shrinkage) in vertical builds. As shown in Figure 27, the teardrop shape in the thermocouple ports has been maintained with minimal change in shape. The ports were shown to have an adequate inner diameter to that of the probe thermocouples, as the sensors were shown to fit in a suitable manner.

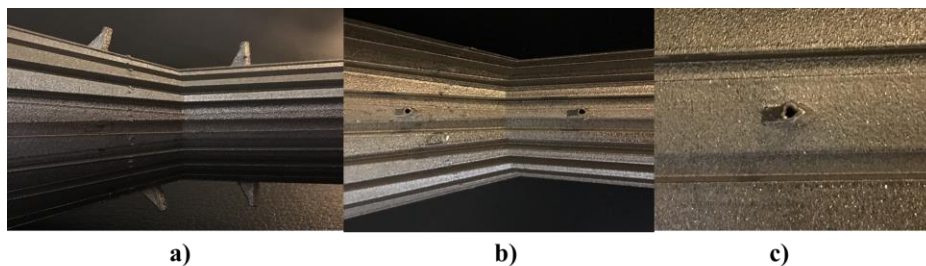


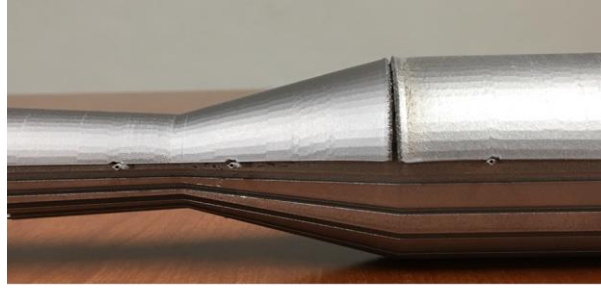
Figure 27: Thermocouple port views a) side b) top c) detail

The manufacturing lead time on the main combustor was three weeks. The actual part build time was reported to be less than three days. As a comparison, the total manufacturing time of the POC combustor using traditional manufacturing was 12 weeks. Though all parts were developed using the SLM method, the main combustor's manufacturing was outsourced to an external facility. The outer shells were developed in-house at UTEP's W.M. Keck Center. Due to machine sizing constraints, the shells were segmented in three sections, to be later assembled and welded. Figure 28 displays the cooling jacket outer shells, while Figure 29 displays a partial assembly of these components. The effect of machine processing parameters is seen in the slight radial warping observed in the shell sections, as this effect was not observed in the main combustor portion. A study by Wang et. al [56] showed that warping defects occur due to the high thermal stresses developed in the rapid solidification of the melt pool. Plastic deformation occurs when these stresses exceed the material's strength. Laser energy input has been shown to play a large role on

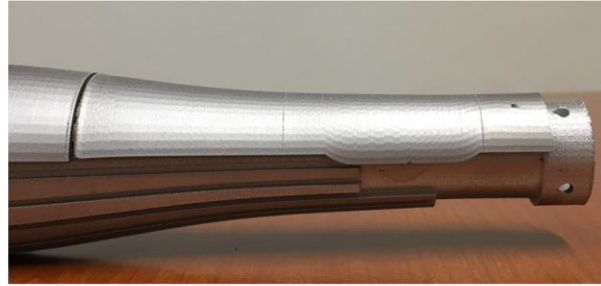
the degree of warping: when this energy is too large the layer is melted too deep, increasing the amount of molten metal and increasing overall solidification time [56]. The microstructures of SLM-manufactured parts are affected by the non-equilibrium processing laser techniques [57]. As such, optimizing process parameters can lead to improved microstructures. At the moment, efforts to determine their effect on the properties of these structures are still ongoing [57]. While a warping effect typically occurs in overhanging surfaces, relatively large residual stresses can occur at the bottom of the parts. Though axial warping is not visually significant, an accumulation of material is apparent from the bottom portion of the parts, affecting the total assembly of the components and the alignment of the shells with sensor ports (Figure 29). Further post processing is required to shorten these portions prior to welding the structure.



Figure 28: Outer shells manufactured by SLM



a)



b)

Figure 29: Partial assembly view of a) nozzle and b) inlet components

An evaluation of dimensional accuracy (Tables 8 & 9) was performed on the main combustor and shell portions to quantify the accuracy of the SLM method and verify the safety of the parts. A significant increment in the combustor's wall thicknesses may result in increased thermal stresses, leading to a higher failure probability. Figures 30 and 31 display schematics of the measured dimensions, while Tables 8 and 9 show the study's results. All measurements were taken three times with a standard dial caliper to quantify the random error in the measurement. The exception of this is the overall combustor length dimension, as this was measured with a ruler. The use of this device resulted in a large random error. Overall, the main combustor's dimensions displayed differences in measurement to the CAD of less than 6%. This is relevant specifically when quantifying features larger than 2 mm, as a different measurement tool is necessary for accurate estimates of smaller features. A significant variance was observed in the measurement of the thermocouple ports due to the size of the measuring device. When comparing the results of the combustor to those of the outer shells, it is apparent that the combustor shells display much larger differences with the CAD model. Overall sizing differences were also observed between

symmetrical shells. Inaccuracies in the radial portion were found to be more significant than those in the axial direction. Though the inaccuracies in shell sizing are significant they do not prove to be critical, as temperatures are not expected to rise significantly in this portion. Combustor parameters D, E, F and G, showed measurement variations of less than 4%. The accuracy of these features has been deemed adequate in regards to the overall expected gas characteristics.

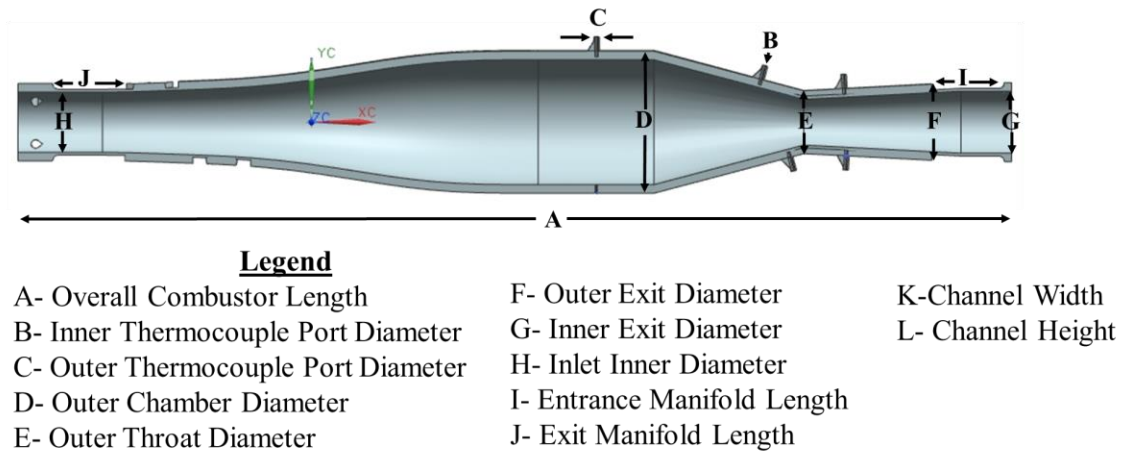


Figure 30: Schematic of measured dimensions

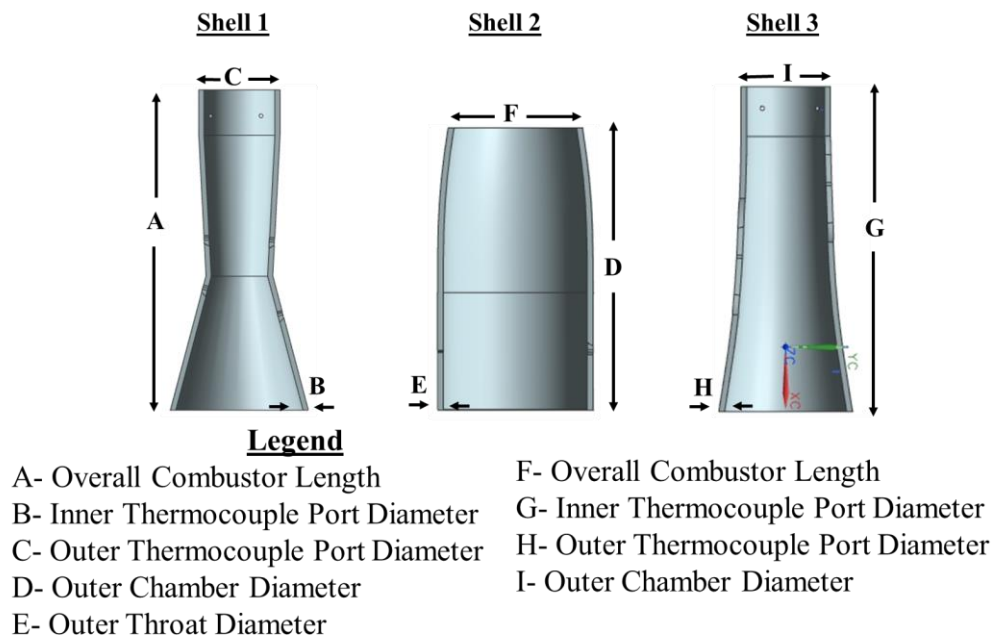


Figure 31: Schematic of measured dimensions (shells)

Table 8: Dimensional analysis results on 1-MW combustor built by AM methods

	Average Measured Value (mm)	Actual Value (mm)	% Difference	Random Error
A	347.8	343.8	1.2%	24.4%
B	0.7	0.8	11.6%	0.2%
C	1.5	1.4	10.7%	1.3%
D	49.4	49.9	1.0%	0.6%
E	21.9	21.2	3.8%	0.7%
F	26.5	26.7	1.0%	1.3%
G	21.2	21.8	2.7%	1.7%
H	20.7	21.2	2.1%	1.3%
I	25.0	25.0	0.0%	2.0%
J	25.1	25.0	0.2%	0.5%
K	1.9	2.0	5.2%	0.1%
L	1.9	2.0	5.6%	1.3%

Table 9: Dimensional Analysis Results for Cooling Shells

	Shell 1				Shell 2				Comparison
	Avg. Meas. (mm)	Actual Value (mm)	% Diff.	Random Error	Avg. Meas. (mm)	Actual Value (mm)	% Diff.	Random Error	Shell % Diff.
A	124.8	123.5	1.0%	0.1%	124.7	123.5	1.0%	0.1%	.1%
B	2.0	2.0	2.0%	0.1%	2.2	2.0	7.5%	0.9%	5.4%
C	31.7	46.6	32.1%	0.4%	31.8	46.6	32%	1.2%	.6%
D	97.4	96.5	0.9%	0.8%	97.3	96.5	0.8%	0.6%	.2%
E	2.2	2.0	7.5%	1.7%	2.2	2.0	11%	0.5%	2.8%
F	47.1	31.8	48.1%	1.4%	47.0	31.8	48%	0.7%	.2%
G	112.7	111.8	0.8%	0.4%	112.7	111.8	0.8%	0.3%	0%
H	2.1	2.0	4.1%	0.9%	2.0	2.0	2.0%	0.4%	2%
I	31.0	31.2	0.3%	0.4%	31.1	31.2	0.2%	0.5%	.1%

Chapter 6: Optimization of Cooling System

A thorough thermal analysis of the cooling system is necessary to ensure the steady-state combustor operating parameters for the 1-MW geometry. Literature has stated that a detailed analysis is particularly important in reusable engines to extend engine life, or where coolant warming provides power in turbo-machinery [51]. Numerical methods allow for the comparison of channel and fin geometries with similar theoretical performances. The use of a numerical approach is especially crucial in medium and large-scale engines, where the channel heat absorption and coolant properties differ significantly from proof of concept models. These results may be employed in the future to provide optimum local channel geometries in similar configurations, eliminating the issue of over-cooling and reducing the overall heat loss to the cooling system. In this investigation, a combination of numerical and analytical methods are employed to investigate proposed channel configurations for the large-scale MHD combustor. Parametric studies regarding the manifold and individual cooling channel configurations are presented in the following sections.

6.1 Manifold Optimization

Investigating the entering portion of the cooling configuration is necessary to understand and enhance channel distribution in large-scale configurations. As the water enters the system in a relatively high-heat flux region of the combustor, an equilibrium must be achieved between rapidly cooling this geometry and evenly distributing the coolant among all channels. A manifold configuration is required to allow the entering fluid to mix and dispense the flow. A parametric study has been performed in an attempt to optimize those parameters critical to the long-term operation of the model. This numerical study compares the entering manifold length, diameter of incoming water pipes and the number of coolant inlets in the system.

6.1.1 Numerical Domain and Setup

The generalized domain for this simulation is shown in Figure 32. A periodic interface was implemented to simulate half of the manifold. This configuration increases the number of elements in the region and improves the accuracy of the simulation. In addition to this, the channel domain has been simulated only to the throat region of the nozzle. At this portion, flow has been deemed to be developed enough to analyze centerline velocity and mass flow distribution.

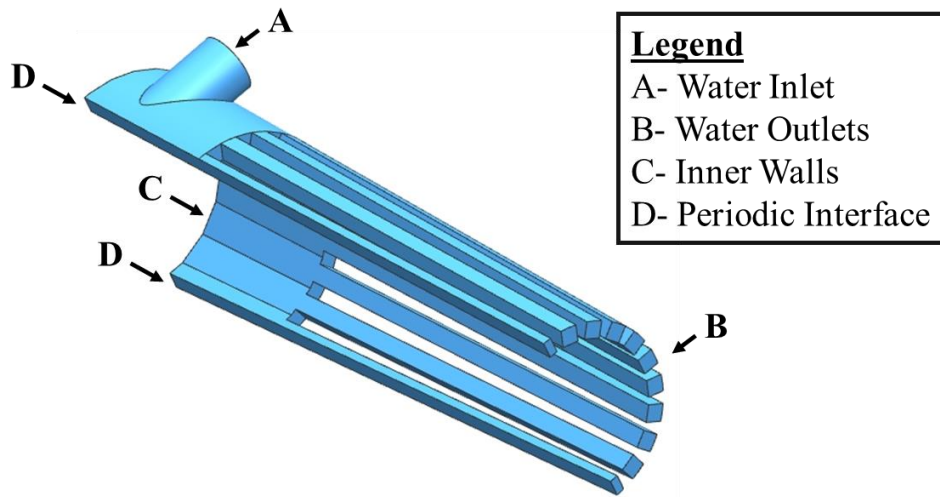


Figure 32: Domain for manifold simulation

Table 10 shows the cases employed in this study. Inlet diameters of 7 and 10 mm were compared; these correspond to the inner diameters of commercially-available pipes of $\frac{1}{4}$ " and $\frac{3}{8}$ ". The number of these inlets is varied from 2 to 4 to investigate the effect of entering tangential velocities. Finally, the length of the mixing manifold is investigated on the effect of channel mass flow distribution.

Table 10: Cases Employed in Manifold Simulation

Case	Inlet Diameter	Number of Inlets	Manifold Length (mm)
A	7	2	20
B	10	2	20
C	7	4	20
D	10	4	20
E	7	2	25
F	10	2	25
G	7	4	25

A detailed view of the employed mesh (Case A) is seen in Figure 33. An unstructured tetrahedral mesh was employed due to the high curvature of the configuration. A minimum orthogonal quality of .4 was found in all meshes. Face sizes were set to have side lengths of $4\text{E-}4$ m in all configurations, with the meshes designed to have a minimum number of elements of 400,000. It was desired to maximize the number of elements in this region due to the chosen tetrahedral configuration, as these type of elements occupy less space than hexahedrons.

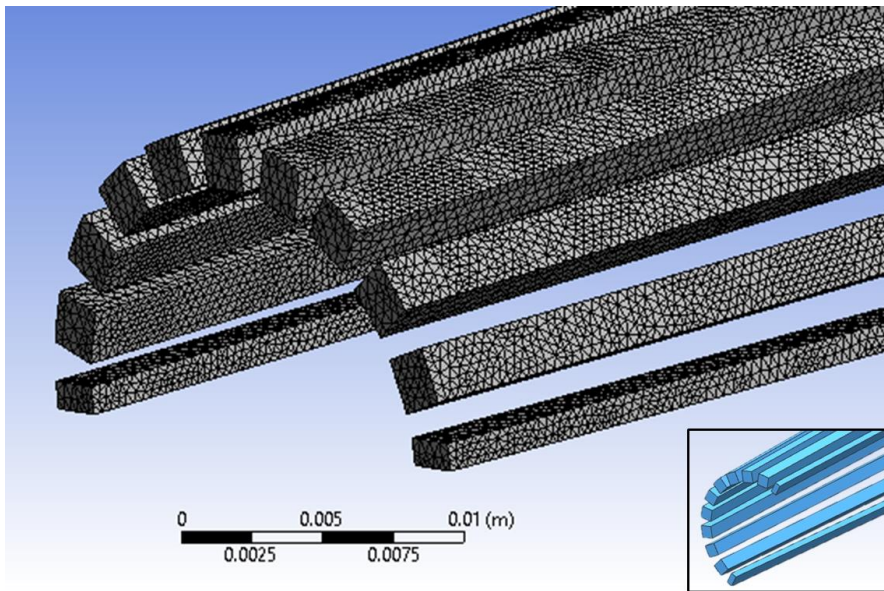


Figure 33: Manifold simulation mesh detail

Equations relevant to the modeling of the configuration have been described in section 3.1. Mass and momentum equations correspond to equations 8-11, while the transport equations relevant to the realizable k-e model correspond to 12 and 13. As this model does not involve non-premixed combustion, the total form of the energy equation is employed. This is shown in the relationship below, Equation 37.

$$\frac{\delta}{\delta t}(\rho E) + \nabla \cdot (\vec{v}(\rho E + p)) = \nabla \cdot (k_{eff} \nabla T - \sum h_j \vec{J}_j + (\overline{\tau_{eff}}) \cdot \vec{v}) + S_h \quad [37]$$

The boundary conditions employed in this model are summarized in Table 11. In regards to the fluid material, water properties were customized by curve-fitting the relevant parameters according to the predicted temperature range. A summary of these properties is shown in Appendix E. The inner wall boundary condition has been defined by a user defined function shown in Figure 34. This estimate of heat flux has been generated by the temperatures predicted by Equation 6. To simplify the simulation and achieve adequate convergence parameters, the fin effect and solid domain have been neglected. A pseudo-transient scheme was employed with the coupled solution

method to accelerate the convergence of the simulation. All cases were deemed to have converged when the unscaled continuity residual reached a value of $1\text{E-}4$.

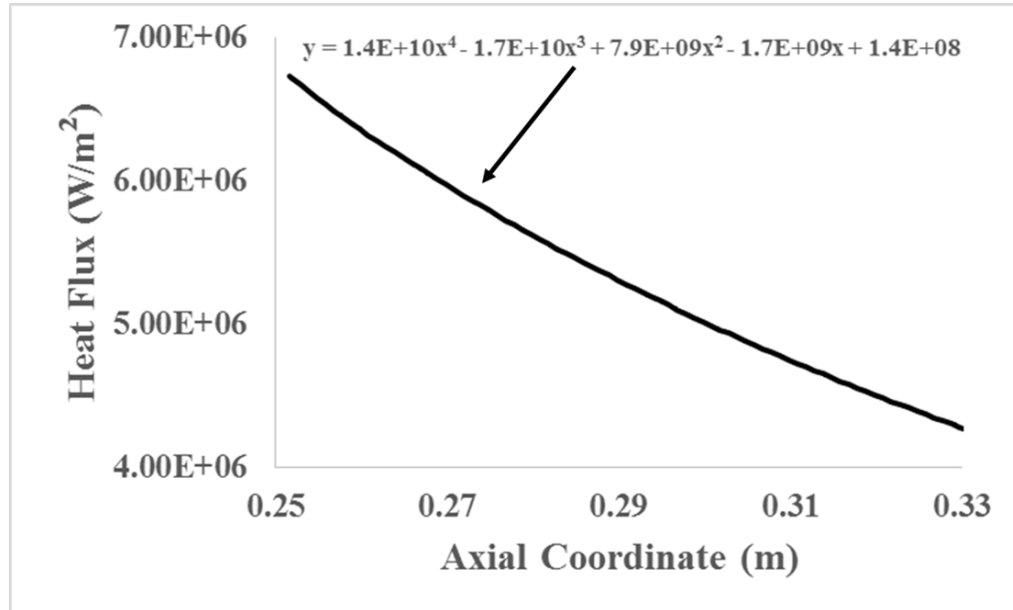


Figure 34: Inner wall boundary condition, UDF

Table 11: Boundary Conditions employed in manifold simulation

	Input
Models	<ul style="list-style-type: none"> • Energy-ON • Viscous-Realizable k-epsilon, Scalable Wall Function
Materials	<p>Water- Liquid</p> <ul style="list-style-type: none"> • Density- user defined polynomial • C_p- user defined polynomial • Thermal conductivity- user defined polynomial • Viscosity- user defined polynomial
Boundary Conditions	<p>Inner Walls</p> <ul style="list-style-type: none"> • Wall- Heat Flux • Heat Flux- UDF <p>Water Inlet</p> <ul style="list-style-type: none"> • Mass flow inlet- .31384 kg/s (base) • Turbulent Intensity- 3.5% • Hydraulic Diameter- 7 or 10 mm <p>Water Outlets</p> <ul style="list-style-type: none"> • Pressure Outlet • Turbulent Intensity- 3.5% • Hydraulic Diameter- 7 or 10 mm <p>Periodic Interface</p>

Solution Methods	Initialization- Water Inlet Scheme- Coupled (Pseudo-Transient) Pressure- Second Order Momentum- Second Order TKE- First Order Epsilon- First Order Energy- Second Order
------------------	---

6.1.2 Numerical Results

Figure 35 displays the temperature contours of base model A, of two 7-mm tangential inlets. This contour includes the periodic repeat domain to showcase the mirroring of the geometry. It is seen from the figure that a maximum temperature region is concentrated in an area of low velocity, where inlet flows intersect each other. This trend has been seen to continue throughout the remaining simulations and is analyzed below.

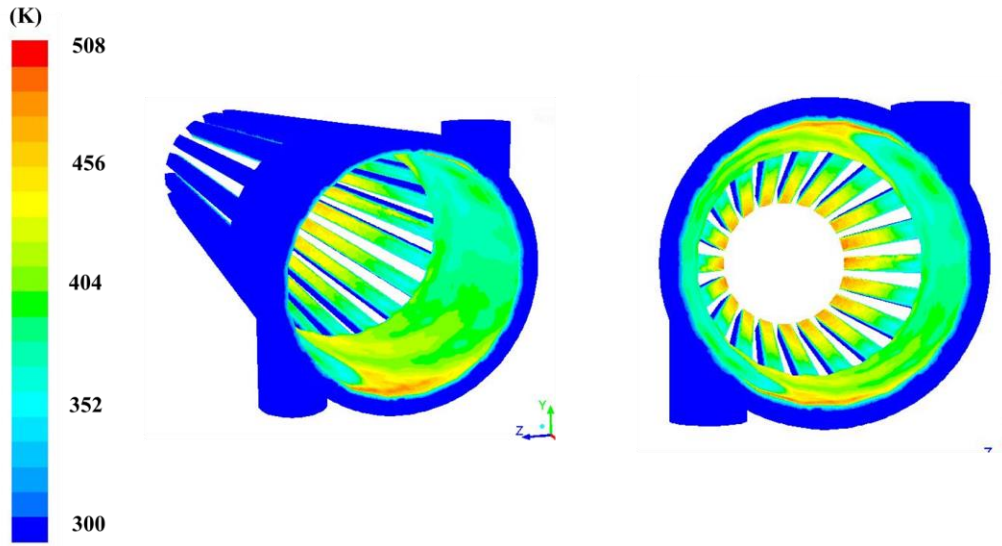


Figure 35: Temperature contours of base model A (periodic repeats)

A comparison of exit channel velocities is seen in Figure 36. The velocity range has been adjusted from 5 to 10 m/s to properly view the differences between cases. From the figure, it is apparent that the cases containing two inlets (A, B, E, F) show a concentration of high velocity distribution among six opposing channels. In contrast, those containing four inlets (C, D, G) do so among 12 channels. The figure also shows that those cases containing an extended manifold configuration (E, F, G) show lower peak velocities and a more even distribution than those with the 20-mm manifold (A, B, C, D). A comparison of velocity distribution values has been recorded in Table 12.

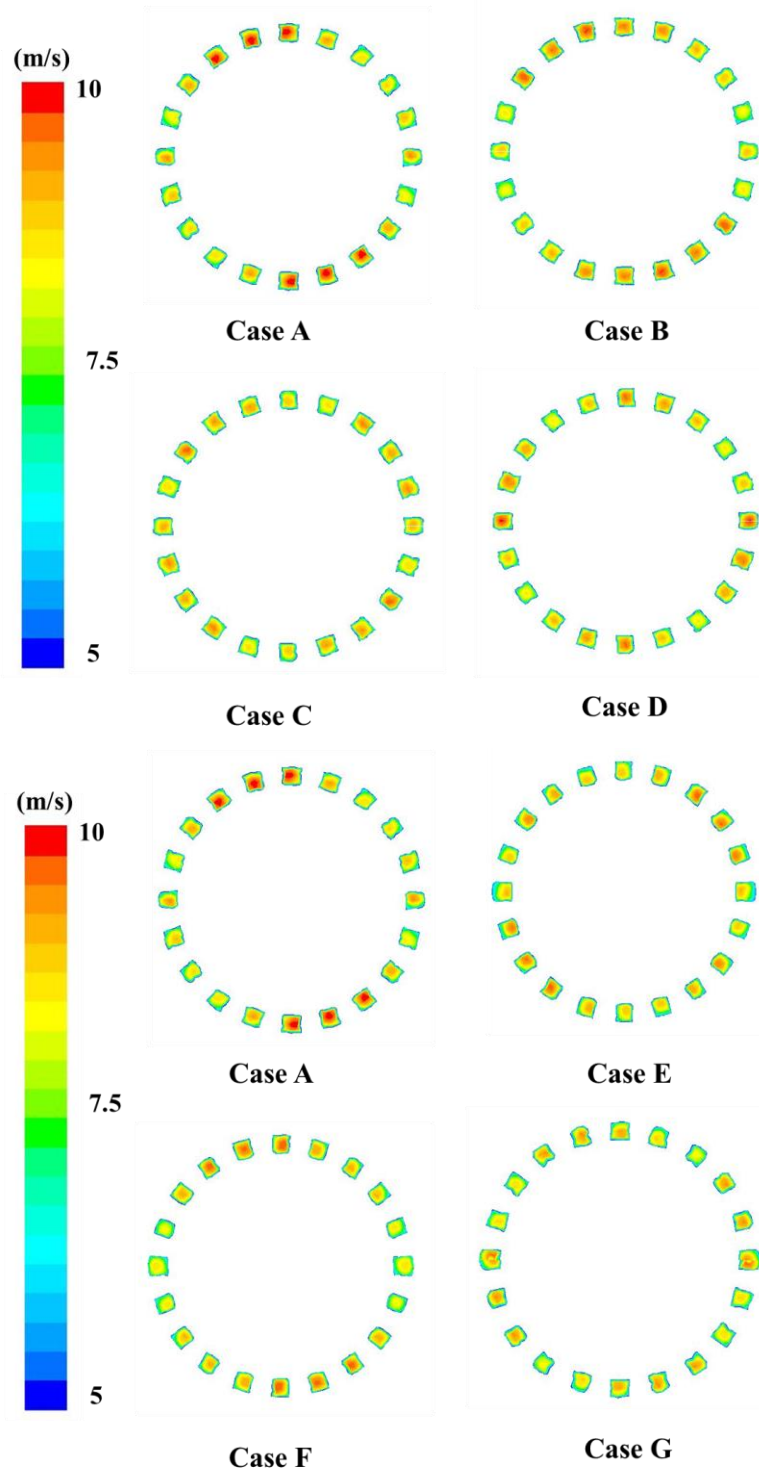


Figure 36: Comparisons of exit velocity contours

A comparison of temperature contours in the manifold region of the simulation is shown in Figure 37. The channel portion of the simulation has been excluded due to the lack of a fin effect, and is further studied in section 6.3. A qualitative assessment of high-temperature areas is shown in the image, where the minimum wall temperature has been set to be 450 K (177 °C). Base case A presents the least amount of high-temperature regions, while predictions of case D show that the entire manifold wall will exceed 450 K. In all cases, the regions of highest temperature are concentrated where channel flows intersect each other, in either two or four locations. While these low-velocity regions may result in cavitation zones if the water pressure is not elevated enough, this could be mitigated by the inclusion of a small chamfer in the design. It is apparent that the extent and intensity of high-temperature areas in the manifold may be predicted by the entering water pipe velocity: cases A and E both have two 7-mm inlets, while case D was designed to have four 10-mm inlets. In each case, the entering mass flow boundary condition was maintained. While those configurations that employ an extended manifold length (E, F, G) and four inlets (C, D, G) present a larger high-temperature area than their 20-mm (A, B, C, D) and two inlet (A, B, E, F) counterparts, their overall channel mass flow distributions show superiority over the latter models. It is implicit that a trade-off analysis of these parameters must be performed when choosing a final configuration for a particular combustor design.

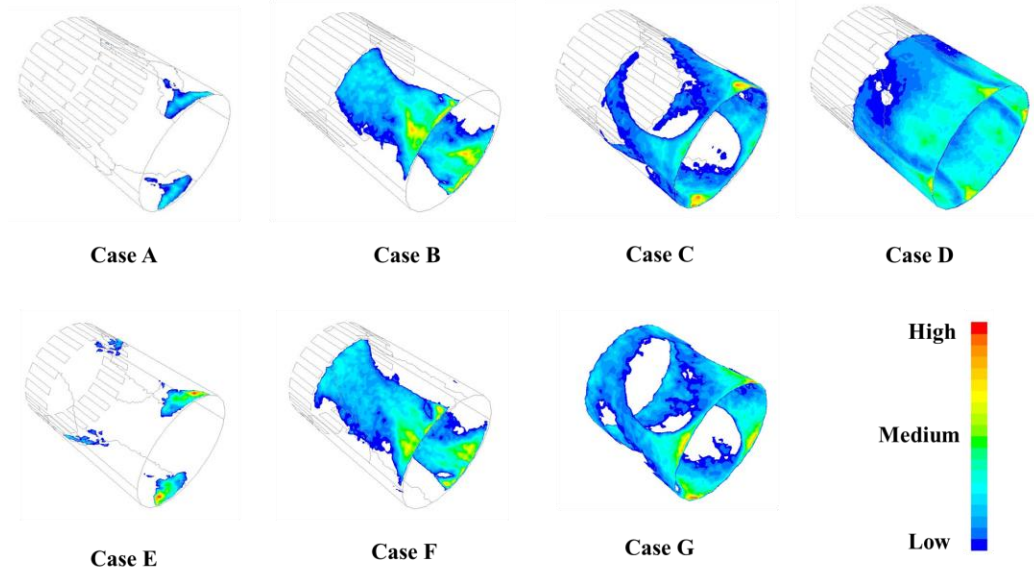


Figure 37: Comparison of temperature zones above 450 K

An overall comparison of manifold model results is shown in Table 12. Model D has the lowest pressure drop, followed by model G. While models A and E were shown to have the lowest maximum temperatures and smallest high-temperature areas, their corresponding pressure drops are the highest amongst all models. While the change amongst the highest (A) and lowest (E) pressure drops may not be significant at this scale, this difference will be significant when implementing such a system in a commercial-scale power plant. Thus, pressure drop must be accounted as a crucial parameter in the choice of manifold model. Model G was chosen and implemented in the 1-MW scale MHD combustor. This model was shown to have one of the smallest velocity % differences, while maintaining a relatively low overall pressure drop. While the maximum local temperature in the model was observed to be significant (601 K), an even flow in the throat-area of the channels was prioritized as a design constraint. To diminish the low-velocity effects at the elevated temperature locations, a chamfer was implemented in the design, eliminating sharp corners.

Table 12: Manifold Model Results

Parameters	Units	A	B	C	D	E	F	G
Maximum Temperature	K	499	576	643	805	513	551	601
Model ΔP	Pa (psi)	87586 (12.7)	71724 (10.4)	69724 (10.11)	65034 (9.43)	86275 (12.51)	69724 (10.11)	68689 (9.96)
Maximum velocity	m/s	8.69	8.45	8.34	8.28	8.17	8.40	8.13
Minimum velocity	m/s	7.43	7.23	7.57	7.51	7.49	7.04	7.47
Velocity Difference %	--	14.50%	14.44%	9.23%	9.30%	8.32%	16.19%	8.12%

6.1.3 Mesh Independence Results

A mesh independence study was performed to validate the numerical methods employed in the model. The centerline temperature of an inner channel wall was evaluated for a coarse (36,500 elements), medium (60,000 elements) and fine (470,000 elements) mesh. Though the coarse and medium meshes contain a similar amount of elements, the differences between the medium and fine meshes are seen to be relatively small. In particular, the axial coordinate locations of 0.25 to 0.31 m show minimum changes between meshes. Axial regions between 0.31 and 0.33m correspond to the manifold mixing region and present a large temperature evolution between the coarse and medium mesh. The evolution of these values is seen in Figure 38.

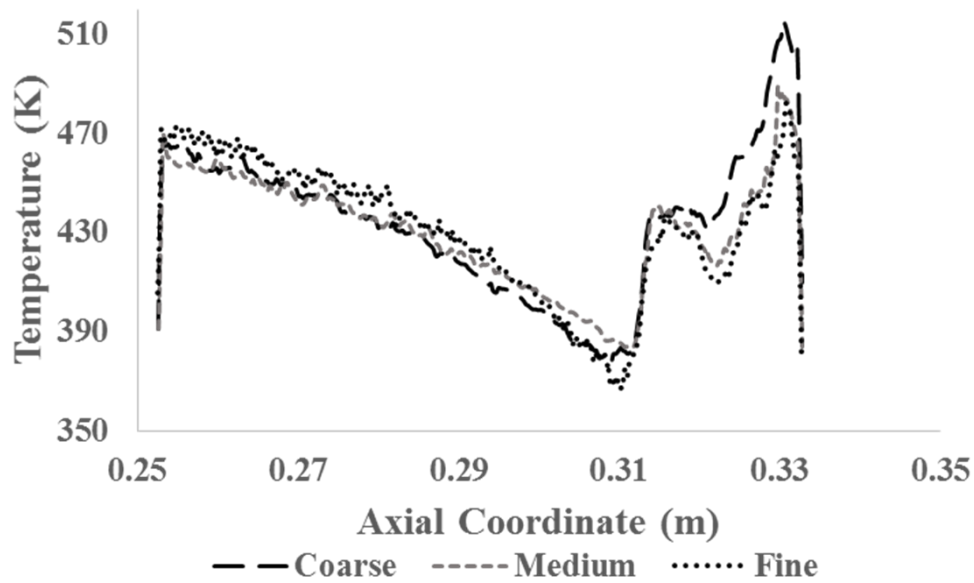


Figure 38: Comparisons of wall temperature at channel midline

6.2 Parametric Fin Study

An analytical estimate based on the fin equation was performed to assess fin performance parameters in the converging and diverging regions of the geometry. This assessment was performed to evaluate the effect of varied aspect ratio, hydraulic diameter and fin thickness. In particular, it was desired to investigate the effect of high aspect ratio cooling channels (HARCC) on fin efficiency. While HARCC are typically employed in rocket engine design to reduce wall temperature and increase material strength [55], these configurations typically have high thermal conductivity solids and low conductivity coolants. Their use has not been extensively assessed in high-heat flux designs employing water as a coolant. A relationship between the changing values of solid thermal conductivity and local fin base temperatures must be established to implement these results in future designs and optimize the cooling system. The setup of the analytical study is shown in Figure 39. A relationship between the channel width, height and fin number is examined in the efficiency results, with the cases being compared in section 6.2.3.

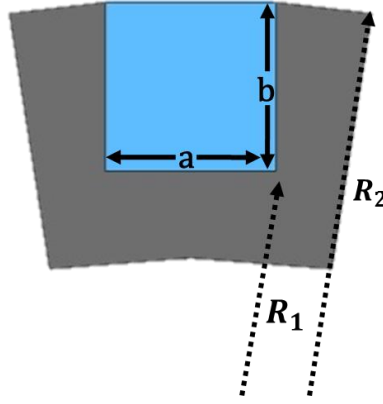


Figure 39: Setup for analytical fin efficiency

6.2.1 Analytical Methodology

The conduction equation governing the temperature variation of an extended surface is presented in the following relationship.

$$\frac{d}{dr} \left[A(r) \frac{d\theta}{dr} \right] - \frac{hP(r)}{k} \theta = 0 \quad [38]$$

$$\theta = T_{co} - T_{rB} \quad [39]$$

For this geometry, the fin's cross-sectional area at any radial coordinate is given by Eq. 40

$$A(r) = \left(1 - \frac{aN_c}{2\pi R_1} \right) \left(\frac{2\pi r}{N_c} \right) l \quad [40]$$

Where the local arc length is defined as $\frac{2\pi r}{N}$. Substituting the area and perimeter values into Equation 41 yields the following formula.

$$\frac{d}{dr} \left[\left(1 - \frac{aN_c}{2\pi R_1} \right) \left(\frac{2\pi r}{N_c} \right) l \right] \frac{d\theta}{dr} - \frac{2hl\theta}{k} = 0 \quad [41]$$

Equation 41 simplifies to the following relationship, corresponding to a Bessel differential equation.

$$r^2 \frac{d^2 \theta}{dr^2} + r \frac{d\theta}{dr} - m_f^2 \theta r = 0 \quad [42]$$

Where

$$m_f^2 = \frac{2hN_c R_1}{k(2\pi R_1 - aN_c)} \quad [43]$$

The general solution of Equation 44 is of the form shown below, where I and K represent the modified Bessel functions.

$$\theta(r) = C_1 I_0(2m_f \sqrt{r}) + C_2 K_0(2m_f \sqrt{r}) \quad [44]$$

At the fin base a local prescribed temperature is provided by the solution of Equation 44. At the fin tip, an assumption is made of an adiabatic wall. These boundary conditions are represented by equations 45 and 46.

$$\theta(R_1) = \theta_B = T_B - T_\infty \quad [45]$$

$$\frac{d\theta}{dr}(R_2) = 0 \quad [46]$$

Where the fin tip radius is defined as

$$R_2 = R_1 + b \quad [47]$$

The specific solution of Equation 44 corresponds to Equation 48, describing the temperature profile for a single fin.

$$\theta(r) = \frac{\theta_B K_1(2m_f \sqrt{R_2}) I_0(2m_f \sqrt{r}) + \theta_B I_1(2m_f \sqrt{R_2}) K_0(2m_f \sqrt{r})}{I_0(2m_f \sqrt{R_1}) K_1(2m_f \sqrt{R_2}) + I_1(2m_f \sqrt{R_2}) K_0(2m_f \sqrt{R_1})} \quad [48]$$

The rate of heat loss is given by the general conduction equation evaluated at the fin base.

$$Q = \left(-kA \frac{d\theta}{dr} \right)_{R_1} = -k \left(1 - \frac{aN_c}{2\pi R_1} \right) \left(\frac{2\pi R_1}{N_c} \right) l \left(\frac{d\theta}{dr} \right)_{R_1} \quad [49]$$

The general fin efficiency is then evaluated by Equation 50.

$$\eta_F = \frac{Q}{(Q)_{\theta=\theta_B}} = \frac{Q}{h(2lb)\theta_B} \quad [50]$$

Finally, a specific equation for fin efficiency is derived through a combination of Equations 48, 49, and 50.

$$\eta_F = \frac{-k \left(a - \frac{2\pi R_1}{N_c} \right) \left[\frac{m_f}{\sqrt{r}} K_1(2m_f \sqrt{R_2}) I_1(2m_f \sqrt{r}) - \frac{m_f}{\sqrt{r}} I_1(2m_f \sqrt{R_2}) K_1(2m_f \sqrt{r}) \right]}{2hb [I_0(2m_f \sqrt{R_1}) K_1(2m_f \sqrt{R_2}) + I_1(2m_f \sqrt{R_2}) K_0(2m_f \sqrt{R_1})]} \quad [51]$$

6.2.2 Analytical efficiency results

The analytical efficiency results have been calculated and plotted according to equation 51. Figures 40 to 42 show a parametric comparison of aspect ratio, hydraulic diameter and number of channels across the converging-diverging nozzle. Values for the solid's thermal conductivity have been calculated through the average of the ambient and base temperatures. Base temperature has been estimated through Equation 6, and assumed to be that of the channel base temperature. Figure 40 shows the efficiency comparison of aspect ratios. It is shown that the variation of aspect ratio does not follow a clear trend of fin efficiency. At the converging section of the nozzle, the smallest aspect ratio (0.75) presents the largest efficiencies, while at the nozzle throat it presents the lowest

values. The thermal conductivity values and base temperature both have an impact upon fin efficiency. The local fin thickness influences this parameter as well, as the thinnest fins are concentrated in the regions of highest temperature. In the aspect ratio comparison, the low aspect ratio configuration (0.75) corresponds to the thinnest fin base thickness. In regions of relatively high thermal conductivity, the thin fins underperform, while in regions of low thermal conductivity, they surpass other configurations.

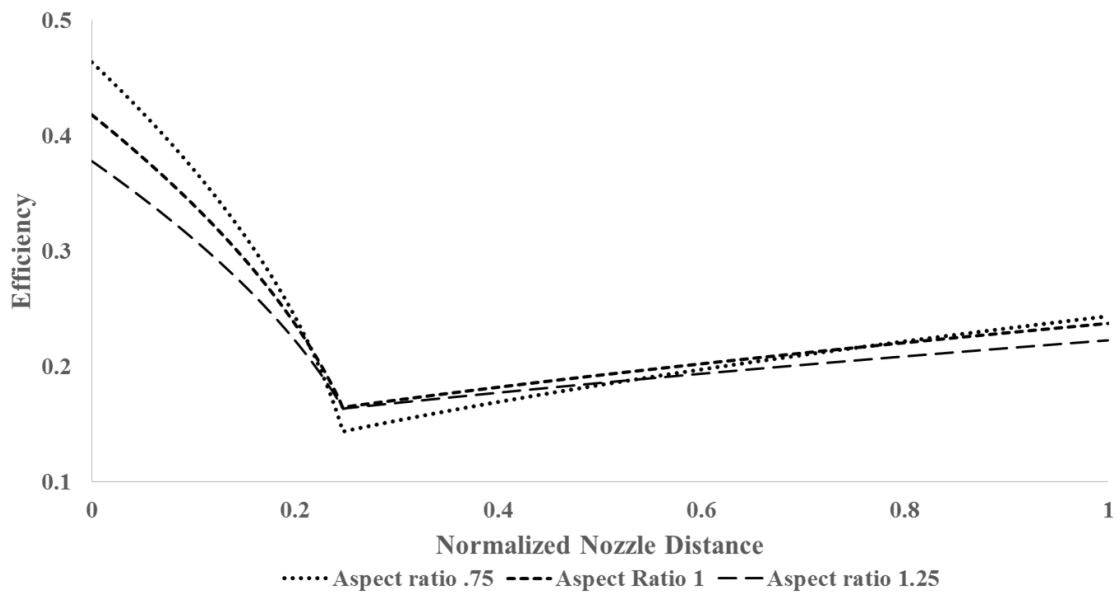


Figure 40: Aspect ratio efficiency comparison

It is noticeable that in all three figures, the fin efficiency decreases at the throat location. For a steady hydraulic diameter this variation is not significant among aspect ratios. In the hydraulic diameter comparison of Figure 41, there is a clear trend that shows that by reducing channel hydraulic diameter, the fin efficiency is increased. As this comparison has been adjusted to maintain fin thickness between cases, this is the only parameter affecting performance in the figure. Though the hydraulic diameter comparison is spaced by 0.5 mm intervals, the plot shows that the efficiency difference between 1.5 mm and 2 mm is much larger than the difference between 2 mm and 2.5 mm.

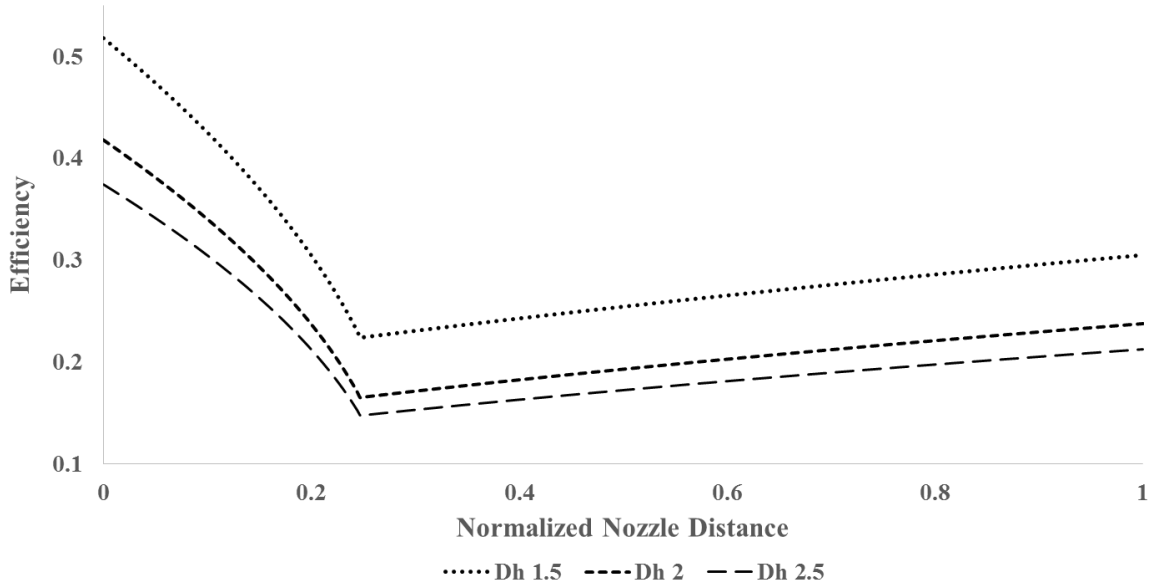


Figure 41: Hydraulic diameter efficiency comparison

Figure 42 shows a comparison when varying the number of channels in the cooling configuration. The plot shows that decreasing the number of channels will carry higher efficiencies for a particular hydraulic diameter. The relationship between the channel number and the increase of efficiency is proportional, as the difference in efficiencies of the 16 and 20 channel configurations is similar to the 20 and 24 channel evaluation. Both the aspect ratio (Figure 40) and channel number (Figure 42) comparisons present a variation of fin base thickness in the models. The aspect ratio analysis, however, also varies in fin length. When comparing both figures it is apparent that while larger fin base thicknesses present overall efficiencies, the fin length parameter affects the efficiency plot's gradient in the nozzle. This explains the efficiency reversal phenomenon seen in Figure 40. It is concluded that for a particular hydraulic diameter, the three major parameters affecting the fin efficiency comprise base thickness, channel number and fin length. This is due to the influence of channel number on parameter m in Equation 43, with aspect ratio affecting the Bessel functions of Equation 50 due to a change in a , b and R_2 . Efficiency is particularly affected by the modified Bessel function $I_o = f(R_2)$, whose values vary in a hyperbolic manner. While these parameters may be optimized for a certain base thickness and thermal

conductivity, these values are rapidly changing throughout the nozzle contour. When choosing a channel configuration, a fin efficiency analysis must be coupled with a study on coolant stratification to both minimize solid wall temperature and maximize the fin effect.

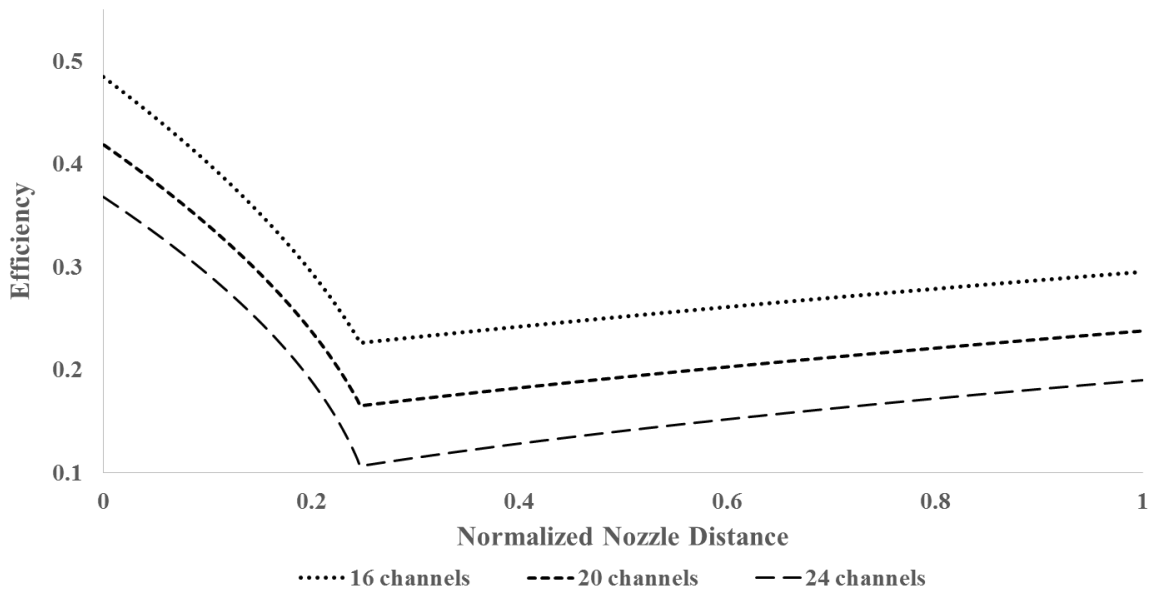


Figure 42: Channel number efficiency comparison

6.3 Numerical Fin Study

Understanding the effect of channel geometry upon coolant performance is the key to enhancing the design of the thermal management system. While one dimensional equations such as the Sieder-Tate correlation (Eq. 4) may provide an approximation of convective properties, a three-dimensional model is able to capture the effect of variable coolant properties due to geometry. According to Kacynski (1992), if thermal stratification is neglected, wall temperature predictions will carry a high degree of inaccuracy; effective heat transfer resistance for a stratified flow is shown to be considerably larger than a fully-mixed case [50]. The objective of this study is to analyze and compare the three-dimensional effects of cooling channels involving a curved configuration. A parametric study replicating the cases analyzed in Section 6.2 has been performed

to quantify the effect of thermal stratification upon the combustion-side and channel bottom wall temperatures. Only the wall solid and liquid cooling domains are included in the simulation to reduce the computational burden of including a combustion model. Results from the study presented in Chapter 4 are implemented as a convective boundary condition based on the reduced Bartz correlation. A periodic boundary condition was implemented to simulate a single channel in each case, increasing the number of elements in each section and allowing for a highly structured mesh. Inlet water boundary conditions have been adjusted to mimic a steady theoretical convective heat transfer coefficient of $47,000 \text{ W/m}^2\text{-K}$; velocity parameters were altered for this value using Equation 4. All cases investigated in the simulation were predicted to have similar temperature profiles according to one-dimensional calculations.

6.3.1 Numerical Domain and Setup

A schematic of the computational domain employed in the simulation is shown in Figure 43. Each simulation employs a simplified water inlet/outlet configuration. The chamber (C), converging (D) and diverging (E) portions were assigned as the combustion-adjacent walls. A periodic interface (G) was located at the fin midpoint. The solid-liquid interface, denoted by letter F, is assigned where the solid and liquid bodies border each other. Each channel was assigned with a periodic repeat angle associated with the number of channels in the model. A summary of the cases investigated is shown in Table 13. The cases are divided into three categories throughout the results section: aspect ratio analysis, hydraulic diameter comparison and number of channel comparison. Those cases involving a change in hydraulic diameter have been adjusted to maintain similar fin base thicknesses.

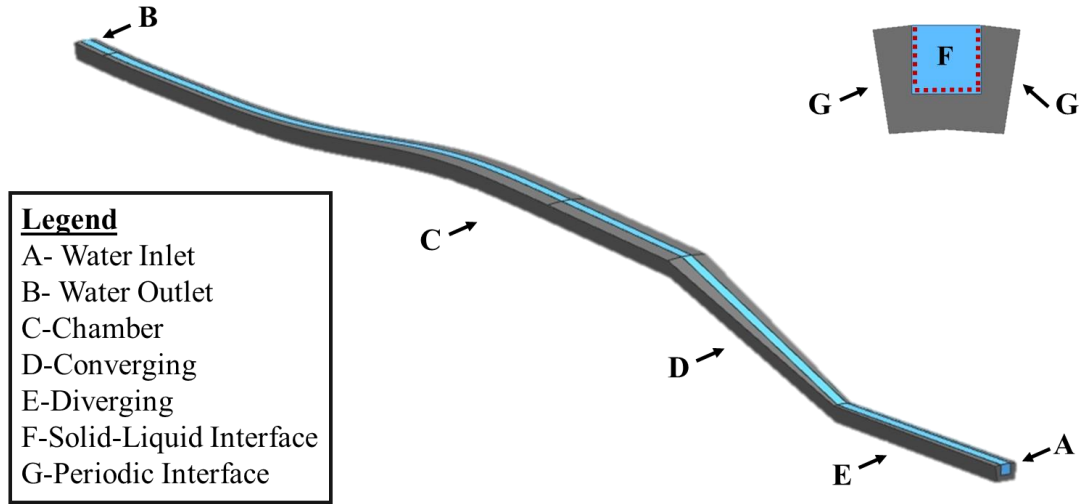


Figure 43: Domain for periodic channel simulation

Table 13: Cases employed in channel simulation

Case	Hydraulic Diameter (mm)	Aspect Ratio	Number of Channels
A	2	1	20
B	2	.75	20
C	2	1.25	20
D	1.5	1	16
E	2.5	1	24
F	2	1	16
G	2	1	24

Figure 44 shows a portion of the mesh employed in the simulation; this corresponds to base case A. In all cases, the mesh was composed of hexahedral elements arranged in a structured manner, resulting in a mesh with a minimum orthogonal quality of 0.5. All configurations contained a minimum of 300,000 elements to increase simulation accuracy. A minimum of 7 elements passes across the combustion chamber wall to effectively capture changes in the

material's thermal conductivity. A high average element quality (>0.8) yielded quick convergence in all cases. Element sizing was set to 2.5 E-4 m in both liquid and solid bodies.

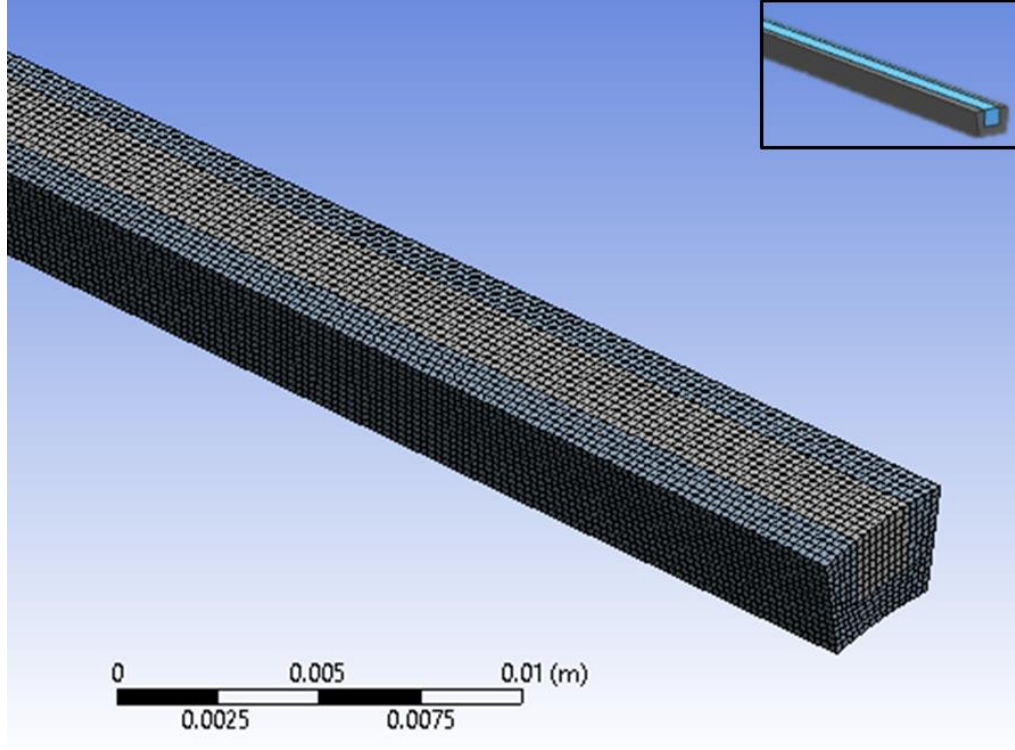


Figure 44: Channel simulation mesh detail

The boundary conditions employed in the model are shown in Table 14. Equations relevant to the simulation have been described in chapter 3. The mass and momentum equations employed are those of 8 to 11, while the realizable k- ϵ model transport equations correspond to 12 and 13. The energy equation for the fluid Eq. 37 is described in section 6.1. The energy equation across the solid corresponds to Eq. 18. Similar to the manifold simulation, this model was configured to employ user defined functions to define combustion-adjacent heat transfer characteristics. The convective heat transfer coefficient in the inner wall was assigned to be the modified Bartz correlation, in accordance to the findings described in chapter 4. The equations for h and boundary layer temperature T_{bl} (Eq. 2) were implemented in the model through user-defined fourth and sixth-order polynomials. These relationships are described in Figures 45 and 46. Water material

properties were those employed in the manifold simulation model, while the Inconel's thermal conductivity was characterized by a linear equation. These properties are described in Appendix E.

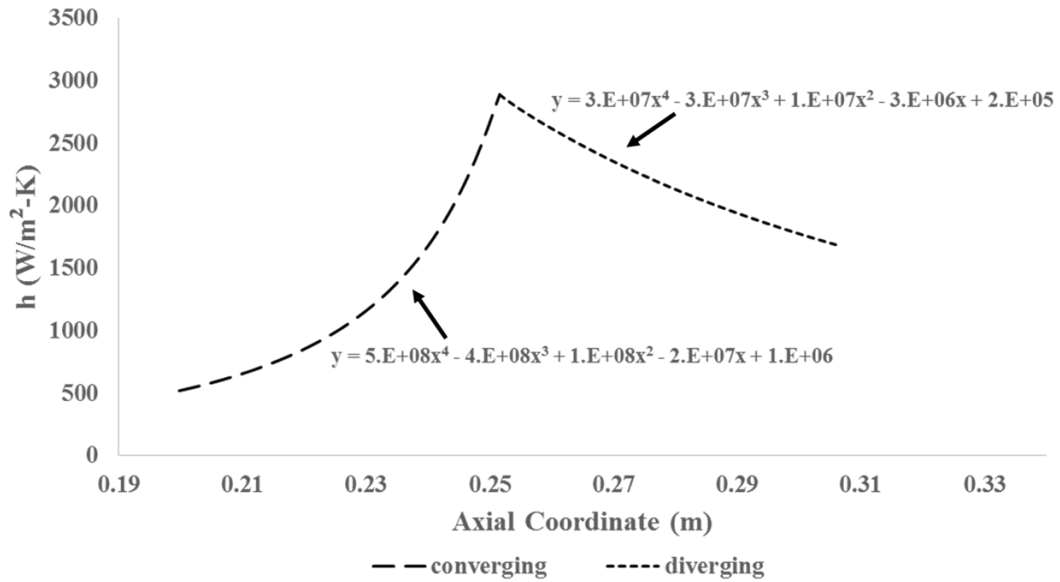


Figure 45: Convective heat transfer coefficient in walls, user defined function

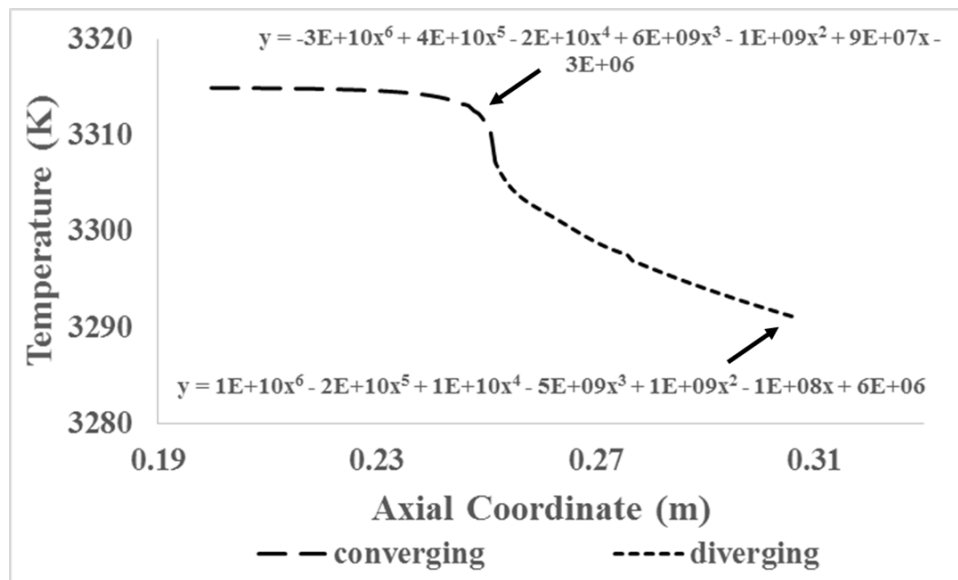


Figure 46: Boundary layer temperature in walls, user defined function

Table 14: Boundary conditions employed in channel simulation

	Input
Models	<ul style="list-style-type: none"> • Energy-ON • Viscous-Realizable k-epsilon, Scalable Wall Function
Materials	<p>Inconel 718</p> <ul style="list-style-type: none"> • Density- 8193 kg/m³ • C_p- 435 J/kg-K • Thermal conductivity – user defined polynomial <p>Water- Liquid</p> <ul style="list-style-type: none"> • Density- user defined polynomial • C_p- user defined polynomial • Thermal conductivity- user defined polynomial • Viscosity- user defined polynomial
Boundary Conditions	<p>Chamber</p> <ul style="list-style-type: none"> • Wall- Convection • Heat Transfer Coefficient- 520 W/m²-K • Temperature- 3315 K <p>Converging</p> <ul style="list-style-type: none"> • Wall- Convection • Heat Transfer Coefficient- UDF • Temperature- UDF <p>Diverging</p>

	<ul style="list-style-type: none"> • Wall- Convection • Heat Transfer Coefficient- UDF • Temperature- UDF <p>Water Inlet</p> <ul style="list-style-type: none"> • Velocity Inlet • Velocity: 9.1 m/s (Dh=2 mm) • Turbulent Intensity- 4.5% • Hydraulic Diameter- .002 m <p>Water Outlet</p> <ul style="list-style-type: none"> • Pressure Outlet • Turbulent Intensity- 4.5% • Backflow hydraulic diameter- .002 m (Dh=2 mm) <p>Solid to Liquid Interface</p> <p>Periodic Interface</p>
Solution Methods	<p>Initialization- Water Inlet</p> <p>Scheme- Coupled</p> <p>Pressure- Second Order</p> <p>Momentum- Second Order</p> <p>TKE- First Order</p> <p>Epsilon- First Order</p> <p>Energy- Second Order</p>

6.3.2 Numerical Results

Figure 47 displays the temperature contours for the base model simulation (Case A). This figure displays the full-combustor view when the periodic repeats are applied. From this model, it is seen that the fins in the chamber and converging regions are affected by a certain degree of solid temperature stratification. The effects of liquid and solid stratification are further described in in Figures 57, 61 and 72 respectively.

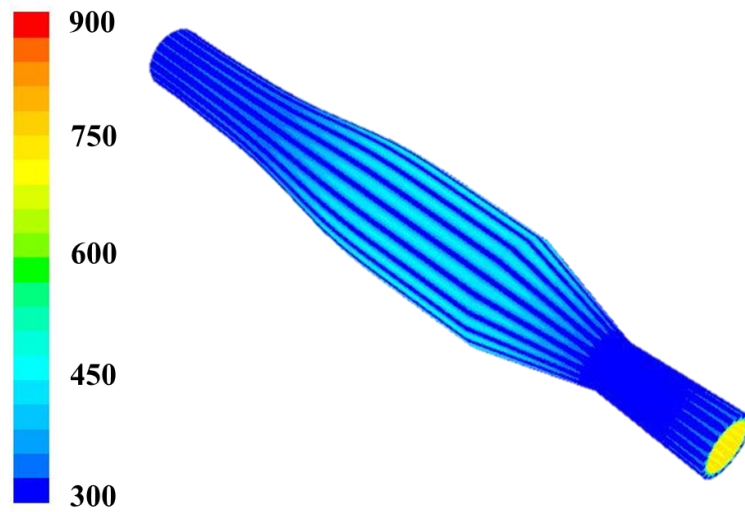


Figure 47: Temperature contours of base model A (periodic repeats)

Figures 48-50 show a comparison of channel bottom temperatures when compared to both the base model A and the 1-D analytical approximation. The initial estimate was generated through the solution of Eq. 4, introduced in chapter 2. The numerical results are compared to the 1-D estimate to analyze the accuracy of the initial method and detect risk from cavitation-prone zones. Figures 48-50 show that the analytical estimate falls short from the numerical values; the largest observed difference is a variation of 50 K. Values are seen to differ most in the chamber region, due to the changing bulk properties in the coolant. The prediction of these temperatures is useful to designers, as a high-pressure safety factor must be implemented when choosing a coolant source. While these figures show that maximum overall temperature is reached at the throat, there is a deviation in expected values at the nozzle inlet area. Lower channel bottom temperatures

coincide with a curvature path change, where a coolant recirculation effect may be triggered by Dean Vortices. While the throat area presents a curvature change, the observed trend indicates a reverse effect, with an increase in temperature slopes. In Figure 48 it is observed that the effect of aspect ratio is not significant when comparing this parameter. In comparison, Figure 49 displays a clear trend when varying hydraulic diameters. Decreasing values carry an increased channel bottom temperature due to an increased level of stratification (Figure 58). While the difference between hydraulic diameter models is notorious in the chamber region, the differences between models are reduced in the CD nozzle, where cavitation risks are greater. When observing the data from Figure 49 it is observed that the 16 channel configuration carries larger channel temperatures. This is directly related to the overall wetted perimeter in the model. The maximum temperature of the 16 channel configuration far surpasses those of the 20 and 24 channels, indicating that cavitation would most certainly occur under this configuration. The practical feasibility of this model could be improved by splitting the channels near the throat, as implemented in HARCC configurations [55].

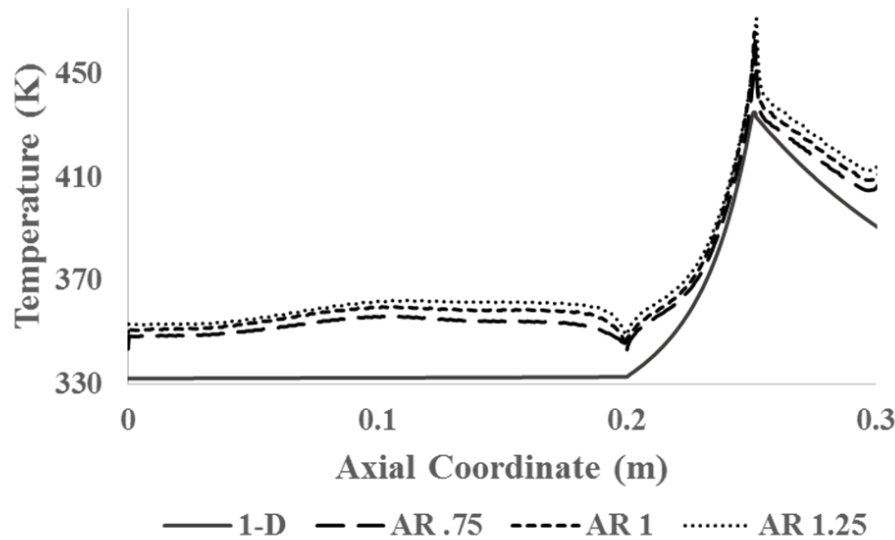


Figure 48: Channel bottom temperature (Aspect ratio comparison)

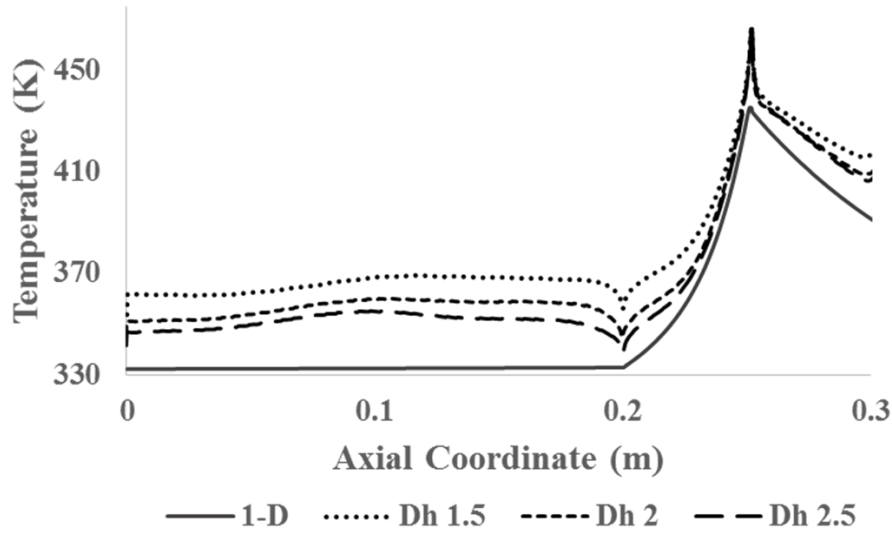


Figure 49: Channel bottom temperature (Hydraulic diameter comparison)

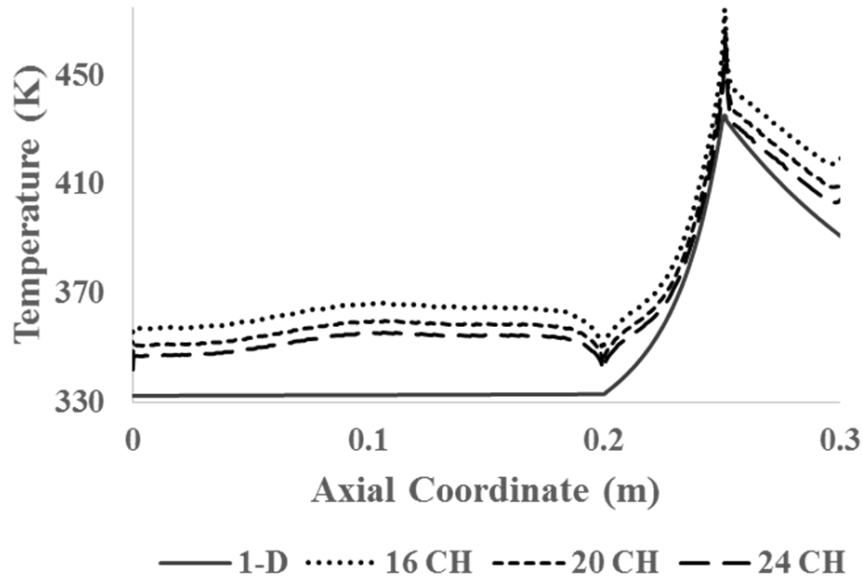


Figure 50: Channel bottom temperature (Channel number comparison)

A comparison of the combustion-side wall temperatures for all models is shown in Figures 51-53. While the channel bottom temperatures in Figures 48-50 exhibit a large difference from the 1-D approximation, the inner wall 1-D temperatures closely resemble the developed numerical models. While all numerical values exceed the prediction, these differences may not be significant

when analyzing thermal stresses. The largest observed differences between numerical and analytical values are seen in the converging section nozzle. Figure 51 presents low temperature disparities when varying aspect ratios. When comparing hydraulic diameters, it is appreciated in Figure 52 that the baseline 2-mm channel configuration presents the lowest temperatures in the converging portion of the nozzle. In the diverging section, all hydraulic diameters perform in a similar manner. Figure 53 shows a clear trend between channel number and temperatures, with the 16 channel configuration presenting the largest temperatures in the diverging section of the nozzle, and the 20 channel configuration doing so in the converging portion.

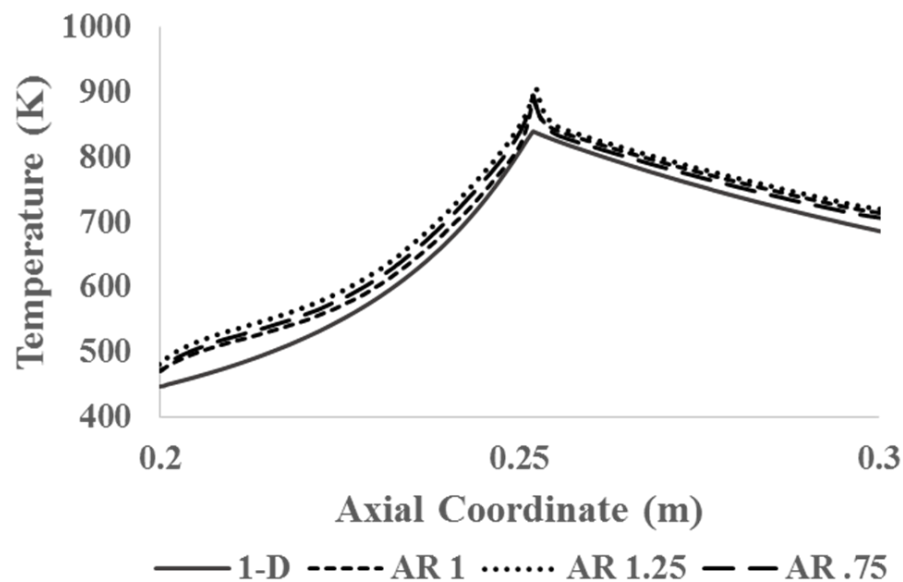


Figure 51: Combustion-side wall temperature (Aspect ratio comparison)

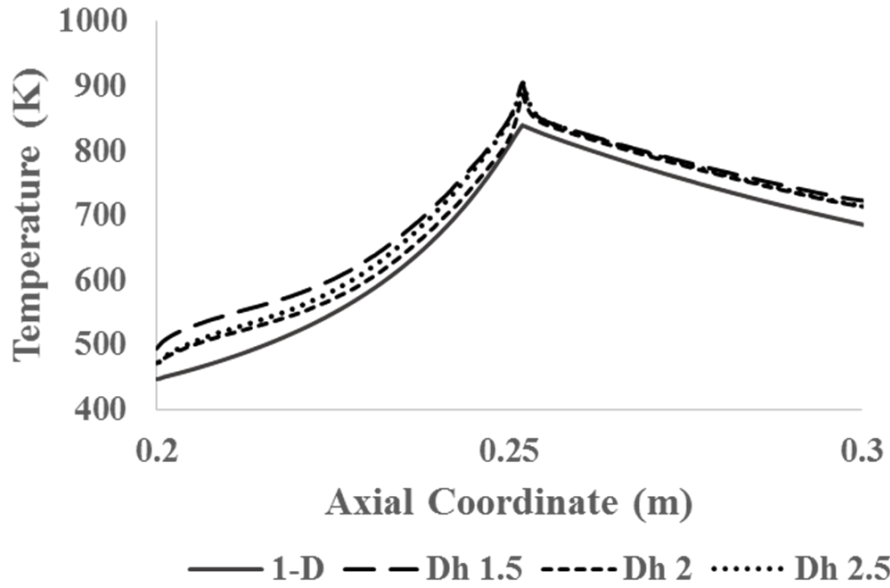


Figure 52: Combustion-side wall temperature (Hydraulic diameter comparison)

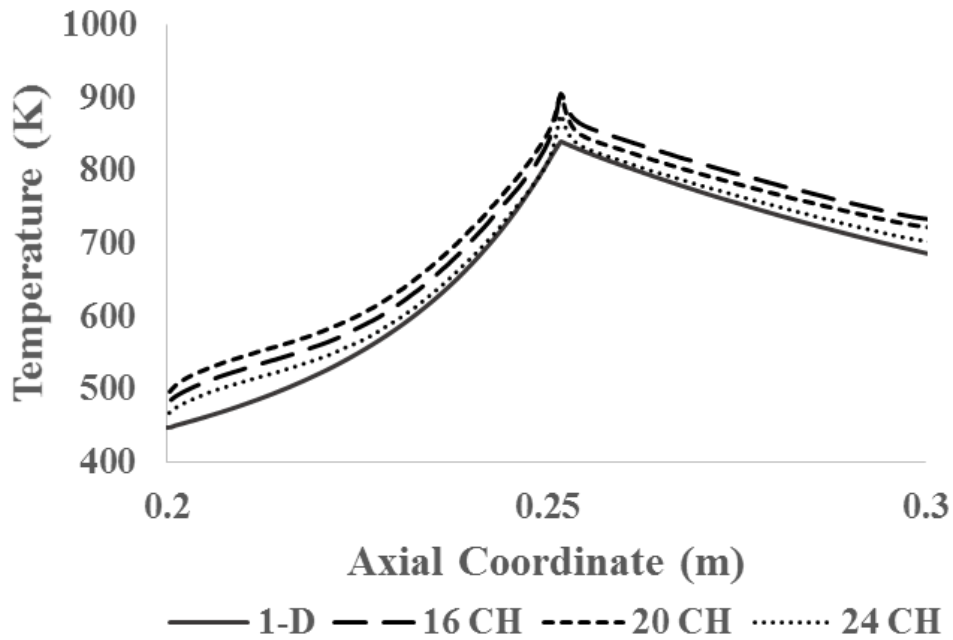


Figure 53: Combustion-side wall temperature (Channel number comparison)

Figures 54-56 show the temperature gradients at the wall of the combustor for the axial throat location. These temperatures show a comparison of the fin-adjacent and channel-adjacent angular locations. In the plots, the normalized coordinate 0 corresponds to the fin centerline

location, while 1 is the wall portion adjacent to the channel centerline. The figures show that fin width plays a role in the maximum overall temperature of the combustor. In turn, large variations of fin temperature may result in increased thermal stresses. From Figure 54 it is apparent that the largest aspect ratio (1.25) and fin bottom width carries the largest throat temperatures and angular gradient. This figure also shows that the base aspect ratio (1) results in the smallest local overall temperatures, with a radial gradient similar to that of the largest aspect ratio. Though the smallest aspect ratio (.75) presents the lowest radial gradient due to a reduced fin thickness, its local temperature exceeds the base case. This finding coincides with the calculations presented in Figure 40, where the throat fin efficiency is diminished for the lower aspect ratio and enhanced for the base case. As this trend varies throughout Figure 40, further analyses must be done for localized portions of the nozzle in terms of maximum inner wall temperature.

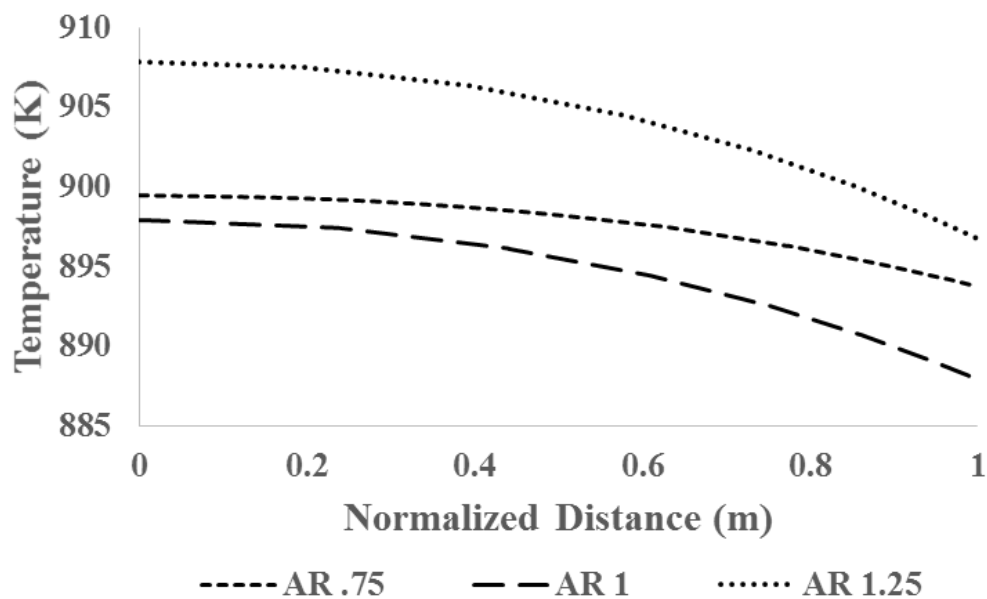


Figure 54: Combustion-side wall temperature (Aspect ratio comparison-radial)

While the smallest hydraulic diameter investigated (1.5 mm) presents the largest wall and channel temperatures throughout the combustor profile, at the nozzle throat the largest hydraulic diameter (2.5 mm) shows the largest temperatures and temperature gradients. Once again, the base

case (2 mm) has been found to have the lowest temperatures. While a smaller hydraulic diameter provides higher fin efficiencies (Figure 41), it also carries larger thermal stratification effects, raising overall temperatures. In turn, the significantly lower efficiency of the largest hydraulic diameter (2.5 mm) cannot be offset by a low stratification effect. The base case (2mm) presents a balance between expected stratification effects and fin efficiencies; it is thus inferred that an optimized channel design shall be dependent on an equilibrium between both parameters to reduce maximum wall temperatures.

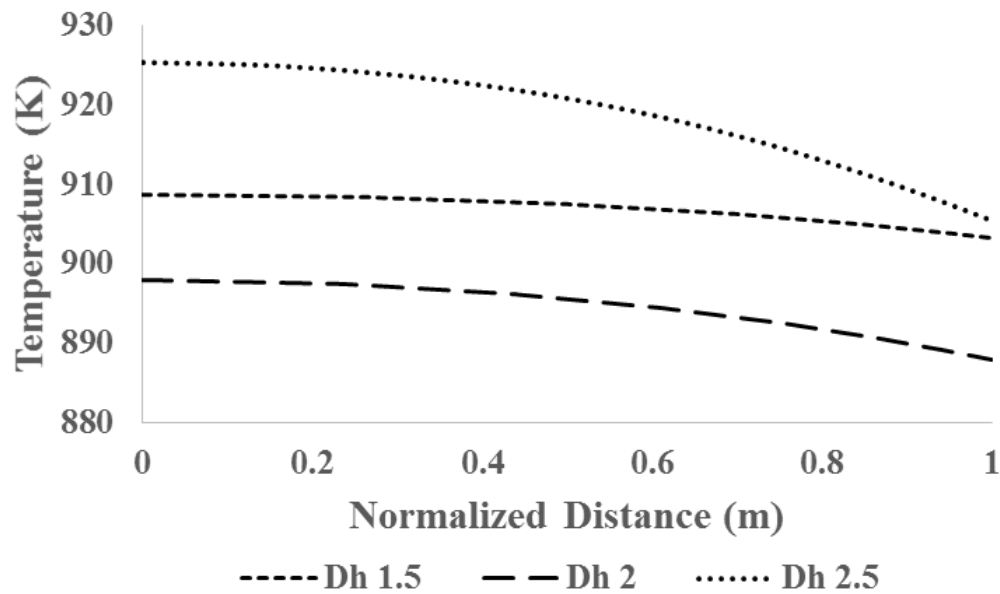


Figure 55: Combustion-side wall temperature (Hydraulic diameter comparison-radial)

Figure 56 shows that the 16-channel configuration presents both the largest inner throat temperatures along with the largest temperature gradient. The effect of the fin thickness is significant, as the thinnest fins (24 channel configuration) present the lowest angular gradient and thus, the lowest local thermal stresses. This trend agrees with what is seen in Figure 53, where the highest channel configuration presents the lowest overall temperatures throughout the nozzle contour.

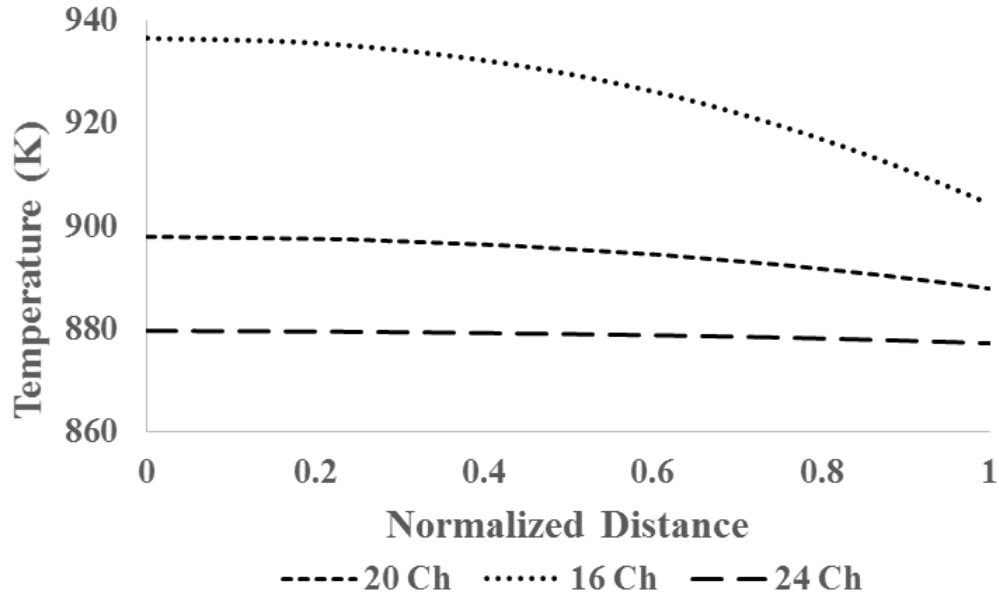


Figure 56: Combustion-side wall temperature (Channel number comparison- radial)

Table 15 shows a comparison of the channel model results for all cases. The one-dimensional temperature predictions (Eq. 4) resulted in a maximum wall temperature of 839 K, or 566 °C. The computational model that most closely matches this value is model G, corresponding to the 24 channel configuration. Its maximum temperature exceeds the 1-D approximation by 40 K; this brings the maximum wall temperature to a little over 600 °C. The high-temperature yield strength properties of the wall material have been shown to exponentially degrade after this value. The model presenting the largest temperature difference is model F, corresponding to the 16 channel configuration. This model predicted a maximum temperature of 664 °C. While the largest temperature regions may not be large when compared to the overall geometry, those models that exceed the design temperature in a significant manner may experience local plastic deformation due to the material's degrading properties. If this occurs, the throat dimensions may be affected, changing the exit gas velocity properties. Increasing the number of channels is in the best interest of the designer, as the overall wall temperatures and risk of failure is minimized. Optimizing the number of channels for a certain configuration is dependent upon a series of parameters: while the thermal stresses are reduced, the fins are made thinner, decreasing the overall structural support to

the external casing of the combustor. Thinner fins also imply the reduction of possible locations for wall temperature sensors, as their inclusion may entail obstructions in the channel flow. Finally, increasing the number of channels will require a significantly larger pump power, ultimately affecting the efficiency of the power generation unit. As shown in Table 15, the 24 channel configuration will require 50% more mass flow than the 16 channel configuration.

When making a comparison of aspect ratio, it was found that for a particular hydraulic diameter, temperature and pressure gradients will be the same for all configurations. Though this may be the case, an aspect ratio must be chosen to maximize fluid mixing throughout the combustor [50]. Upon comparing hydraulic diameters, it was shown that the configuration with the smallest hydraulic diameter (Case D) carries the largest temperature and pressure differences. When comparing channel numbers, configuration G (24 channels) carries the lowest temperature, with the pressure gradient matching models A and F. Minimizing these parameters is key to the survival of large-scale configurations. While a number of subscale rocket tests attempt to match a maximum heat flux, the overall heat flux profile and extent of fluid heating must be accounted for when performing the design of scaled configurations [50]. An evaluation of the total heat absorbed by each channel model showed that all cases will result in the same total heat transfer to the cooling system. While the actual convective coefficients (Figures 64-66) vary amongst the models, this result matches the design premise of equal theoretical performance.

Table 15: Channel model results

Parameters	Units	A	B	C	D	E	F	G
Channel ΔT	K	21.20	20.93	20.74	33.46	16.10	26.23	17.70
Maximum Temperature	K	897.9	899.5	905.4	908.74	925.2	936.5	879.5
Channel ΔP	Pa (psi)	142571 (20.67)	144166 (20.90)	143266 (20.77)	175349 (25.42)	122644 (17.78)	140730 (20.41)	143827 (20.85)
Overall mass flow	kg/s	.721	.7338	.7342	.456	.951	.577	.865
Heat Absorbed	kW	63.92	64.22	63.68	63.81	64.03	63.3	64.02

Figures 57-61 describe the water stratification levels and the increase in bulk temperature for all configurations. Stratification arises from thermal gradients in the core of the coolant due to the fluid being unable to satisfactorily distribute the non-uniform heating in the fin walls [50]. This effect is seen in configurations with an asymmetric distribution of heat fluxes, such as CD nozzles [55]. While high aspect ratio coolant channels have been described to result in large stratification effects and low wall temperatures [55], the results of this parametric study show that stratification effects are evenly distributed for cases A, B and C. An analysis of the centerline temperatures in these cases revealed no change between models. In addition to this, the analytical study of fin efficiency (Figure 40) displayed no significant efficiency variations between the base and high aspect ratio cases at the nozzle throat. This implies that that HARCC may only benefit designs with specific parameters, specifically those that employ high fin thermal conductivities. In the case of varying hydraulic diameters, it is apparent that thermal stratification increases with a decrease in size. This is also noticeable in Figure 59, where channel centerline temperature is plotted. While case E maintains a temperature increment of only 16 K, case D presents an

increment of 33 K. As seen in the slopes of the figure, the effect of stratification is cumulative upon the centerline temperature. This is reflected on the gradients of each curve, particularly in the combustion chamber region. In all models, centerline bulk temperature is seen to increase significantly at the throat, corresponding to coordinate 0.25 m. This implies that properties will vary significantly at this point when compared to the 1-D estimates. A comparison of channel stratification at the throat location for a varying number of channels, Figure 60, reveals an increased stratification with a decrease in channel number. This is directly related to the fin efficiency in Figure 42. As fin efficiency is increased, the percentage of heat transferred through the bottom surface area is lower when compared to the area at the sides of the channel. This increases temperature level variations. In the case of channel number comparison, water centerline temperature in the nozzle regions was found to be indistinguishable. In the chamber region, the differences become apparent due to the cumulative effect of thermal stratification in the models. While many of the studies found in literature examine stratification models for compressible coolants with rapidly-changing properties [50] [55], there is still a necessity to account for property variations in incompressible flows. A 1992 NASA report on channel performance [50] reported fluid (H_2) temperature variations of more than 360 K when analyzing turbulent mixing conditions. In comparison, the largest temperature gradient found in the present models was of 33 K. This

implies that designers may be able to control and mitigate the effect of stratification more easily in water-cooled engines than in gas-fueled regenerative rocket engine configurations.

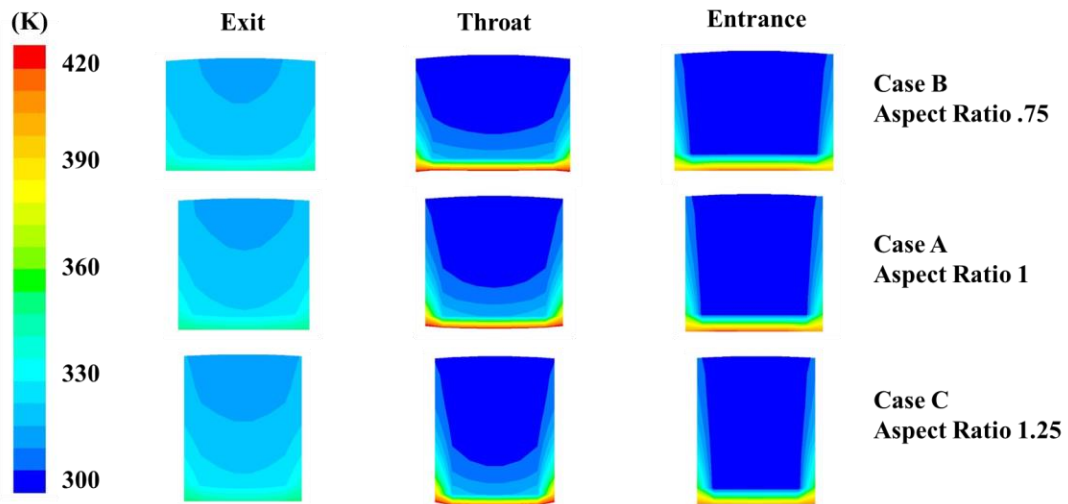


Figure 57: Channel stratification, aspect ratio comparison

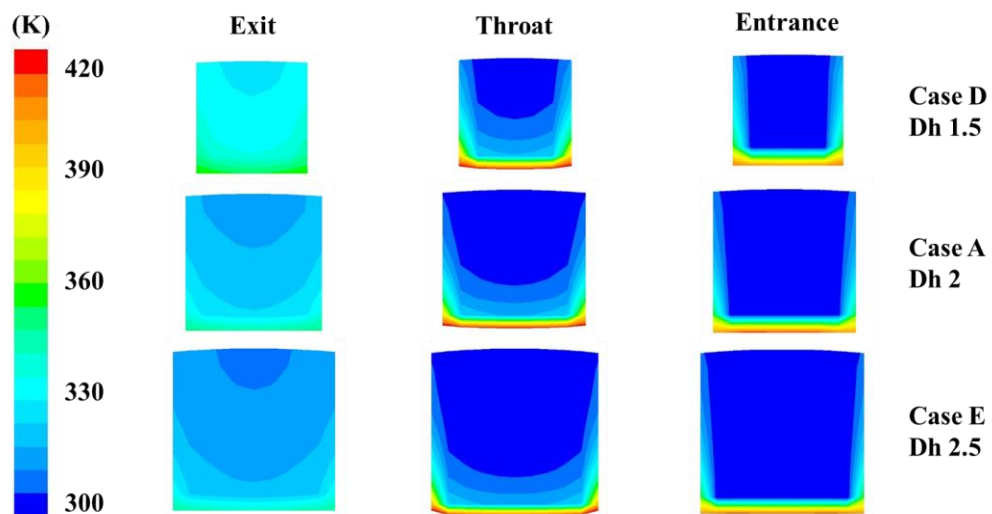


Figure 58: Channel stratification, hydraulic diameter comparison

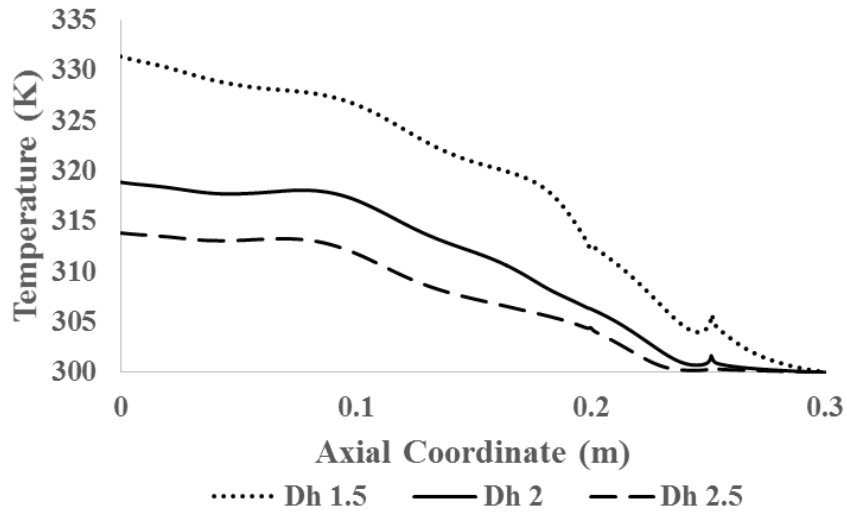


Figure 59: Water centerline temperature comparison (Hydraulic diameter)

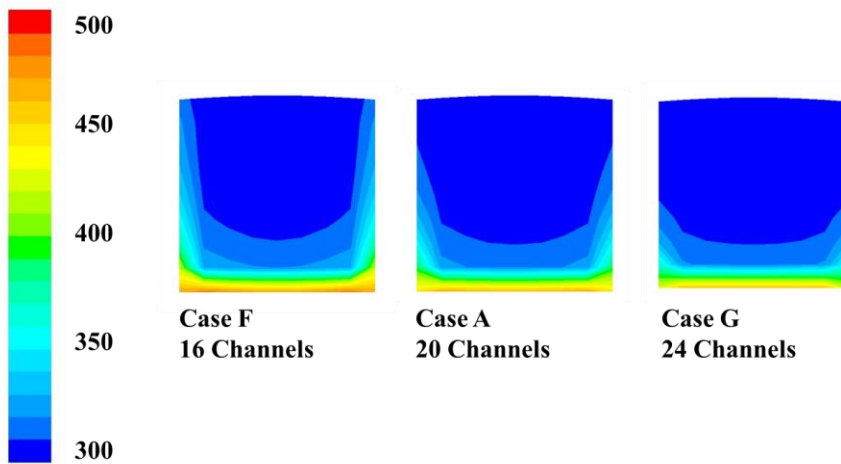


Figure 60: Channel stratification at throat, channel number comparison

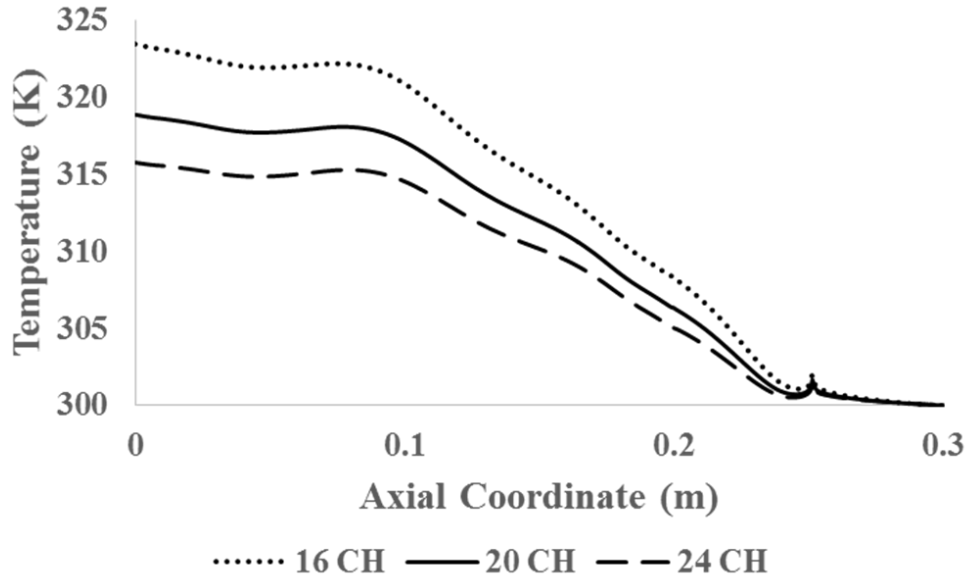


Figure 61: Water centerline temperature comparison (Channel number)

An analysis of radial velocities at different locations of the channel geometry has been conducted to identify the presence of Dean Vortices. Figure 62 displays yz velocity vectors at the channel entrance, exit, nozzle throat and combustion chamber/converging nozzle interface. Figure 63 displays the contours of radial velocity at these axial locations. Figure 63 shows that while the radial velocity is almost nonexistent at the channel entrance, the velocity vectors in Figure 62 display a slight downwards motion. At the nozzle throat, where radial flow is changing directions, radial velocity is seen to be strongest at the upper edges of the channel (Figure 63); velocity vectors point towards a slight upwards direction of radial motion. At this location, the effect of the centripetal force (reflected in the Dean Vortices) is cancelled by the effect of the high heat flux in the area and high thermal conductivity of the coolant; this causes buoyancy effects to be larger than the downwards force caused by the Dean vortex. The radial velocity at the bottom of this cross-sectional portion is seen to be negligible, possibly explaining the sudden drop in convective heat transfer coefficient at this location (Figures 64-66). After this point, the combined effect of buoyancy and the direction of channel curvature enhance the intensity of the upwards radial velocities. These velocities come to a peak at the nozzle entrance, shown in the top right picture in

Figures 62 and 63. At the combustion chamber entrance, where the coolant exits the domain, the effect of Dean vortices is reduced due to the configuration resembling a straight channel. A recirculation zone is apparent due to the effect of heat transfer in the area.

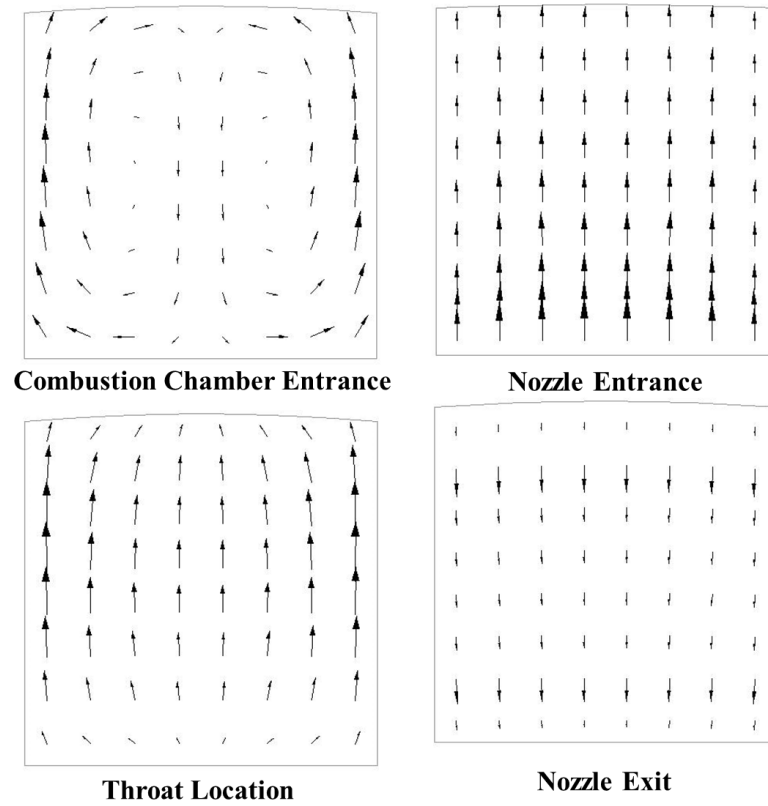


Figure 62: Dean Vortices in base model A

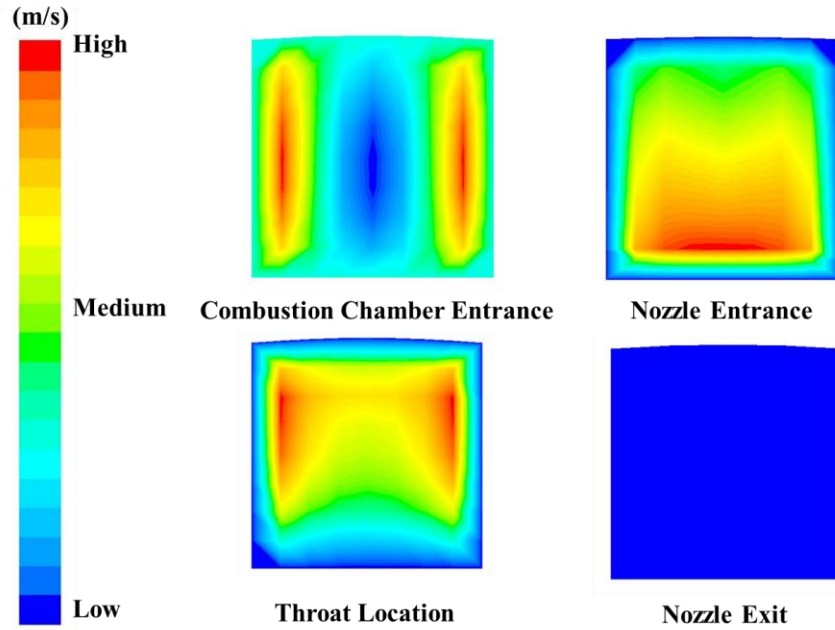


Figure 63: Radial velocity contours for base model A

Figures 64-66 present the convective heat transfer coefficient for the cases studied. These plots were generated through Newton's law of cooling, where the local channel heat flux, bulk temperature and wall temperatures were used to find parameter h . A general trend observed in the figures is the uneven and curved appearance of the plots due to the combined effect of Dean Vortices and thermal stratification. In all figures, a sharp and sudden decrease of the convective coefficient is observed immediately to the left of the nozzle throat. This decrease is theorized to be directly related to the change of direction of radial velocities in the area due to the curvature. This change in direction can be seen in Figure 67, where radial velocity magnitudes are seen to be negative in the diverging section with an immediate change to positive in the converging portion. A gradual increase of this value is observed at the converging section, where the combined effects of buoyancy and centripetal forces allow for a rapid mixing of the flow and enhanced heat transfer characteristics. The sharp decrease observed at the end of the combustion chamber region is thought to be due to the dissipation of the Dean vortices in the straight combustor section. A steady increase of the convective coefficient is seen from the combustion chamber region to the exit of the channels. The enhanced convective coefficient is due to an increased channel bulk temperature

in the area stemming from thermal stratification effects. A positive effect of this recirculation phenomenon can be seen in the figures in the axial locations between .1 and .2 m, where there is a slight curvature in the geometry. Upon comparing the numerical values to the analytical predictions, it is apparent that the analytical estimates through the Sieder-Tate correlation over predict the numerical values in the nozzle region; this implies that a safety factor must be implemented when calculating overall coolant velocity. The comparison of channel aspect ratios shown in Figure 64 indicate that a decrease in the aspect ratio will result in an increased convective coefficient in the combustion chamber area. In the nozzle areas, cases A and C present similar performances. Data points for Case B (AR 1.25) indicate that the convective coefficient values will show significant degradation in high aspect ratio configurations. A comparison of hydraulic diameters (Figure 65) indicates that the smallest configuration will result in the largest convective heat transfer coefficient. Figure 66 shows a clear trend between the number of channels and the cooling performance: a lower number of channels will result in a higher coolant convective heat transfer coefficient due to increased coolant wall temperatures. This trend is unaffected by axial coordinate parameters, as the difference between models is steady throughout the combustor length.

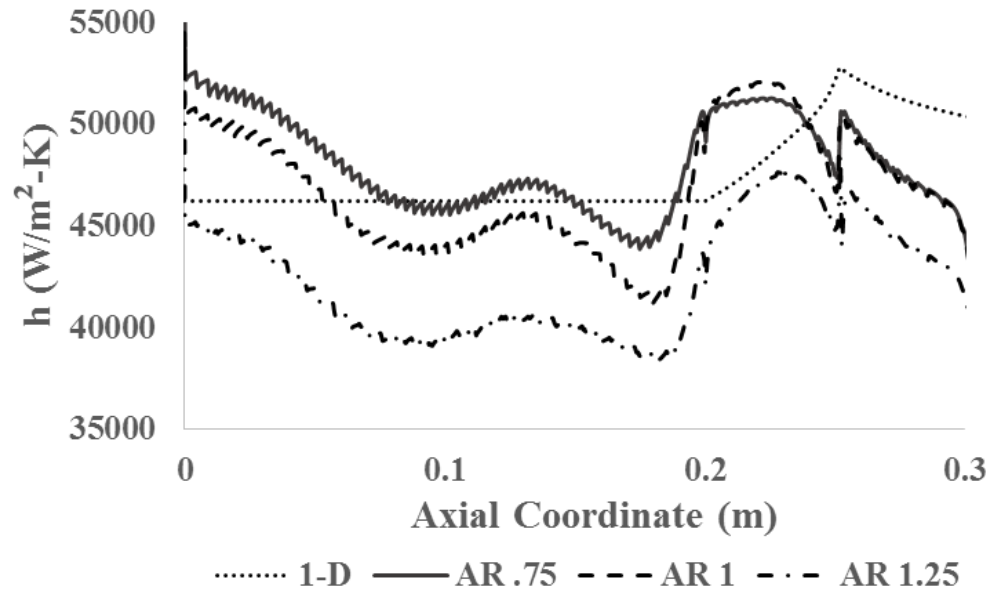


Figure 64: Convective heat transfer coefficient comparison (Aspect ratio)

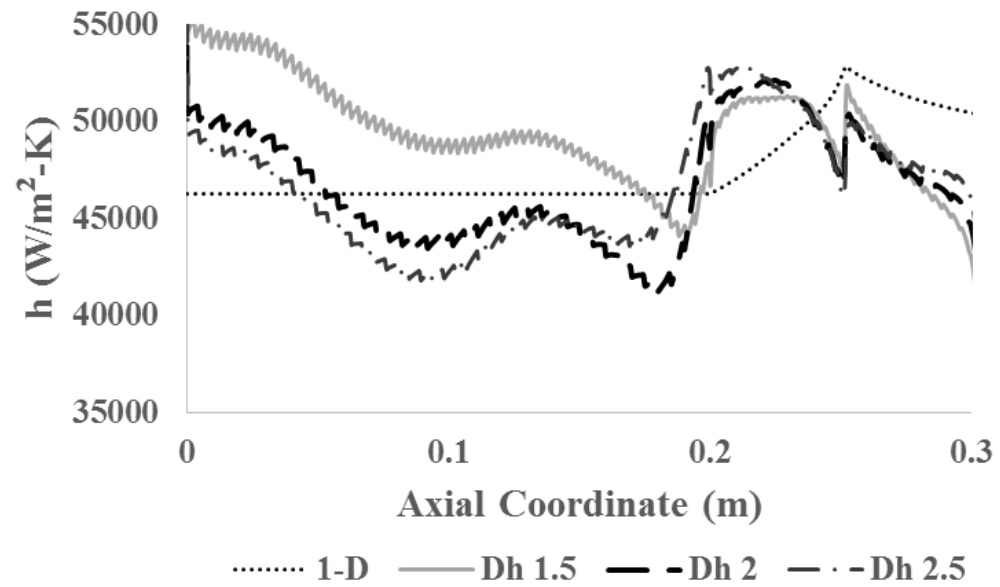


Figure 65: Convective heat transfer coefficient comparison (Hydraulic diameter)

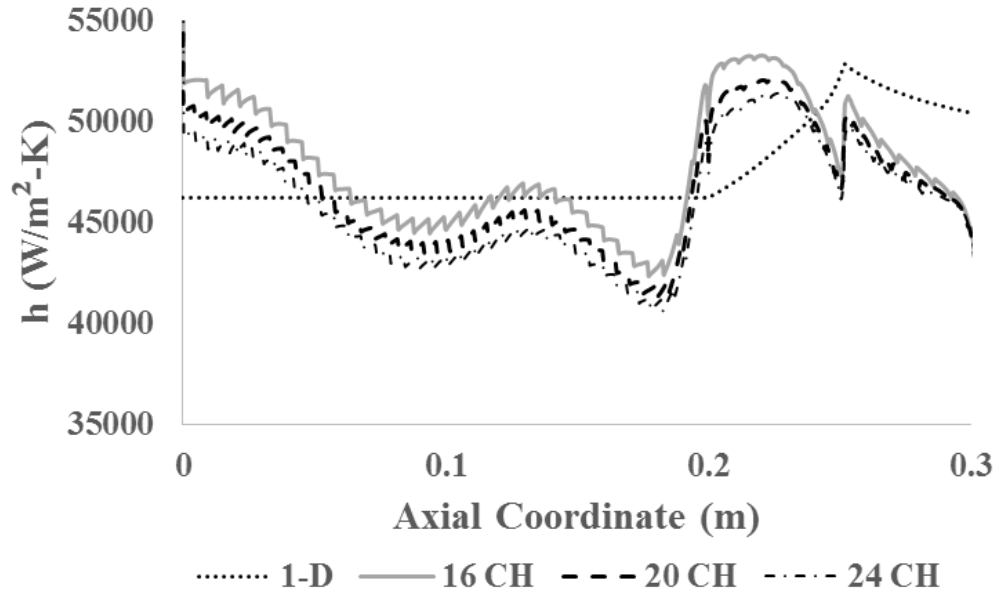


Figure 66: Convective heat transfer coefficient comparison (Channel number)

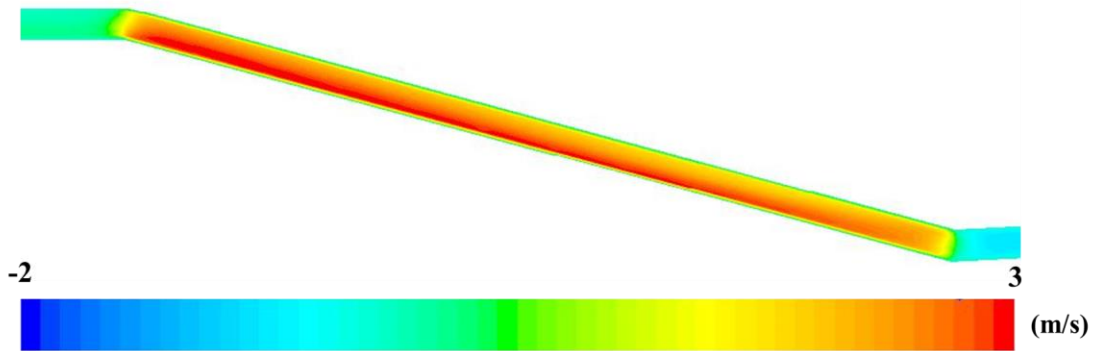


Figure 67: Detailed view of radial velocity contours

A three-dimensional numerical study performed by Pizzarelli et al [54] on hydrogen-cooled rockets showed that heat transfer in curved channels is enhanced when compared to a straight configuration, independent of the orientation of the curvature. A perturbation of the thermal stratification effect arises from the Dean vortices, which enhance mixing between the high and low-density fluids. A counterflow channel configuration was investigated and compared to a co-flow configuration in the study. Radial velocity vectors in this investigation were seen to match what was shown in Figure 62 for a concave-convex curvature setting. A comparison of the observed trends in convective heat transfer coefficients shows that there is a slight performance

reduction in the model where Dean Vortices change direction; both cases are displayed in Figure 68. While counterflow case a) shows only a slight decrease in performance for locations $s=20-25$ cm, the current configuration displays a sharp reduction at $x=.25$ m. This sharp reduction may be due to the increased viscosity of water over that of hydrogen, diminishing overall velocities with the curvature change.

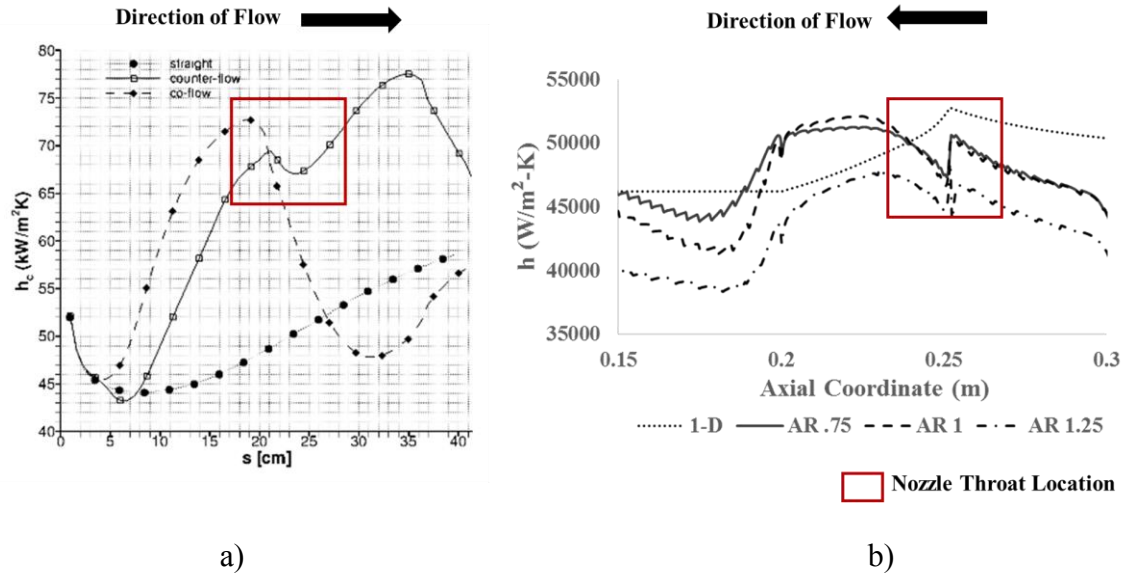


Figure 68: Case comparison between a) Pizzarelli et. al [54] and b) current configuration

As described in Section 6.2, predictions of fin base temperature were estimated analytically according to the estimate of channel temperatures. Numerical fin base temperatures were extracted at the midline of the fin, at a radial coordinate of 1 mm from the inner wall. It is apparent from Figures 69-71 that the analytical prediction of fin base temperature grossly underestimates their maximum value according to the numerical simulation. The trends seen in these figures show a sharp decrease of fin temperatures at the end of the combustion chamber. This decrease is due to the increased effect of the bottom-channel convection vs. the fin effect, lowering overall temperatures. The increased fin base thicknesses in models C (AR 1.25) and F (16 channels) result in larger fin base temperatures when compared to their respective counterparts. Though fin base thicknesses remain the same when comparing hydraulic diameters, an increase in this value is seen

to have a growth in the base temperature. This is directly related to Figure 55, where it was shown that case E had the largest angular temperature gradient for its respective parametric study.

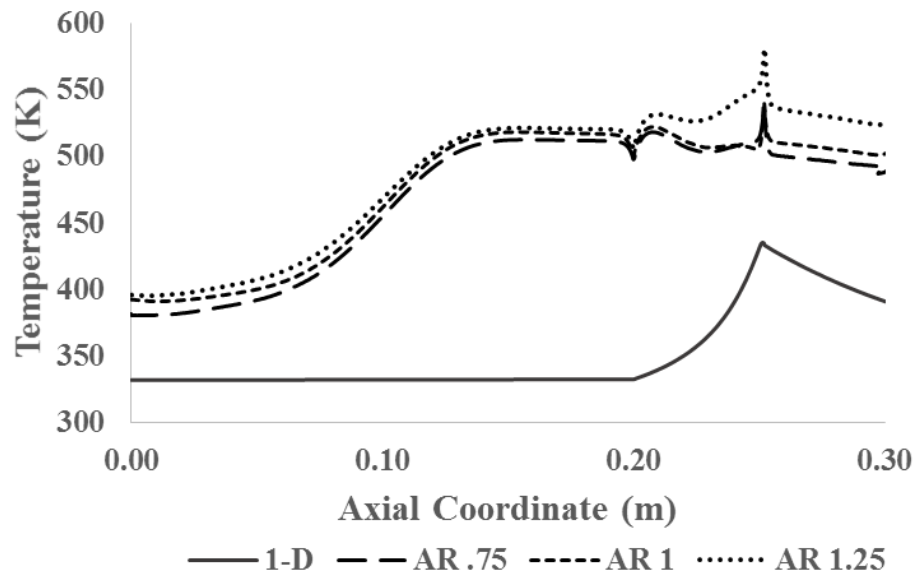


Figure 69: Fin base temperature comparison (Aspect ratio)

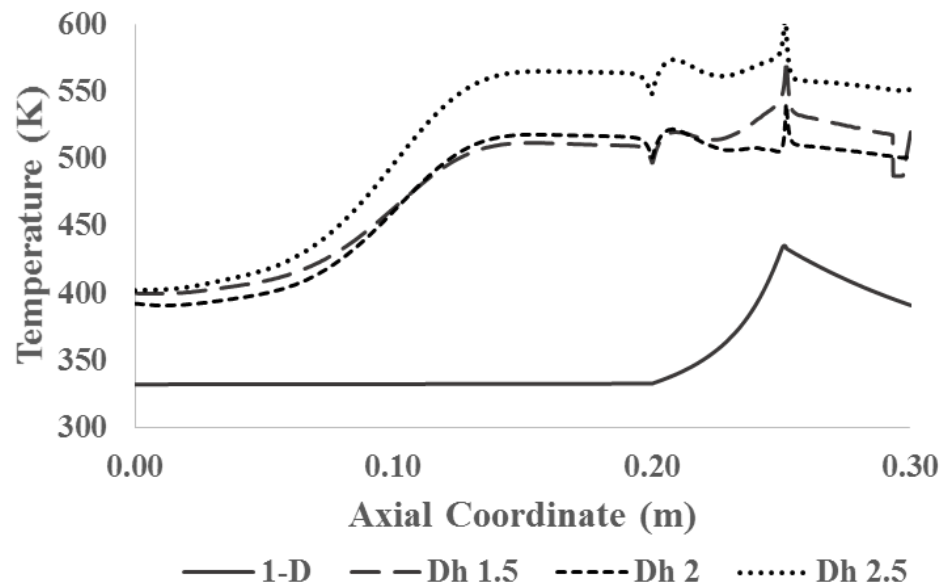


Figure 70: Fin base temperature comparison (Hydraulic diameter)

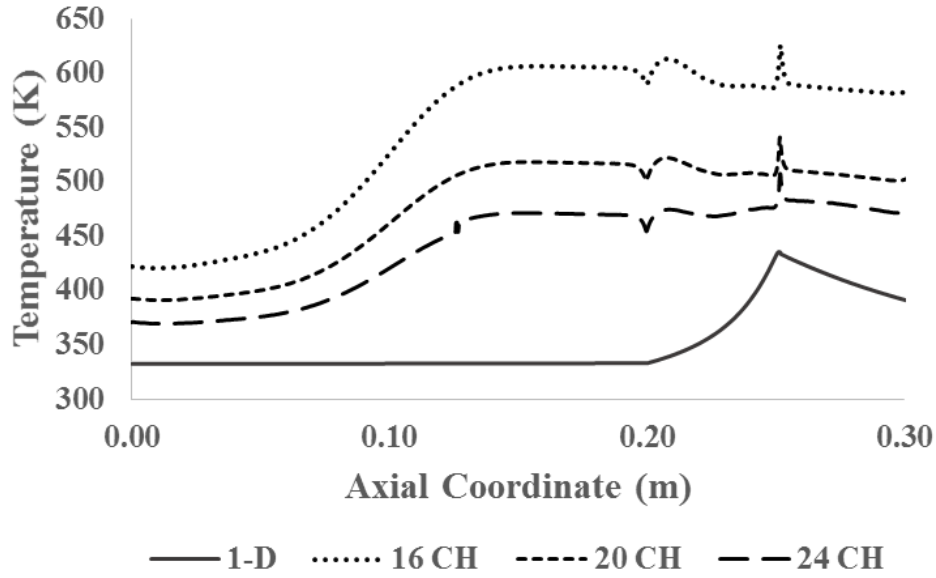


Figure 71: Fin base temperature comparison (Channel number)

Fin stratification effects at the axial throat location are compared in Figure 72. Similar to what has been observed in Figures 57-61, solid stratification appears to be proportional to the degree of coolant stratification when comparing aspect ratios (Models A, B, C). A comparison of hydraulic diameters (Models A, D, E) reveals large amounts of solid stratification in the case of model D, where the fin tip has an approximate temperature of 400 K.

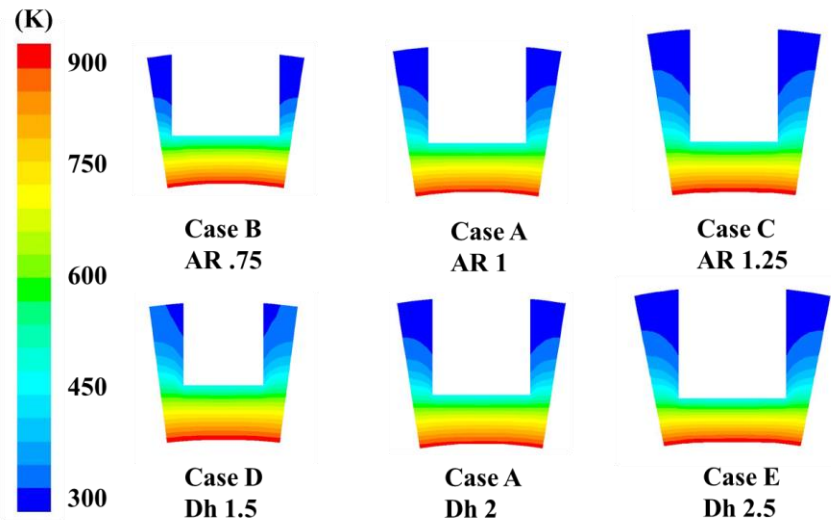


Figure 72: Fin temperature stratification, comparison at throat

Computational throat efficiency was evaluated through the averaging of heat flux at the sides of the fin for the axial throat location. An approximate local efficiency was calculated through equation 52, shown below. The results of the models evaluated are shown in Table 15. A comparison of the efficiency values shows that the largest discrepancy between analytical and numerical models occurs in model C, corresponding to an aspect ratio of 1.25. This is largely due to the difference between the numerical fin base temperature and the assumed analytical value. Overall, the evaluation of the 1-D efficiency through the analytical method described in section 6.2 resulted in acceptable accuracies when compared to the numerical method.

$$\eta = \frac{q_{fin,sides}}{h_{bulk}(T_{fin,base} - T_{bulk})} \quad [52]$$

Table 16: Local efficiency comparison of channels

	A	B	C	D	E	F	G
1-D	16.4%	14.4%	16.8%	23%	15.24%	23.11%	11.34%
Numerical	19.72%	15.28%	23.80%	23.08%	18.44%	28.45%	12.27%
Difference	3.32%	.88%	7%	.08%	3.2%	5.34%	.93%

6.3.3 Mesh Independence Results

A mesh independence study was carried out to validate the methods in the periodic numerical simulation. The channel centerline velocity was plotted for a coarse (95,000 elements), medium (185,000 elements) and fine (300,000 elements) mesh configuration. Figure 73 presents a plot of these values. While the meshes were been scaled up in relatively steady increments, the medium-fine mesh comparison shows a larger value gap than the coarse-medium comparison. In all mesh iterations and axial locations, values of velocity were not seen to vary more than 1 meter per second.

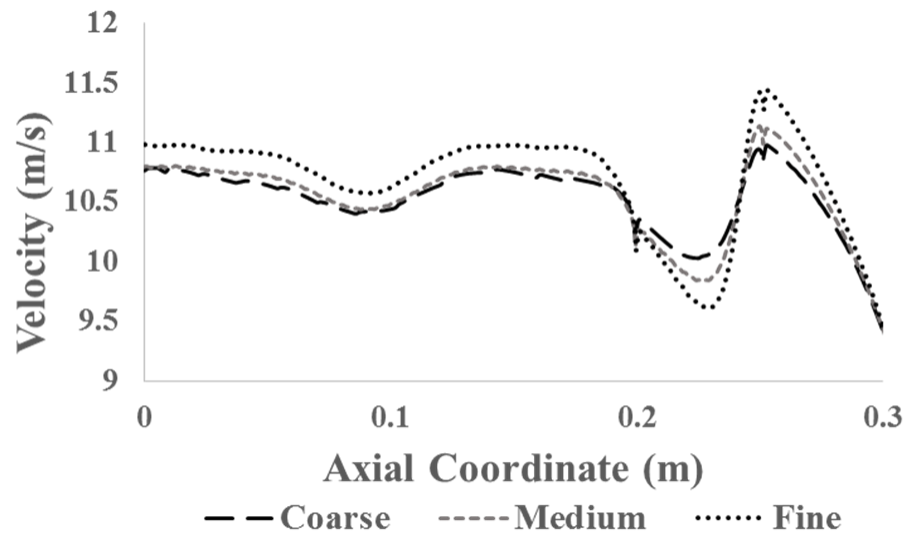


Figure 73: Comparisons of midline channel velocity

Chapter 7: Summary and Future Work

The integration of oxy-fuel flames in power generation techniques has been identified as a potential method to enhance fossil-fuel based technologies, reducing overall emissions and improving efficiencies in existing power generation systems. While its application is constrained by material limitations, open-cycle magnetohydrodynamic (MHD) combustors have the potential to fully utilize the energy of undiluted flames. An MHD direct power extraction unit produces electricity based on Faraday's law of induction, generating current through the interaction of a conductor and a magnetic field. This type of system possesses no moving parts, directly converting thermal energy to electrical energy and allowing for a higher overall working temperature. Studies have shown that the inclusion of an MHD device as a topping cycle may exceed the efficiencies of those seen in existing power plants by as much as 20%. Though research on open-cycle MHD combustors has seen a sharp decline since the 1990s, the possible integration of oxy-fuel combustion has triggered renewed interest in the use of the technology. As operation at temperatures exceeding 3000 K presents a challenge, the design of a steady-state MHD combustor requires the inclusion of a highly effective cooling mechanism. A literature review on the cooling of similar environments revealed that most techniques employ semi-empirical 1-D approaches with implied inaccuracies. In addition to this, limited data exists on the use of MHD open-cycle generators burning in the presence of oxygen with no additional diluents. This work presents design and modeling methodologies on MHD direct power extraction systems capable of operating at near-stoichiometric conditions. A proof-of-concept 60 kW_{th} model of an MHD combustor was designed in accordance to rocket engine theories. This model employed a combination of gaseous methane and oxygen at near-stoichiometric conditions. The principal requirements of this engine were set at an exit gas temperature of 2800 K and a velocity of 2000 m/s. These requirements have

been determined from literature: the working fluid's electrical conductivity has been shown to increase by a factor of T^{10} , while potential power output is related to the square of the gas velocity. This combustor was manufactured using Inconel 718, a superalloy chosen due to its high melting point and strength characteristics in extreme environments. The design of this geometry was carried out through the assumption of isentropic expansion and a flame temperature of 3315 K. Heat transfer in the combustor models was described through the use of the Bartz correlation for nozzles in a thermal resistance model. The techniques employed in the design of the MHD combustor were characterized through a computational fluid dynamics (CFD) model, with comparisons being drawn to experimental results. The numerical simulation coupled the combustion, solid and fluid domains in a single 2-D axisymmetric model. The solution of the combustor domain was shown to vary by less than 5% when compared to isentropic flow equations. Gas exit velocity was estimated to be 2018 m/s, with exit temperature corresponding to 2759 K. Reductions in the numerical values are thought to be the product of boundary layer prediction and viscous losses. Numerical estimates of heat flux showed that the model presents a value 40% lower than the analytical calculation performed through the Bartz equation. The accuracy of this correlation was found to be impacted by inlet conditions of the flow and boundary layer thickness according to literature [44]. A reduction of this value was proposed for its future implementation in nozzle cooling systems with chamber pressures below 1.4 MPa. The modified analytical temperature estimates were shown to predict surface temperature values to within 3 K when compared to experimental values. A comparison between numerical and experimental results showed similar accuracies, with deviations attributed to the effects of curvature and stratification. While the coupled resolution of pressure and momentum equations enhances accuracy, the use of an analytical model by assuming a reduction in the Bartz correlation effectively provides an

estimate of heat flux parameters and wall temperatures. Due to its successful experimental implementation and the validity of the numerical method, the techniques employed in the proof-of-concept study were retained in the development of the scaled prototype.

A thorough scaling procedure is necessary when developing DPE device technologies to full commercial implementation. Reports on MHD literature have suggested that a research gap exists in the improvement of oxy-based open-cycle combustors. In addition to this, there is a lack of data on the scaling characterization of models employing near-stoichiometric oxy-methane flames. The development of non-dimensional scaling parameters may lead to reduced production costs and lead times in similar systems. A scaling methodology was proposed in the development of a 1-MW combustor. Baseline gaseous exit temperature and velocity parameters mimicked those of the proof-of-concept model. Scaling parameters were determined from critical design criteria in rocket literature [32]. The combustion reaction was maintained by conserving the oxidizer and fuel combination at the same pressure and mixture conditions. Injector geometries were developed using a photo-scaled method and a constant momentum flux ratio (MFR). Orifice diameters were dictated by a 20% pressure drop requirement. While this method implies a change of the Reynolds number, empirical data has suggested a reduction in possible instabilities. A transition region based on a 5th order polynomial [59] was implemented to expand oxidizer inlet diameter to that of the chamber. The cooling system of the scaled combustor was based on the methodology employed in the POC, with the required coolant convective parameters equaling those of the first design.

The 1-MW combustor prototype was manufactured through additive manufacturing (AM) methods employing selective laser melting (SLM). The inclusion of this technology allowed for a reduced manufacturing time and increased design freedoms, with minimal changes in the material's high temperature characteristics. In addition to a pressure sensing conduit and multiple

ignition locations, the design of this prototype includes .8-mm thermocouple conduits embedded into the channel fins. While the model displayed a relatively high surface roughness, the AM method was shown to effectively replicate these small-scale features with a relatively low shrinkage. Radial and axial warping were seen in the combustor's cooling jacket shells due to the accumulation of thermal stresses; no such defects were observed in the main combustor section. A dimensional measurement on the built prototypes revealed measurement disparities of less than 4% in the main combustor, with those in the shells averaging a difference of 10% or more.

Coolant manifold configurations and cross-sectional channel geometries were investigated through numerical and analytical methods. This analysis was performed to ensure steady-state combustor operating parameters and quantify the effect of a three-dimensional geometry. The use of numerical methods is crucial in large-scale engines, where coolant temperature profiles may differ significantly from POC models. Parametric studies regarding the manifold and individual channel geometry were performed and related to fin efficiency. To optimize element number and increase mesh quality, periodic models were employed in both simulations.

A study on manifold optimization presented a correlation between entering tube velocities and cavitation-prone areas. Though a reduced cavitation risk was associated with smaller tube diameters, these cases presented a strong asymmetry in channel mass flow distribution. This was considered to be a critical factor in the model. Cases implementing increased manifold lengths and tube inlets were shown to display equal values of flow amongst the channels. A case resulting in low theoretical pressure drops, a moderate cavitation risk and an even flow distribution was implemented in the design of the 1-MW model. A chamfer was introduced to the design in an attempt to mitigate the high-temperature portions present in sharp edges.

An analytical estimate of fin efficiency was developed to assess performance and establish a comparison to the 3-D channel model. Fin thermal conductivity, local base temperatures and base thickness were shown to influence efficiency values regardless of channel geometry. This results in a variation of optimal aspect ratio throughout the nozzle. Fins corresponding to low channel aspect ratios were observed to perform optimally in regions of low thermal conductivity due to their reduced overall lengths. As a general trend, fin efficiency was seen to decrease at the throat, following the trend set by base temperatures. Inverse proportionalities with fin efficiency were found in the channel hydraulic diameter and number of channels. While fin parameters may be optimized for a certain point, parameters affecting this value are rapidly changing throughout nozzle contours. A fin efficiency analysis must be coupled with a study on channel stratification to both minimize solid wall temperatures and maximize the fin effect.

A three-dimensional model was developed to capture the effect of variable coolant properties on the combustor walls. All models compared were designed to provide a theoretically equal performance according to the Sieder-Tate correlation. Results from the initial numerical model were implemented in the form of a convective boundary condition based on the reduced Bartz correlation.

It was found that the analytical estimates of the Sieder-Tate correlation overpredict convective heat transfer coefficient when compared to numerical values. In addition to this, results from the numerical model show that the analytical estimate falls short when estimating wall temperatures. These results imply that pressure and velocity safety factors must be implemented when operating the system. While large differences were observed in estimates of fin base temperature, inner wall 1-D temperatures closely resembled the developed numerical models. A variation of analytical and numerical fin base temperatures resulted in increased fin efficiencies

for higher-temperature models. While the differences among models varied from .08% to 7%, the analytical efficiencies were considered to be acceptable as a design base point.

An analysis on hydraulic diameter variations showed increased channel bottom temperatures when decreasing cross-sectional geometry. However, when comparing inner wall temperatures, the base case displayed the lowest values. Inner temperatures were shown to be affected by both stratification levels and fin efficiency. When optimizing aspect ratios, an equilibrium must be reached between both values. A comparison between channel number with a steady hydraulic diameter showed that a decrease in this value results in increased cavitation risks and inner wall temperatures. Though the 24-channel configuration presented the lowest overall temperatures of all models, this configuration overestimates the 1-D approximations by more than 40 K. While an increase in the number of channels results in decreased temperatures, it also ensues in decreased structural supports and larger pump power requirements. The comparison of aspect ratios shows that while channel bottom temperatures are not significantly affected, the base aspect ratio results in the lowest combustion-side wall temperatures.

An analysis of radial velocities at different locations in the geometry was conducted to identify the presence of Dean Vortices. Radial velocity was seen to change directions according to the path of curvature. This change had a significant effect in the local convective heat transfer coefficient, reflected as a sharp and sudden decrease observed to the left of the nozzle. A literature study on H₂-cooled rockets [54] was seen to exhibit a similar trend in a reduced manner.

7.1 Next steps/Considerations

Further evaluations of diverse cooling channel configurations (e.g. bifurcated, angled) must be performed to quantify differences in geometry. The numerical findings expressed in this work may be used to improve a particular channel geometry for diverse axial locations. Cooling channels may be optimized to minimize pressure drop through a variation of hydraulic diameters, increasing wall temperature in non-critical regions and decreasing cavitation risks in the nozzle. This would also increase the overall efficiency through a minimization of heat loss. Though this may pose a challenge for traditional methods, AM methods may be employed to manufacture and investigate these geometries. The overall results of the models developed indicate that the implementation of oxy-combustion may be feasible in future DPE applications. The experimental performance of the proof-of-concept 60 kW device demonstrates potential in next-generation power applications. The 1-MW MHD combustor prototype must be tested in similar conditions to those employed in the 60-kW investigation to characterize the wall's thermal profile and determine the validity of the cooling system modeling. The findings made in this investigation must be analyzed to determine the reliability of the design methods and characterize scaling criteria. The development of a reliable scaling technique may lead to a rapid growth of oxy-fuel combustor technology. A combination of numerical and experimental studies incorporating seeding may be performed on the POC and 1-MW models. While these prototypes may be modified to include a seeding port, the possibility of injection in the oxidizer region must be investigated. The efficiency of the models and their potential power extraction must be experimentally characterized to determine their feasibility as a topping cycle component in power generation applications. Once models have been executed at the pilot and commercial scales, the implementation of this technology could result in a drastic increase of efficiencies and reduction of emissions.

References

- [1] Environmental Protection Agency, "US Greenhouse Gas Inventory Report: 1990-2014," Environmental Protection Agency, 2016. [Online]. Available: <http://www.epa.gov/climatechange/ghgemissions/usinventoryreport.html>.
- [2] A. A. Chowdhury, L. Bugarin, A. Badhan, A. Choudhuri and N. Love, "Thermodynamic analysis of a directly heated oxyfuel supercritical power system," *Applied Energy*, vol. 179, pp. 261-271, 2016.
- [3] C. Kunze and H. Spliethoff, "Assessment of oxy-fuel, pre- and post-combustion-based carbon capture," *Applied Energy*, no. 94, pp. 109-116, 2012.
- [4] N. Kayukawa, "Open-cycle magnetohydrodynamic electrical power generation: a review and future perspectives," *Energy and Combustion Science*, vol. 30, no. 1, pp. 33-60, 2004.
- [5] N. Kayukawa and Y. Wang, "Advanced Coal Power Cycle with a Stand-Alone Magnetohydrodynamic Generator," *Journal of Propulsion and Power*, vol. 20, no. 3, pp. 566-571, 2004.
- [6] M. Petrick and B. Shumyatsky, "Open-cycle magnetohydrodynamic electrical power generation. Technical and economic aspects of open-cycle MHD Power Plants," Nauka, Moscow and Argonne NL: Joint US-USSR Publication, 1978.
- [7] A. O. Ayeleso and M. T. Kahn, "Modelling of a combustible ionised gas in thermal power plants using MHD conversion system in South Africa," *Journal of King Saud University-Science*, 2017.
- [8] V. R. Malghan, "History of MHD Power Plant Development," *Energy Corners: Mgmt*, vol. 37, no. 5, p. 1996, 569-590.
- [9] S. Way, S. M. DeCorso, R. L. Hundstat and G. A. Kemeny, "Experiments With MHD Power," *ASME J. Eng Power*, vol. 83, no. 4, pp. 397-408, 1961.
- [10] L. Proskuryakova and A. Kovalev, "Measuring energy efficiency: is energy intensity a good evidence base?," *Applied Energy*, no. 138, pp. 450-459, 2015.
- [11] S. Aithal, "Analysis of Optimum Power Extraction in a MHD Generator with Spatially Varying Electrical Conductivity," *International Journal of Thermal Sciences*, vol. 47, no. 8, pp. 1107-1112, 2008.
- [12] M. Ishikwa, M. Yuhara and T. Fujino, "Three-Dimensional Computation of Magnetohydrodynamics in Weakly Ionized Plasma with strong MHD interaction," *Journal of Materials Processing Technology*, vol. 181, no. 1-3, pp. 254-259, 2007.
- [13] B. Bhadoria and A. Chandra, "Transient Analysis of Proposed Indian MHD Channel," *Energy Conversion and Management*, vol. 42, no. 8, pp. 963-966, 2001.
- [14] M. Wolfendale and M. J. Bluck, "A Coupled Systems Code-CFD MHD Solver for Fusion Blanket Design," *Fusion Engineering and Design*, Vols. 98-99, pp. 1902-1906, 2015.
- [15] W. D. Jackson, R. A. Lawit, M. G. Klett, J. C. Cutting and C. D. Maxwell, "Status of the reference dual cycle MHD-steam power plant," in *Proceedings of the 16th SEAM*, Pittsburgh, 1977.

- [16] Y. Hu, J. Yan and H. Li, "Effects of flue gas recycle on oxy-coal power generation systems," *Applied Energy*, vol. 97, pp. 255-263, 2012.
- [17] C. Y. Liu, G. Chen, N. Sipöcz, M. Assadi and X. S. Bai, "Characteristics of oxy-fuel combustion in gas turbines," *Applied Energy*, vol. 89, no. 1, pp. 387-394, 2012.
- [18] M. Pizzarelli, B. Betti and F. Nasuti, "Coupled analysis of hot-gas and coolant flows in LOX/methane thrust chambers," in *4th European Conference for Aerospace Sciences*, 2011.
- [19] T.-S. Wang and V. Luong, "Hot-Gas-Side and Coolant-Side Heat Transfer in Liquid Rocket Engine Combustors," *Journal of Thermophysics and Heat Transfer*, vol. 8, no. 3, pp. 524-530, 1994.
- [20] M. Pizzarelli, F. Nasuti, R. Paciorri and M. Onofri, "Numerical Analysis of Three-Dimensional Flow of Supercritical Fluid in Cooling Channels," *AIAA Journal*, vol. 47, no. 11, pp. 2534-2543, 2009.
- [21] C. H. Marchi, F. Laroca, A. F. Carvalho da Silva and J. N. Hinckel, "Numerical Solutions of Flows in Rocket Engines with Regenerative Cooling," *Numerical Heat Transfer, Part A*, vol. 45, no. 7, pp. 699-717, 2004.
- [22] S.-K. Kim, M. Joh, H. S. Choi and T. S. Park, "Effective Modeling of Conjugate Heat Transfer and Hydraulics for the Regenerative Cooling Design of Kerosene Rocket Engines," *Numerical Heat Transfer, Part A: Applications*, vol. 66, no. 8, pp. 863-883, 2014.
- [23] S.-K. Kim, M. Joh, H. S. Choi and T. S. Park, "Multidisciplinary simulation of a regeneratively cooled thrust chamber of liquid rocket engine: Turbulent combustion and nozzle flow," *International Journal of Heat and Mass Transfer*, vol. 70, pp. 1066-1077, 2014.
- [24] H. W. Zhang, Y. L. He and W. Q. Tao, "Numerical study of film and regenerative cooling in a thrust chamber at high pressure," *Numerical Heat Transfer, Part A*, vol. 52, no. 11, pp. 991-1007, 2007.
- [25] M. Pizzarelli, F. Nasuti and M. Onofri, "Coupled Numerical Simulation of Wall Heat Conduction and Coolant Flow in Liquid Rocket Engines," *Journal of Propulsion and Power*, vol. 29, no. 1, pp. 34-41, 2012.
- [26] M. Pizzarelli, F. Nasuti and M. Onofri, "Coupled Wall Heat Conduction and Coolant Flow Analysis for Liquid Rocket Engines," *Journal of Propulsion and Power*, vol. 29, no. 1, pp. 34-41, 2013.
- [27] M. Pizzarelli, F. Nasuti and M. Onofri, "Coupled Numerical Simulation of Wall Heat Conduction and Coolant Flow in Liquid Rocket Engines," in *47th AIAA/ASME/SAE/ASEE Joint Propulsion Conference & Exhibit*, San Diego, California, 2011.
- [28] S. Gu, C. Eastwick, K. Simmons and D. McCartney, "Computational Fluid Dynamic Modeling of Gas Flow Characteristics in a High-Velocity Oxy-Fuel Thermal Spray System," *Journal of Thermal Spray Technology*, vol. 10, no. 3, pp. 461-469, 2001.
- [29] H. Tabbara and S. Gu, "Computational simulation of liquid-fuelled HVOF thermal spraying," *Surface & Coatings Technology*, vol. 204, no. 5, pp. 676-684, 2009.

- [30] M. Li and P. D. Christofides, "Multi-scale modeling and analysis of an industrial HVOF thermal spray process," *Chemical Engineering Science*, vol. 60, no. 13, pp. 3649-3669, 2005.
- [31] H. Katanoda, T. Tachibanaki, J. Kawakita, S. Kuroda and M. Fukuhara, "Mathematical Modeling and Experimental Validation of the Warm Spray (Two-Stage HVOF) Process," *Journal of Thermal Spray Technology*, vol. 18, no. 3, pp. 401-409, 2008.
- [32] D. Huzel and D. Huang, *Modern Engineering for Design of Liquid Propellant Rocket Engines (Progress in Astronautics and Aeronautics)*, Washington D.C.: American Institute of Aeronautics and Astronautics, 1992.
- [33] S. M. Ferdous, E. Ghani, M. Rezaul Hasan, W. Bin Khaled and M. Nayeemul Hasan, "An Overview of Technical and Economical Feasibility of Retrofitted MHD Power Plants from the Perspective of Bangladesh," *Cyber Journals: Multidisciplinary Journals and Technology, Journal of Selected Areas in Renewable and Sustainable Energy (JRSE)*, 2011.
- [34] P. G. Hill and C. R. Peterson, *Mechanics and Thermodynamics of Propulsion*, Addison Wesley, 1992.
- [35] A. Krishnan and B. Jinshah, "Magnetohydrodynamic Power Generator," *International Journal of Scientific and Research Publications*, vol. 3, no. 16, 2013.
- [36] J. Marlin Smith and L. Nichols, "Estimates of Optimal operating conditions for hydrogen-oxygen cesium-seeded magnetohydrodynamic power generator," NASA Lewis Research center , Cleveland, 1977.
- [37] M. Pizzarelli, M. Carapellese and F. Nasuti, "A Quasi-2-D Model for the Prediction of the Wall Temperature of Rocket Engine Cooling Channels," *Numerical Heat Transfer, Part A: Applications*, vol. 60, no. 1, pp. 1-24, 2011.
- [38] T. L. Connell, S. A. Santi, G. A. Risha and B. A. Muller, "Experiment and semi-empirical modeling of lab-scale hybrid rocket performance," in *45th Joint propulsion conference & exhibit*, Denver, 2009.
- [39] S. Gordon and B. J. McBride, "Computer Program for Calculation of Complex Chemical Equilibrium Compositions and Applications, part 1: analysis," National Aeronautics and Space Administration, Cleveland, 1994.
- [40] ANSYS, "Modeling Non-Premixed Combustion (ANSYS Fluent Theory Guide)," ANSYS Inc. , Canonsburg, 2013.
- [41] ANSYS, Inc., *ANSYS Fluent Theory Guide - 4.12.2 Standard Wall Functions*, Canonsburg: ANSYS, Inc., 2009.
- [42] A. Neale, D. Derome, B. Blocken and J. Carmeliet, "CFD calculation of convective heat transfer coefficients and validation – Part 2: Turbulent flow," in *Annex 41*, Kyoto, 2006.
- [43] J. M. Smith and L. D. Nichols, "Estimates of Optimal Operating Conditions for Hydrogen-Oxygen Cesium-Seeded Magnetohydrodynamic Power Generator," NASA, 1977.
- [44] D. R. Bartz, "Turbulent boundary-layer heat transfer from rapidly accelerating flow of rocket combustion cases and of heated air," Jet Propulsion Laboratory, Pasadena, 1965.
- [45] W. E. Welsh and A. B. Witte, "A comparison of analytical and experimental local heat fluxes in liquid-propellant rocket thrust chambers," *Journal of heat transfer*, vol. 84, no. 1, pp. 19-28, 1962.

- [46] L. H. Back, P. F. Massier and H. L. Gier, "Convective Heat Transfer in a Convergent Divergent Nozzle," Jet Propulsion Laboratory, Pasadena, 1964.
- [47] J. J. Kolozsi, *An investigation of heat transfer through the turbulent boundary-layer in an axially symmetric converging-diverging nozzle*, Columbus: Ohio State University, 1958.
- [48] D. M. Smith, *A comparison of experimental heat-transfer coefficients in a nozzle with analytical predictions*, Raleigh: North Carolina State University at Raleigh, 1970.
- [49] R. A. Ahmad, "Discharge coefficients and heat transfer for axisymmetric supersonic nozzles," *Heat Transfer Engineering*, vol. 6, no. 22, pp. 40-61, 2001.
- [50] K. J. Kacynski, "Thermal Stratification Potential in Rocket Engine Coolant Channels," NASA Lewis Research Center, Cleveland, 1992.
- [51] M. Pizzarelli, F. Nasuti and M. Onofri, "A simplified model for the analysis of thermal stratification in cooling channels," in *2nd european conference for aerospace sciences*, Brussels, 2007.
- [52] A. V. Kalpakli, "Vortices in turbulent curved pipe flow-rocking, rolling and pulsating motions," Royal Institute of Technology KTH Mechanics, Stockholm, 2014.
- [53] Y. Torres, L. Stefanini and D. Suslov, "Influence of curvature in regenerative cooling system of a rocket engine," *Progress in Propulsion Physics*, vol. 1, pp. 171-184, 2009.
- [54] M. Pizzarelli, F. Nasuti and M. Onofri, "CFD Analysis of Curved Cooling Channel Flow and Heat Transfer in Rocket Engines," in *46th AIAA/ASME/SAE/ASEE Joint Propulsion Conference & Exhibit*, Nashville, 2010.
- [55] P. M. Shumyatsky, "U.S./U.S.S.R. Cooperative program in open-cycle MHD electrical power generation," Argonne, 1978.
- [56] J. R. Hulka, "Scaling of Performance in Liquid Propellant Rocket Engine Combustion Devices," in *44th AIAA/ASME/SAE/ASEE Joint Propulsion Conference & Exhibit, Joint Propulsion Conferences*, Hartford, 2008.
- [57] W. Xiao-Wei, C. Guo-Biao and G. Yu-Shan, "Scaling of heat transfer in a gas-gas injector combustor," *Chinese Physics B*, vol. 20, no. 6, 2011.
- [58] S. S. Penner, "On the Development of Rational Scaling Procedures for Liquid-Fuel Rocket Engines," *Journal of Jet Propulsion*, vol. 27, no. 2, pp. 156-161, 1957.
- [59] M. Subramanya, D. S. Davu and A. Choudhuri, "Experimental Investigation on the Flame Extinction Limit of Fuel Blends," in *43rd AIAA Aerospace Sciences Meeting and Exhibit*, El Paso, 2005.
- [60] B. M. Lovich, "Design of a 1 Megawatt Heat Input Direct Power Extraction System for Advanced Topping Cycles," The University of Texas at El Paso, El Paso, 2017.
- [61] T. Trosch, J. Strobner, R. Volkl and U. Glatzel, "Microstructure and mechanical properties of selective laser melted Inconel 718 compared to forging and casting," *Materials Letters*, vol. 164, pp. 428-431, 2016.
- [62] Q. Jia and D. Gu, "Selective laser melting additive manufactured Inconel 718 superalloy parts: High-temperature oxidation property and its mechanisms," *Optics & Laser Technology*, vol. 62, pp. 161-171, 2014.
- [63] S. C. Joshi and A. A. Sheikh, "3D printing in aerospace and its long-term sustainability," *Virtual and Physical Prototyping*, vol. 10, no. 4, pp. 175-185, 2015.

- [64] B. Song, X. Zhao, S. Li, C. Han, Q. Wei, S. Wen, J. Liu and Y. Shi, "Differences in microstructure and properties between selective laser melting and traditional manufacturing for fabrication of metal parts: A review," *Frontiers of Mechanical Engineering*, vol. 10, no. 2, pp. 111-125, 2015.
- [65] N. Quigley and J. Evans Lyne, "Development of a Three-Dimensional Printed, Liquid-Cooled Nozzle for a Hybrid Rocket Motor," *Journal of Propulsion and Power*, vol. 30, no. 6, pp. 1726-1727, 2014.
- [66] J. M. Waller, B. H. Parker and K. L. Hodges, "Nondestructive Evaluation of Additive Manufacturing (State-of-the-Discipline Report)," NASA, 2014.
- [67] Z. Wang, K. Guan, M. Gao, X. Li, X. Chen and X. Zeng, "The microstructure and mechanical properties of deposited-IN718 by selective laser melting," *Journal of Alloys and Compounds*, vol. 513, pp. 518-523, 2012.
- [68] Y. A. Cengel, *Heat Transfer: A practical approach*, Princeton: McGraw-Hill, 1998.
- [69] D. Wang, Y. Yang, Z. Yi and X. Su, "Research on the fabricating quality optimization of the overhanging surface in SLM," *International Journal of Advanced Manufacturing Technologies*, vol. 65, pp. 1471-1484, 2013.
- [70] M. Pizzarelli, F. Nasuti and M. Onofri, "Trade-off analysis of high-aspect-ratio-cooling-channels for rockete engines," *International Journal of Heat and Fluid Flow*, vol. 44, pp. 458-467, 2013.
- [71] L. E. Schwer, "Is Your Mesh Refined Enough? Estimating Discretization Error Using GCI," Anwenderforum, 2008.
- [72] J. W. Slater, "Examining Spatial (Grid) Convergence (Public tutorial on CFD verification and validation)," NASA Glenn Research Center, Cleveland, 2008.

Appendix A: Nomenclature

a	= Channel width
A	= Area
b	= Channel height
B	= Bias error
c^*	= Characteristic velocity
C	= Constant
C_p	= Heat capacity
D	= Diameter
D_h	= Hydraulic diameter
E	= Discretization error
e	= Grid refinement ratio
er	= Relative error
f	= Mixture fraction
F	= Force
F_s	= Factor of safety
g	= Gravitational constant
G	= Generation of turbulent kinetic energy
GCI	= Grid convergence index
h	= Convective heat transfer coefficient
h_m	= Mesh discretization parameter
H	= Enthalpy
HHV	= Higher heating value
$I_{0,1}$	= Modified Bessel function of the first kind
k	= Thermal conductivity
K	= Turbulent kinetic energy

$K_{0,1}$	= Modified Bessel function of the second kind
l	= Channel depth
LHV	= Lower heating value
m	= Mass
\dot{m}	= Mass flow rate
m_f	= Fin equation constant
M	= Mach number
MFR	= Momentum Flux Ratio
N	= Heat of chemical reaction
N_c	= Number of channels
n	= Number of data points
Nu	= Nusselt number
o	= Observed rate of convergence
O/F	= Oxidizer to fuel ratio
p	= Pressure
P	= Channel perimeter
Pr	= Prandtl number
PW	= Total Power
PDF	= Probability density function
\dot{q}	= Heat flux
Q	= Heat
q	= Thickness
r	= Radial coordinate
R	= Gas Constant
R_{ct}	= Radius of curvature
R_1	= Local fin base radius
R_2	= Local fin tip radius

Re	= Reynolds number
S	= Viscous Dissipation
S_h	= Source Term
S_x	= Standard deviation
s	= Sign function for iteration
t	= Time
$t_{\alpha/2}$	= Student's t-distribution
T	= Temperature
v	= Velocity
W	= Total error
x	= Axial coordinate
Y	= Fluctuating dilatation in compressible turbulence
Z	= Elemental mass fraction
z	= Function
δ_{ij}	= Kronecker delta
γ	= Ratio of specific heats
ϵ	= Turbulent dissipation
ϵ_n	= Nozzle expansion ratio
η	= Specific enthalpy
η_f	= Fin efficiency
θ	= Normalized temperature parameter
μ	= Dynamic viscosity
ρ	= Density
σ	= Boundary layer correction factor
τ	= Shear stress
ν	= Kinematic viscosity
ϕ	= Instantaneous species

Subscripts

aw	= Adiabatic wall
b	= Buoyant effect
B	= Fin base
c	= Chamber
co	= Coolant
ct	= Curvature at throat
e	= Nozzle exit
eff	= Effective
f	= Fuel
g	= Gas
H	= Enthalpy
H^*	= Instantaneous enthalpy
i	= Element i
j	= Species j
ke	= Turbulent kinetic energy
M	= Dissipation rate
ns	= Nozzle stagnation
ox	= Oxidizer
r	= Radial coordinate
R	= Removed
t	= Throat
to	= Total
tu	= Turbulent
w	= Wall
x	= Axial coordinate

z = Tangential coordinate

ϵ = Turbulent dissipation

Appendix B: Sample Calculations

Sample calculations employed in the design of the combustors are shown below. Equations 53-55 show values applicable for both prototypes, while equations 56-64 are solved employing the geometry of the 1-MW combustor. Select calculations must be computed using English units due to implicit conversion factors; these are noted by an (E) in the equation name. Table 17 shows the values required for the combustion calculation, while Table 18 displays those required for cooling system parameters.

Combustor Calculations

Table 17: Combustion parameters for 1MW model

Parameter	SI	Units	English	Units
γ	1.12	--	--	--
$(P_c)_{ns}$	758	kPa	110	psi
P_e	117	kPa	17	psi
g	9.81	m/s ²	32.2	ft/s ²
R	396	J/kg-K	73.63	lbf-ft/lbm-R
$(T_c)_{ns}$	3315	K	5967	R
D_t	16	mm	.6284	in
O/F	3.6	--	--	--

- Theoretical expansion ratio

$$\epsilon_n = \frac{A_e}{A_t} = \frac{\left(\frac{2}{\gamma+1}\right)^{\frac{1}{\gamma-1}} \left[\frac{(P_c)_{ns}}{P_e}\right]^{\frac{1}{\gamma}}}{\sqrt{\frac{\gamma+1}{\gamma-1} \left[1 - \left(\frac{P_e}{(P_c)_{ns}}\right)^{\frac{\gamma-1}{\gamma}}\right]}} = \frac{\left(\frac{2}{2.12}\right)^{\frac{1}{1.12-1}} \left[\frac{110}{17}\right]^{\frac{1}{1.12}}}{\sqrt{\frac{2.12}{.12} \left[1 - \left(\frac{17}{110}\right)^{\frac{.12}{1.12}}\right]}} = 1.82 \quad [53]$$

- Nozzle Exit velocity (E)

$$v_e = \sqrt{\frac{2g\gamma}{\gamma-1} R(T_c)_{ns} \left[1 - \left(\frac{p_e}{(p_c)_{ns}}\right)^{\frac{\gamma-1}{\gamma}}\right]}$$

$$= \sqrt{\frac{2*32.2*1.12}{.12} 73.63 * 5967 \left[1 - \left(\frac{17}{110} \right)^{\frac{.12}{1.12}} \right]} \quad [54]$$

$$= 6919 \frac{ft}{s} = 2109 \frac{m}{s}$$

- Nozzle Exit Temperature

$$T_e = (T_c)_{ns} \left[\frac{p_e}{(p_c)_{ns}} \right]^{\frac{\gamma-1}{\gamma}} = 5967 * \left[\frac{17}{110} \right]^{\frac{.12}{1.12}} = 4885 \text{ R} = 2713 \text{ K} \quad [55]$$

- Required mass flow (E)

$$\dot{m} = A_t (p_c)_{ns} \sqrt{\frac{\gamma \left[\frac{2}{\gamma+1} \right]^{\frac{\gamma+1}{\gamma-1}}}{R(T_c)_{ns}}} = \left(\frac{\pi}{4} \cdot .0525^2 \right) 110 \sqrt{\frac{1.12 \left[\frac{2}{1.12} \right]^{\frac{1.12}{.12}}}{73.63 * 5967}} = .0057 \frac{slugs}{s} = 83.2 \frac{g}{s} \quad [56]$$

- Fuel mass flow

$$\dot{m}_{fuel} = \frac{\dot{m}}{(1+O/F)} = \frac{83.2}{(1+3.6)} = 18.1 \text{ g/s} \quad [57]$$

- Oxygen mass flow

$$\dot{m}_{oxygen} = \dot{m}_{fuel} * O/F = 18.1 * 3.6 = 65.16 \text{ g/s} \quad [58]$$

Cooling System Calculations

Table 18: Cooling system parameters for 1-MW model

Parameter	SI	Units	English	Units
$T_{w,g}$	848	K	1526	R
μ_{ns}	.00011	Pa.s	5.85 E-6	lb/in-s
$C_{p_{ns}}$	2.286	kJ/kg-K	.5371	BTU/lb-F
Pr_{ns}	.664	--	--	--
c^*	1786	m	5862	ft/s
R_{ct}	.0119	m	.47	in
k_{co}	.6	W/m-K	.0012	BTU-in/s-F ²
ρ_{co}	998	kg/m ³	62.3	lb/ft ³
v_{co}	9.1	m/s	29.9	ft/s
μ_{co}	.0089	Pa.s	.006	lb/ft-s
$\mu_{co,wall}$.00176	Pa.s	.0012	lb/ft-s
D_h	.002	m	.079	in
$k_{wall,throat}$	16.64	W/m-K	.032	BTU-in/s-F ²
$R_{1(throat)}$.00811	m	.32	in
$R_{2(throat)}$.00911	m	.36	in
T_{co}	300	K	540	R

- Boundary layer correction factor at combustor throat

$$\sigma = \frac{1}{\left[\frac{1}{2} \frac{T_{w,g}}{(T_c)_{ns}} \left(1 + \frac{\gamma-1}{2} \right) + \frac{1}{2} \right]^{.68} \left[1 + \frac{\gamma-1}{2} \right]^{.12}} = \frac{1}{\left[.5 * \frac{848}{3315} (1.06) + \frac{1}{2} \right]^{.68} [1.06]^{.12}} = 1.35 \quad [59]$$

- Gaseous convective heat transfer coefficient at combustor throat (E)

$$\begin{aligned} h_g &= \left[\frac{0.026}{D_t^{0.2}} \left(\frac{\mu_{ns}^{0.2} C_{p_{ns}}}{Pr_{ns}^{0.6}} \right)_{ns} \left(\frac{p_{cns} g}{c^*} \right)^{0.8} \left(\frac{D_t}{R_{ct}} \right)^{0.1} \right] \left(\frac{A_t}{A} \right)^{0.9} \sigma \\ &= \left[\frac{0.026}{.6284^{0.2}} \left(\frac{(5.85E-6)^{0.2} * .53716}{.6644^{0.6}} \right)_{ns} \left(\frac{110 * 32.2}{5862} \right)^{0.8} \left(\frac{.6248}{.47} \right)^{0.1} \right] 1.35 \\ &= .001639 \frac{Btu}{in^2-s-R} = 4821.4 \frac{W}{m^2-K} \end{aligned} \quad [60]$$

- Heat Flux calculation at combustor throat

$$\dot{q} = h_g ((T_c)_{ns} - T_{w,g}) = .6 * 4821.4 * (3315 - 848) = 7.137 \frac{MW}{m^2} \quad [61]$$

- Coolant convective heat transfer coefficient
A coolant velocity of 9.1 m/s and a hydraulic diameter of 2 mm are assumed.

$$\begin{aligned}
h_{co} &= \frac{k_{co}}{D_h} C_1 Re_{co}^{.8} Pr_{co}^{.4} \left(\frac{\mu_{co}}{\mu_{w,co}} \right)^{.14} \\
&= \frac{.6}{.002} \cdot 0.027 \left(\frac{998 \cdot 9.05 \cdot .002}{.001003} \right)^{.8} \left(\frac{4182 \cdot .001003}{.6} \right)^{.33} \left(\frac{.00089}{.000176222} \right)^{.14} \\
&= 52359 \frac{W}{m^2-K}
\end{aligned} \tag{62}$$

- Inner wall temperature at combustor throat

$$\begin{aligned}
T_r &= \left(\frac{-\dot{q} \cdot r_1}{k} \right) \ln(r) + \left(\frac{h_{co} \left(\frac{\dot{q} \cdot r_1}{k} \ln(r_2) + T_{co} \right) + \dot{q}}{h_{co}} \right) \\
&= \left(\frac{-7.14E6 \cdot .00811}{16.64} \right) \ln(.00811) + \left(\frac{52359 \left(\frac{7.14E6 \cdot .00811}{16.64} \ln(.00911) + 300 \right) + 7.14E6}{52359} \right) \\
&= 841 \text{ K}
\end{aligned} \tag{63}$$

- Channel wall temperature at combustor throat

$$\begin{aligned}
&= \left(\frac{-7.14E6 \cdot .00811}{16.64} \right) \ln(.00911) + \left(\frac{52359 \left(\frac{7.14E6 \cdot .00811}{16.64} \ln(.00911) + 300 \right) + 7.14E6}{52359} \right) \\
&= 436.4 \text{ K}
\end{aligned} \tag{64}$$

Appendix C: Experimental Uncertainty Calculations

An error analysis of flow and temperature measuring devices was performed for test times exceeding two minutes. A total of four test runs were evaluated between times of 50 and 100 seconds; the range corresponds to stable flows, unaffected by valve operations. Equation 65 was employed to estimate the total error in each device, with P being the random error and B the systematic error. Systematic errors were provided by the manufacturer to be 1.5% for Flowmeters and .75% for Thermocouples. Equation 66 was employed to calculate random error, assuming a 95% confidence interval. Table 19 shows the individual values for individual parameters. An average error of 3.2% was observed for temperature measurements, with a 6.6% error for flow devices.

$$W = \sqrt{P^2 + B^2} \quad [65]$$

$$P = t_{\alpha/2} * \frac{s_x}{\sqrt{n}} \quad [66]$$

Table 19: Error analysis of temperature and flow sensors

	Average Value (LPM)	Random Error	Bias Error	Overall Error
Fuel Flowmeter	87.2	10.8%	1.5%	10.9%
Oxidizer Flowmeter	154.0	1.5%	1.5%	2.2%
Total Flow	241.2	3.5%	1.5%	3.8%
	Average Value (C)	Random Error	Bias Error	Overall Error
Incoming H₂O Temperature	28.95	3.6%	.75%	3.7%
Outgoing H₂O Temperature	30.98	3.6%	.75%	3.7%
Combustor Surface Temperature	61.90	2.1%	.75%	2.3%

Appendix D: Estimates of Numerical Error for 60 kW Coupled Simulation

A computational error analysis was performed in accordance to the methods described by Schwer [56] and Slater [57] on the examination of spatial grid convergence. This study is based

on the relationship given by traditional error analysis, Eq. 67 and its subsequent logarithmic form, Eq. 68, where slope o is defined as the observed rate of convergence, and E is the discretization error. In this study, the mesh discretization parameter h_m has been normalized in accordance to the number of elements in each grid, where the unit value corresponds to the finest grid.

$$E(h_m) = u_{exact} - u(h_m) \approx C h_m^o \quad [67]$$

$$\log E(h_m) = \log(C) + o \log(h_m) \quad [68]$$

As the exact solution u_{exact} is unknown, Eqn. 67 is rearranged as the following system of equations 69-71, corresponding to a transcendental function for the order of convergence o [57]. These equations are solved in an iterative manner assuming $z(o)=0$ as an initial value. The iterative method is employed due to the choice of a nonuniform grid refinement ratio h_m . The Richardson extrapolation 72 is subsequently applied to estimate a converged solution equal to parameter u_{exact} . In this study, temperature and heat flux parameters have been evaluated for the converging-diverging nozzle, with a focus on the throat location. Figures 74 and 75 show the spatial error % in log-log space for the aforementioned parameters. It is apparent from Figure 74 that at the same location, temperature and heat flux parameters display similar rates of convergence for the coarse-medium and medium-fine meshes. In contrast, Figure 75 shows a marked difference between the nozzle average and localized points. This contrast corresponds to a slope of 3.2 for the throat location and an average nozzle convergence rate of 1.1. This difference is attributed to an increased element refinement at locations near the throat.

$$o = \frac{|\ln|^{u_{32}/u_{21}}| + z(o)|}{\ln r_{21}} \quad [69]$$

$$z(o) = \ln \left(\frac{e_{21}^o - s}{e_{32}^o - s} \right) \quad [70]$$

$$s = \text{sign}(u_{32}/u_{21}) \quad [71]$$

$$u_{10} = \frac{e_{21}^o u_1 - u_2}{e_{21}^o - 1} \quad [72]$$

$$\text{Spatial Error \%} = F_s \left| \frac{u_{\text{specific}} - u_{\text{exact}}}{u_{\text{exact}}} \right| * 100\% \quad [73]$$

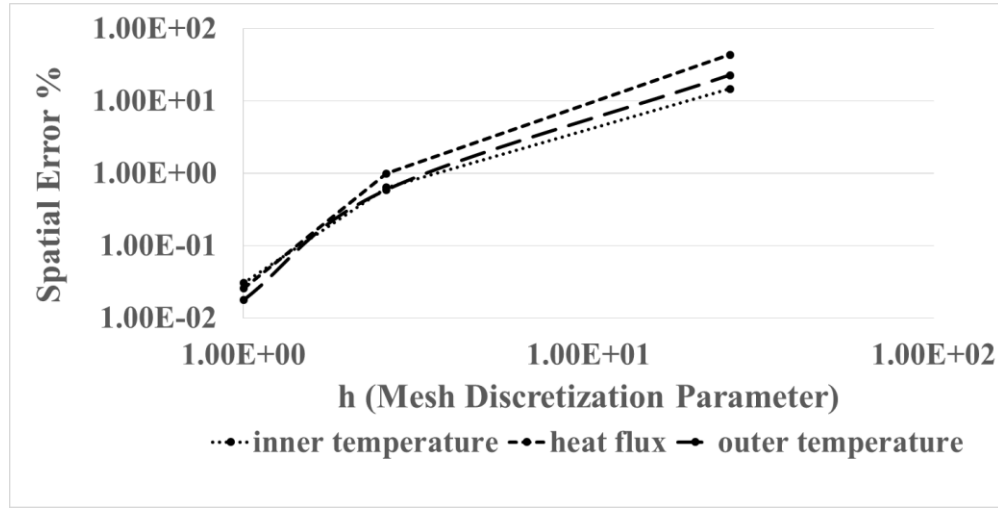


Figure 74: Spatial error % in log-log space comparing temperature and flux values for localized point

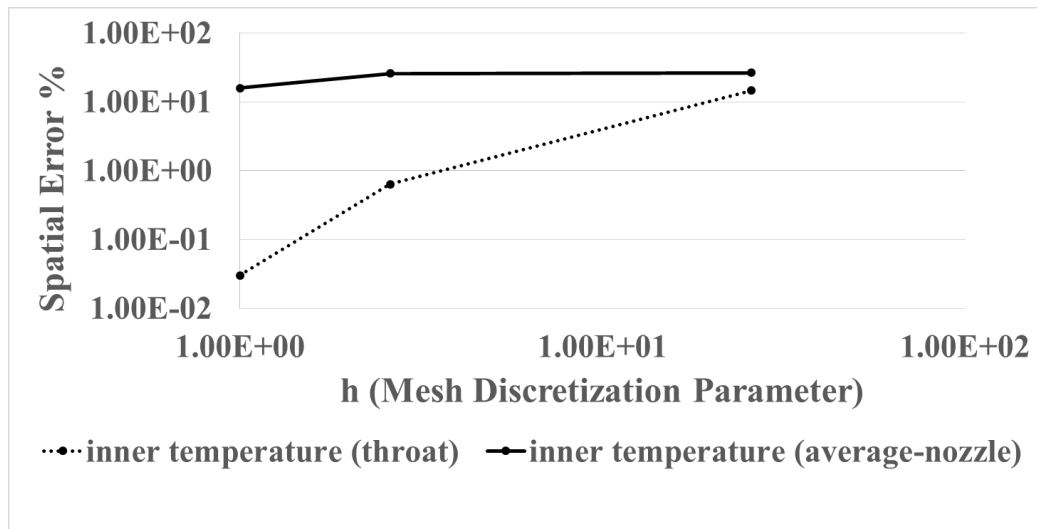


Figure 75: Spatial error % in log-log space comparing average and localized values

The Grid Convergence Index (GCI) has been calculated to estimate discretization error. This parameter is given by Eq. 74. A safety factor F_s of 3 has been applied to compare only the medium and fine meshes, providing a more conservative estimate and ensuring the comparisons are within the asymptotic range of convergence. Table 20 shows the convergence predictions for throat temperature and heat flux parameters. The results from the GCI show that a further refinement of the mesh would result in no more than a .03% change in throat parameters. The overall analysis shows that the fine mesh is sufficiently refined in accordance to the approximations provided by the comparison methods.

$$GCI_{21} = F_s \frac{er_{21}}{e_{21}^o - 1} \quad [74]$$

Table 20: Numerical predictions of converged value

	Fine Mesh	Richardson Extrapolation	GCI	GCI Range (95% confidence)
Inner Temperature (K)	861.35	861.26	0.03%	[861.1, 861.6]
Outer Temperature (K)	475.03	475.05	0.02%	[474.9, 475.1]
Heat Flux (MW/m2)	8.288	8.289	0.03%	[8.286, 8.2904]

Appendix E: Material properties for numerical models

The polynomials employed for the material definition of water and Inconel 718 are presented below. Second- to sixth-order polynomials were employed to represent the properties of the materials in their expected range. Water properties were plotted according to the NIST database to at least 480 K (207 C). Inconel's thermal conductivity was obtained for a range of 300-100 K (27-727 C).

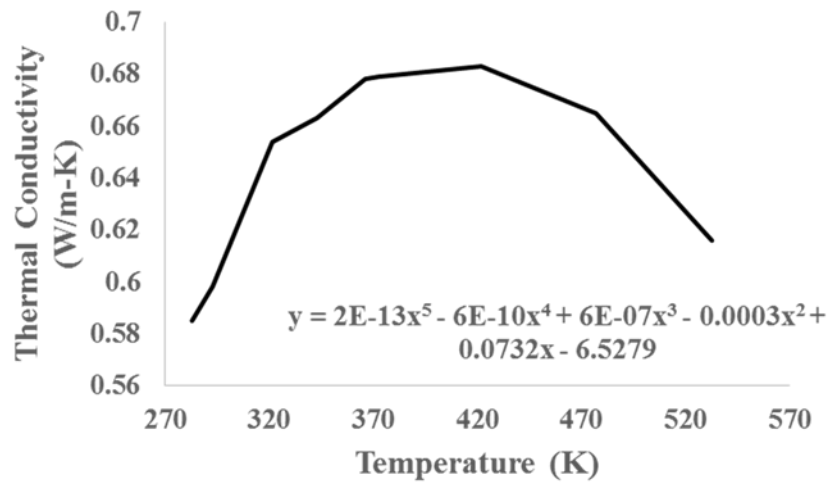


Figure 76: Thermal conductivity of water

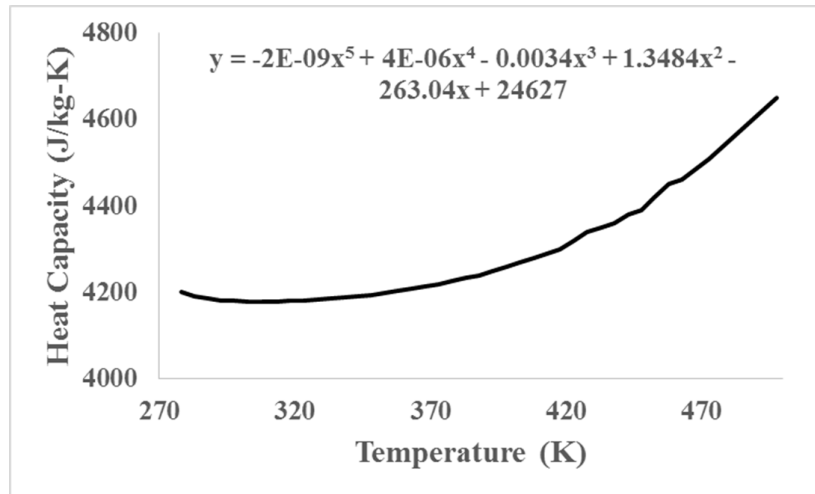


Figure 77: Heat capacity of water

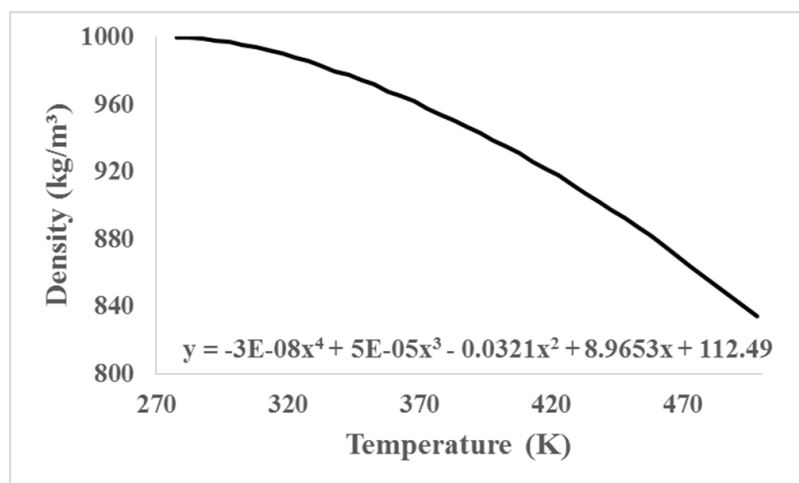


Figure 78: Density of water

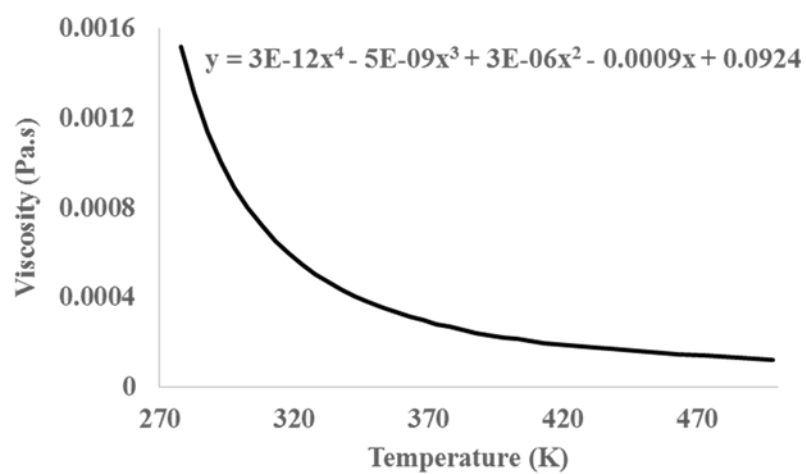


Figure 79: Viscosity of water

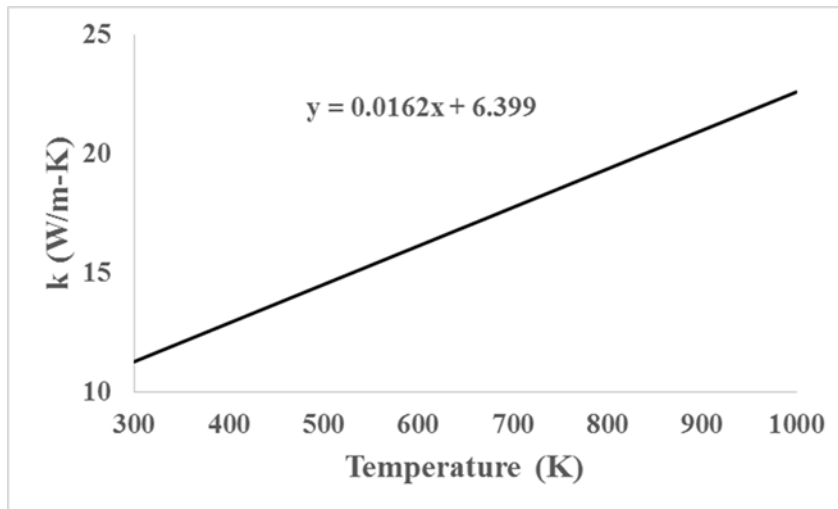


Figure 80: Thermal conductivity of Inconel 718

143

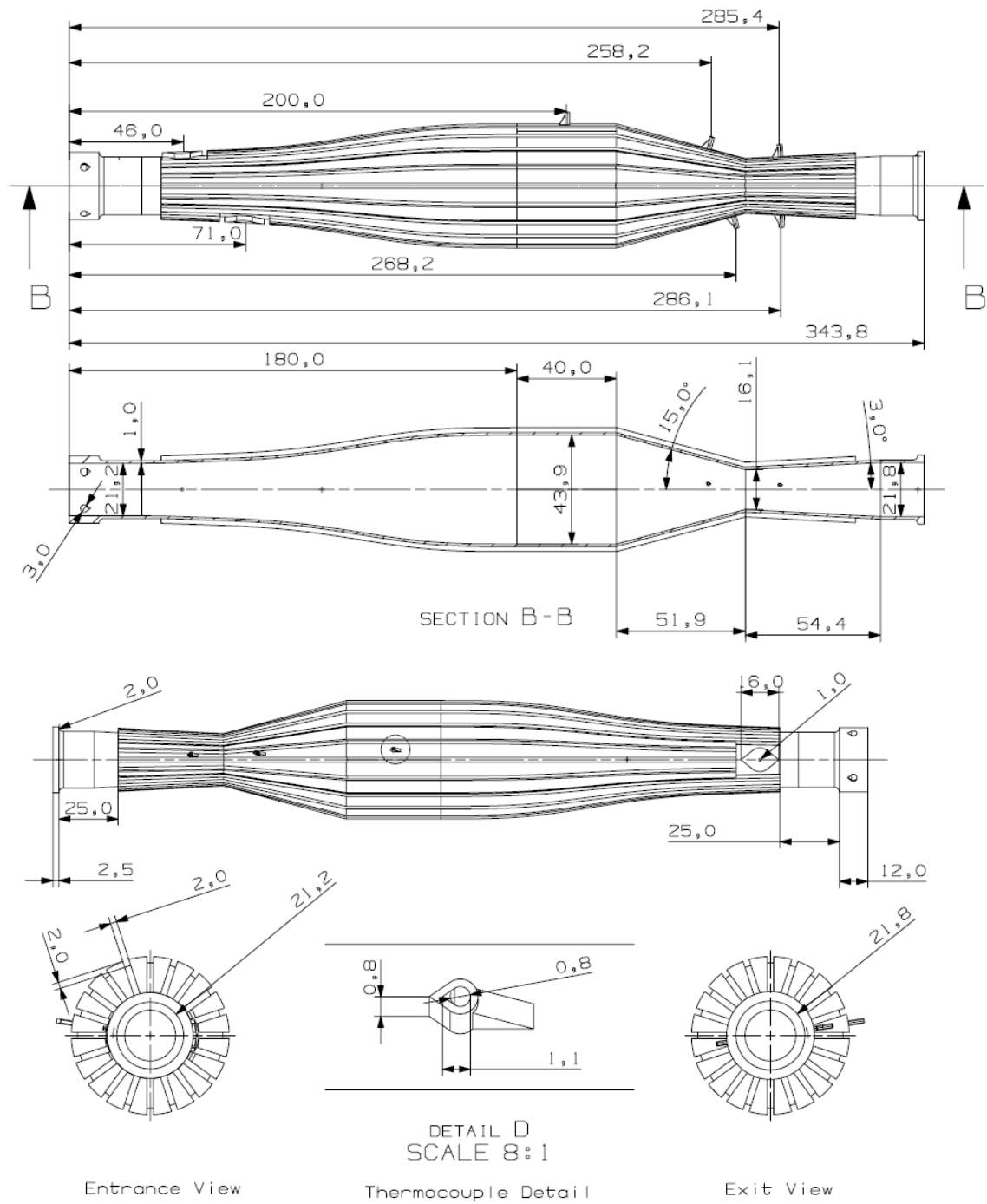


Figure 82: Dimensions for 1-MW Combustor (mm)

Vita

Luisa Alejandra Cabrera Maynez earned her Bachelor of Science in Mechanical Engineering from The University of Texas at El Paso in 2012. She received her master's in 2014, and joined the doctoral program in Mechanical Engineering the same year. Her research interests are in the areas of high heat flux thermal system design and the development of rocket technology in terrestrial applications. Dr. Cabrera Maynez has received a number of honors and awards including the CONACYT doctoral fellowship and a best paper award from the American Institute of Aeronautics and Astronautics. She was also selected to attend the 2016 Princeton summer school on combustion. While pursuing her degree, Dr. Cabrera Maynez worked as a research associate and teaching assistant for the Department of Mechanical Engineering at UTEP. She has presented her research at several international conference meetings, including the 2016 Joint Propulsion Conference and the 2017 Aerospace Sciences Meeting. Dr. Cabrera Maynez's dissertation entitled "Investigation on a Cooling Channel Design for a High Heat Flux Oxy-Fuel Direct Power Extraction Combustor" was supervised by Dr. Norman Love. Dr. Cabrera Maynez has accepted a research and development position with Intel Corporation.

Permanent address: Palma Areca 4750-6

Ciudad Juarez, Chihuahua, Mexico, 32664

This dissertation was typed by Luisa Alejandra Cabrera Maynez